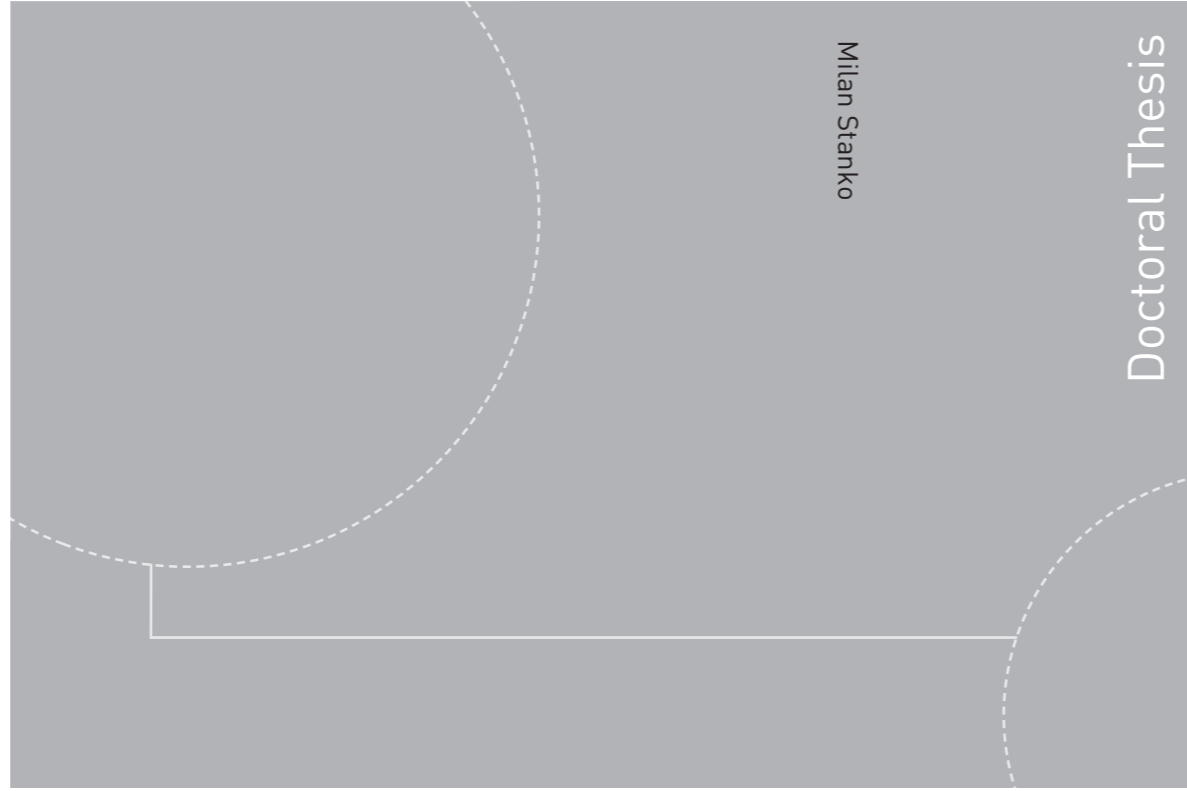


ISBN 978-82-326-0282-7 (printed version)
ISBN 978-82-326-0283-4 (electronic version)
ISSN 1503-8181



Doctoral theses at NTNU, 2014:180

NTNU
Norwegian University of Science and Technology
Faculty of Engineering Science and Technology
Department of Petroleum Engineering
and Applied Geophysics



Doctoral theses at NTNU, 2014:180

Milan Stanko

**Topics in Production Systems
Modeling: Separation, Pumping
and Model Based Optimization**

Milan Stanko

Topics in Production Systems Modeling: Separation, Pumping and Model Based Optimization

Thesis for the degree of Philosophiae Doctor

Trondheim, June 2014

Norwegian University of Science and Technology
Faculty of Engineering Science and Technology
Department of Petroleum Engineering
and Applied Geophysics



NTNU – Trondheim
Norwegian University of
Science and Technology

NTNU

Norwegian University of Science and Technology

Thesis for the degree of Philosophiae Doctor

Faculty of Engineering Science and Technology
Department of Petroleum Engineering
and Applied Geophysics

© Milan Stanko

ISBN 978-82-326-0282-7 (printed version)

ISBN 978-82-326-0283-4 (electronic version)

ISSN 1503-8181

Doctoral theses at NTNU, 2014:180



Printed by Skipnes Kommunikasjon as

Abstract

This thesis addresses three distinct topics within oilfield production technology: 1) Inline oil-water separation for subsea applications, 2) Model based constrained optimization for production networks of high water cut wells boosted by ESPs (Downhole Electric Submersible Pumps), and 3) Hydraulic analysis of a novel configured hexagonal positive displacement pump.

While each of the three topics in the thesis is investigated and discussed in a stand-alone manner, they all share a common industry objective; increasing the yield and prolonging the viable production period of hydrocarbon producing fields. More specifically, they reside within two important classes of production technology challenges; (a) boosting the deliverability and the flow of wells with high water content, and (b) separating and removing of water from hydrocarbon streams as close as possible to the source in a production gathering system. Numerical modeling is the main methodology employed in the three topics, where modeling results are substantiated by field scale or laboratory generated data.

The inline oil-water separation technology addressed in this thesis is based on a controlled and distributed tapping from the lower side of a water rich stream flowing in an inclined pipe spool. The long term objective is to develop a capability for seabed separation near the subsea wells in mature offshore fields with high water production and declining reservoir pressure. The intention is to reduce the backpressure on the wells and increase or maintain their production level. The production gain is achieved by harnessing and hydraulically manipulating the energy of the inlet mixture stream to reduce the backpressure exerted by the outlet streams. Important and unique features of the concept are; the separation and phase splitting do not consume external energy, there are no major moving parts, and there is inherent performance tolerance to deviations from the design set-points.

The thesis expands an earlier IPT/NTNU concept verification research project (Sponsored by the Research Council program DEMO 2000) which involved experimenting with a low pressure full scale separator test facility. This thesis progresses the relevant previous knowledge and information from a concept validation level to establishing and validating a more detailed design strategy and a more focused performance design for the separator. The thesis brings the investigated separation approach to a mature level where the fluid mechanics design aspects are largely clear and understood and are ready as an input for the mechanical design of a separator prototype.

The separation was analyzed from the multiphase hydraulic design point of view using numerical experimentation as the primary tool. The research methodology comprised of conducting the following tasks: (a) developing a procedure to assess the potential production gain of installing the inline separator in a subsea production system and to identify the design requirements for obtaining a specified separator performance, (b) introducing and demonstrating concepts to quantify the drainage performance of a single and multiple tapping points, (c) Validating the usefulness of 3D CFD (Computational Fluid Dynamics) methods to represent the fluid dynamics details of an oil-in-water dispersion and separation, (d) Employing the same 3D CFD model to reproduce the laboratory experimental results.

The other two topics in the thesis constitute a response to emerging field scale problems where the industry have called for an immediate and sound modeling based diagnostic and modeling based investigative design.

The second topic addresses an optimization strategy for large oil production systems consisting of clusters of high water-cut, low GOR oil wells producing by ESP. The production streams of the wells converge through a multi branched surface gathering system into a system of main flow conduits leading to a single processing plant. The objective is to perform a model based numerical optimization to maximize oil production and reduce lift costs by modifying ESP rotor rotation frequency while complying with multiple operational constraints. While industry is currently in possession of tools to perform such tasks the outcome is inconsistent and yields poor optimization result when modeling large system with many wells, complex network and large number of constraints. An investigative task to clarify the source of the difficulties was deemed necessary.

The optimization technique is described in the thesis and employed to quantifying the achievable production gains. It also identifies the computational hurdles encountered in computing the global production optimum. The thesis reports and discusses modeling and optimization using three cases: two are scaled-down synthetic cases to establish the fundamentals of the computational process, and one case on a field-scale production system is used to capture the impact of system complexity. The observed outcome and the conclusions of the investigation provide bases for a robust and consistent production optimization program of a large field. The details of this industrial scale project are beyond the scope of this thesis

The third topic deals with modeling and critical analysis of a novel design of a positive displacement pump for drilling mud circulation. The concept has been commercialized and launched to the offshore market in recent years (commercially called "Hex pump"). The obvious attractiveness of the pump is its compactness and its small footprint when mounted on congested offshore platforms. However, the pumping performance of the pilot installation was very poor exhibiting excessive pulsation, vibration, mechanical failures and noise. These have driven expensive and critical drilling operations offshore to a halt. It has been recognized at this stage that the unique and innovative design features of the pump together with the criticality of it good and safe performance warned a thorough model based concept analysis and verification. The thesis describes the hydraulic performance modeling and its use to identify the concept inherent pulsation generating source. The conducted modeling and its interpretation are of novel nature and the results revealed a fundamental conceptual flaw. The research outcome had a prompt and an immediate impact on the industry decision of deploying this novel pump type.

On the numerical models employed in the thesis

The present thesis employs several numerical models and computational tools for the analysis of the topics under study. Most of the numerical models were built by the author in specialized canned commercial software with academic licenses and no major modification was done to out-of-the-box software functionality. Some models however were created from scratch by programming computational routines and elements in software suited for that purpose.

The main body of the thesis dedicates limited attention to the details of the construction and set up of the models in order to simplify the reading process. However, Appendix A gives an overview of all numerical models employed in the thesis and it provides the most important details about them. Appendix B provides general details about the commercial software employed.

Most of the numerical models are contained in binary files making impossible to include them as a text attachment to the thesis.

A thorough quality control process has been performed to ensure the validity of the results. This was usually done by running simpler cases and checking for physical coherence, checking with analytical expressions and by comparing the results of the numerical models of one software with another.

Acknowledgments

I would like to express my deep gratitude to my supervisor, Professor Michael Golan, for giving me this opportunity, for sharing his knowledge, for his guidance, support, advice and help along these years. Prof. Golan is an incredible person, scientist and teacher and it has been an honor and a privilege to work with him.

I would like to thank my co-supervisor Professor Miguel Asuaje for his contribution to my undergraduate and graduate learning, especially for his efforts to materialize this opportunity. I truly appreciate his mentoring, inspiring energy, persistence and hard work.

I express my gratitude to Professor Curtis Hays Whitson for his good teaching and for the time invested in many fruitful discussions. I appreciate his vast knowledge and skills in many areas.

I would like to thank the members of the committee for taking time out from their busy schedule to review and evaluate my work. Their comments and observations are welcomed.

I thank Rocio Rivera for preparing the ground for a great thesis startup, for her participation in fruitful technical discussions, sharing material and answering my frequent requests for additional information.

I acknowledge the support from NOTUR (The Norwegian Metacenter for Computational Science) and the NTNU HPC group (High performance computing) for the computational resources allocated to this project.

I would like to thank the NTNU Faculty of Engineering Science and Technology (IVT) for providing the financial support (my scholarship) for this research.

I acknowledge the financial support of Statoil for traveling to the International Conference on Multiphase Flow 2013 in Korea.

I acknowledge the contribution of Stein Ørjan Solrud and Ola-Marius Røyset to the development of the Pipe-it template for ESP optimization.

I would like to thank Gilberto Nuñez for helping me with format issues in Word while preparing the final thesis manuscript.

I would also like to thank the staff of the Department of Petroleum and Applied Geophysics for all the support provided and for creating an enjoyable working atmosphere.

I would like to thank my family and friends for their unconditional support.

I would like to thank my wife, Andrea Shmueli for her support, patience, love and smiles that brighten my day.

Papers

List of papers:

- **Paper 1 (Conference paper, published):** Stanko, M.; Golan, M.; Asuaje, M. (2013) 3D-CFD numerical simulation of gravity induced segregation in water dominated dispersed oil-water pipe flow. 8th International Conference on Multiphase Flow 2013. 2013 may 26th to 2013 may 31st
- **Paper 2 (Journal paper, published):** Stanko, M.; Golan, M. (2013). Hexagonal reciprocating pump: advantages and weaknesses. International Journal of Fluid Machinery and Systems (ISSN 1882-9554). 2013 ;Volum 6.(3) s. 121-136. DOI: 10.5293/IJFMS.2013.6.3.113.
- **Paper 3 (ready for submission in the SPE journal of Projects, Facilities & Construction):** Stanko, M.; Golan, M. Investigating challenges in conducting model-based constrained optimization of oil well clusters produced by ESP in high water cut producing wells.

“There are two kinds of research: applied research and not yet applied research”

Martin John Rees – Baron Rees of Ludlow

Astronomer Royal, past Master of Trinity College/Cambridge and past President of the Royal Society

“Essentially, all models are wrong, some are useful”

George Box

Contents

Abstract	III
On the numerical models employed in the thesis	V
Acknowledgments.....	VII
1 Chapter 1.....	25
1.1 Introduction.....	25
1.2 Industrial application example of the inline separator	26
1.2.1 Pressure reduction estimation with the deployment of the inline separator	28
1.3 Inline separation definitions, design principles and strategies.....	33
1.3.1 Concept of single tapping point separation performance	34
1.3.1.1 Estimation of the Drainage potential using single pipe/no tapping values	35
1.3.1.2 Visualizing the drainage potential in a phase superficial velocity map - Separation Triangle with unit slope.....	39
1.3.2 Performance of a multiple tapping point arrangement.....	40
1.4 Separation analysis using experimental data.....	41
1.4.1 Effect of pipe inclination in drainage potential – estimation from literature data.....	41
1.4.2 Separation assessment based on experimental data of the separation prototype of Rivera (2011)	42
1.4.2.1 Influence of inclination on oil content of tapped flow.....	44
1.4.2.2 Effect of the number of tapping points on the amount of oil drained.	45
1.5 Evaluating the capability of a CFD model to represent the segregation and separation phenomena in oil in water dispersions	46
1.5.1 Selected experimental data from the literature	46
1.5.2 Background information about the CFD model employed	47
1.5.2.1 Treatment of the dispersed phase in the CFD simulator	48
1.5.2.2 General settings of the CFD model.....	49
1.5.3 Comparison between the experimental data and CFD model results	50
1.5.4 Concluding Remarks	52
1.6 CFD simulations to evaluate the inline separator performance	53
1.6.1 Settings of the CFD simulations.....	53
1.6.2 Simulations performed with the CFD model.....	54
1.6.3 General procedure for acceptance of results of the CFD model.....	54
1.6.4 Results of the CFD model	55

1.6.4.1	Comparison between CFD model and measured data.....	55
1.6.4.2	Case 250 lpm water 27 lpm oil: Effect of Inclination in the drainage potential curve... ..	56
1.6.4.3	Development length	57
	Conclusions and Recommendations	59
	References	60
Appendix A1	1D Integration method for obtaining the water and oil rates of a cross section layer	63
Appendix B1	Deduction of the inclination angle of the line representing all possible conditions downstream a tapping point	65
Appendix C1	Droplet size prediction of an oil in water dispersion.....	67
Appendix D1	Details of the CFD model of the separator prototype (mesh analysis)	71
Appendix E1	Paper.....	73
2	Chapter 2.....	85
2.1	Introduction	85
2.2	Basics of the model-based optimization	86
2.3	Modeling cases and considerations	87
2.4	Case 1. Two oil wells with common wellhead manifold discharging to a pipeline	87
2.5	Case 2: Two clusters of three wells each discharging to a common pipeline	90
2.6	Case 3: Real field production network model.	93
	Conclusions and Recommendations	95
	References	96
Appendix A2	General information about the considered production systems.....	97
Appendix B2	Notes about solving using MS Excel the production hydraulic network of case 1.....	99
3	Chapter 3.....	101
3.1	Introduction	101
3.2	Hexagonal pump characteristics	102
3.2.1	Hexagonal pump piston kinematics and comparison with a crankshaft driven piston ...	104
3.2.2	Operational valve delays in the Hexagonal pump	105
3.2.3	Simulation of the hexagonal pump valve dynamics	108
3.2.3.1	Estimating the valve closing delay from the results of the valve dynamics simulation	109
3.2.3.2	One dimensional simulation of the valve dynamics.....	110
3.2.3.3	Suggestion for improvement of the 1D model.....	114
3.2.3.4	Two dimensional axisymmetric CFD model simulation of the discharge valve dynamics	115
3.3	Transient hydraulic 1D simulation.....	116
3.3.1	Setting up the simulation cases.....	116
3.3.2	Setup of the simulations.....	118
3.3.2.1	The simulator.....	118

3.3.2.2	The boundary conditions.....	118
3.3.3	Results	119
3.3.3.1	Pressure and flow inside the hexagonal manifold	122
3.3.4	Pulsation remediation measures.....	124
3.3.4.1	Case 1: Hexagonal pump with orifice plate.....	124
3.3.4.2	Case 2. Hexagonal pump with orifice plate and gas accumulator.	126
Conclusions and Recommendations		127
References.....		128
Appendix A3	Public drilling records of a platform with the Hexagonal pump installed.....	129
Appendix B3	Hexagonal pump piston kinematics and valve delays.....	131
Appendix C3	Hexagonal pump check valves dimensions.....	135
Appendix D3	Axisymmetric 2D CFD fluid structure numerical simulation of the discharge valve dynamics.....	137
Appendix E3	Transient Fluid Dynamics Numerical Simulator.....	139
Appendix F3	Gas Pulsation Accumulator.....	141
Appendix G3	Simplified resonance assessment of the discharge hydraulic system.....	145
Appendix A	Details about the numerical models and computational tools employed in the thesis.....	147
Appendix B	Brief description of some of the computational tools employed in the thesis.....	153

List of Figures

Fig. 1.1 Functioning principle of the inline multiphase separation strategy.....	25
Fig. 1.2 Prototype testing (a) vs. design analysis (b) concepts of the inline separator	26
Fig. 1.3 Application case for the inline oil-water separator	27
Fig. 1.4 Application case with the inline separator installed.....	27
Fig. 1.5 Pressure reduction on the Production pipeline achieved by installing the inline separator	28
Fig. 1.6 Simplified production system downstream the inline separator and relevant data.....	29
Fig. 1.7 Pressure reduction color map vs Water cut and rate of the separated stream.....	30
Fig. 1.8 Color map of pressure difference between main line and separated line vs water cut and flow rate	31
Fig. 1.9 Inline separator operating with a control valve to control the flow rate separated.....	31
Fig. 1.10 Pressure reduction color map vs Water cut and rate of the separated stream (for viscous oil case)	32
Fig. 1.11 Pressure reduction color map vs Water cut and rate of the separated stream (for gas case) ...	33
Fig. 1.12 Simplified setup to quantify the separation performance of a single tapping point	34
Fig. 1.13 Cross section of a pipe displaying the area to drain	35
Fig. 1.14 Drainage potential quantification procedure	36
Fig. 1.15 water volume fraction and velocity distribution along the diameter for high inclination (a) and low inclination (b).....	36
Fig. 1.16 Sample drainage potential curve	37
Fig. 1.17 two different ways to use the drainage potential curves for tapping planning and design	37
Fig. 1.18 Beginning and end of the drainage potential curve: tapped water flow rate vs tapped stream water cut	38
Fig. 1.19 Different proposals for drainage area in the cross section to compute the drainage potential. 38	
Fig. 1.20 Representation of all possible separation efficiencies in a superficial velocity plot (fixed separated rate).....	39
Fig. 1.21 Drainage potential presented in a phase superficial velocity map	39
Fig. 1.22 Inlet and all possible outlet conditions of the inline separator plotted in a phase superficial velocity plot.....	40
Fig. 1.23 Different drainage strategies proposed for the inline separator	41
Fig. 1.24 Fictitious example of calculating the separator output with a uniform tapping strategy and the drainage potential	41
Fig. 1.25 Percentage of total inlet water flow drained vs water cut of drained stream	42
Fig. 1.26 Experimental setup for Rivera (2011).....	42
Fig. 1.27 Calculating the oil and water flow rates approaching a tapping point	43
Fig. 1.28 Different inclinations to drain a liquid flow rate q_t	44
Fig. 1.29 Different number of tapping points chosen to drain a total amount of flow q_t	45
Fig. 1.30 A 3 droplet class dispersion of oil in water	48
Fig. 1.31 Geometry and boundary conditions location.....	49
Fig. 1.32 Cross section of the mesh.....	50
Fig. 1.33 Simulated water volume fraction profile variation with droplet diameter for case 1	51
Fig. 1.34 Simulated water volume fraction profile for a tuned two diameters class dispersion for Case 2	52
Fig. 1.35 Simulated axial mixture velocity profile for case 2.....	52
Fig. 1.36 Boundary conditions employed in the CFD model	53

Fig. 1.37 Domain dimensions	54
Fig. 1.38 drainage potential curve for 250 lpm water and 27 lpm oil for different inclinations	56
Fig. 1.39 Layer height vs water flow transported in layer	57
Fig. 1.40 Different axial positions measured from the inlet in the CFD model	57
Fig. 2.1 Scheme of a surface network in a hydrocarbon production system with 4-wells cluster	85
Fig. 2.2 Production optimization routine for a hydrocarbon production system with surface network ...	86
Fig. 2.3 Layout of case 1: two wells with common wellhead manifold discharging to a pipeline	88
Fig. 2.4 Total oil production color map for the complete ESP frequency range of wells 1 and 2	89
Fig. 2.5 Layout of case 2: 2 clusters of 3 wells each discharging to a common pipeline	90
Fig. 2.6 Optimum frequencies found with different optimization engines	92
Fig. 2.7 Oil production vs. Iteration number from iteration N°1 to 700 for Pipe-It® optimizers: IPOPT, Reflection and NOMAD	92
Fig. 2.8 Layout of case 2: 2 clusters of 3 wells each discharging to a common pipeline	93
Fig. 2.9 Oil production vs. water production, feasible solutions	94
Fig. 2.10 ESP frequency and Watercut vs well name for base case and optimum	94
Fig. 3.1 Schematic configuration of piston assemblies and power end in the hexagonal pump	102
Fig. 3.2 Discharge flow of the piston used in the hexagonal manifold pump	102
Fig. 3.3 Pump with hexagonal discharge manifold	103
Fig. 3.4 Discharge manifold in reciprocating pumps	103
Fig. 3.5 Theoretical discharge and suction flow rate of the piston defined by the piston movement	104
Fig. 3.6 Piston kinematics of the Hexagonal piston and crankshaft driven piston	105
Fig. 3.7 Primary delays in the suction and discharge cycles of the Hex pump piston	106
Fig. 3.8 Primary delays in the suction and discharge cycles of the Hex pump piston	107
Fig. 3.9 Valve opening delay dependance with valve closing delay	108
Fig. 3.10 Valve configuration in the Hexagonal pump	108
Fig. 3.11 Valve types used in the Hexagonal pump	109
Fig. 3.12 Representative pressure forces acting on the valve body	110
Fig. 3.13 Discharge valve displacement and flow rate from piston chamber.	111
Fig. 3.14 Simulated discharge valve displacement and valve pressure drop	112
Fig. 3.15 Simulated suction valve displacement and inflow to piston chamber versus time	112
Fig. 3.16 Simulated suction valve pressure drop and displacement vs time.	113
Fig. 3.17 Valve closing delay vs pump shaft rotation speed - 1D simulation results	113
Fig. 3.18 Total discharge and suction delays vs pump shaft rotation speed	114
Fig. 3.19 Fluid force function vs valve flow rate for different valve openings	114
Fig. 3.20 Pressure drop across the valve vs flow rate for different valve openings	115
Fig. 3.21 Simulated discharge valve displacement versus time	115
Fig. 3.22 Discharge valve simulation results between CFD model and a 1D approximation	116
Fig. 3.23 Cases simulated using transient hydraulics	117
Fig. 3.24 Ideal and real piston discharge for: (a) Ramp profile, (b) Sinusoidal profile	117
Fig. 3.25 Time dependent flow boundary conditions for cases a, b and c.	119
Fig. 3.26 Calculated discharge pressure and flow for one pump period (T = 0.48 s) for cases a, b and c.	120
Fig. 3.27 Dominant frequencies in the discharge pressure signal for cases a, b and c.	121
Fig. 3.28 Diagram indicating the location of alternating flow in the hexagonal manifold	122
Fig. 3.29 Reciprocating flow in section P5-P4 of the hexagonal manifold.	122
Fig. 3.30 Maximum and minimum pressure values recorded during the simulation along a branch of the hexagonal discharge manifold	123
Fig. 3.31 Maximum and minimum pressure values recorded during the simulation along the discharge piping	123
Fig. 3.32 Dominant frequencies in the pressure signal of the hexagonal manifold point P6.	124
Fig. 3.33 Hexagonal pump configuration with orifice plate.	124
Fig. 3.34 Discharge pressure and flow for the hexagonal pump with orifice	125

Fig. 3.35 Maximum and minimum pressure values recorded during the simulation along a branch of the hexagonal discharge manifold with and without orifice..... 125

Fig. 3.36 Reciprocating flow in section P5-P4 of the hexagonal manifold with orifice plate installed. ... 126

Fig. 3.37 Hexagonal pump configuration with orifice plate and gas accumulator..... 126

Fig. 3.38 Discharge pressure and flow for the hexagonal pump with orifice and gas accumulator. 126

List of Tables

Table 1.1 Viscous oil viscosity dependence with temperature	32
Table 1.2 Richardson exponents for emulsion viscosity	32
Table 1.3 Flow regimes in upwards inclined oil-water flows	43
Table 1.4 Oil volume fraction in tapped stream depending on the inclination for multiple inlet conditions	44
Table 1.5 Selected experimental points with the same upstream conditions, total flow drained but different number of tapping points	45
Table 1.6 Experimental cases simulated in the present study	47
Table 1.7 Physical properties of the experimental fluids for each case.....	47
Table 1.8 Experimental information available for each case	47
Table 1.9 Maximum droplet diameter and Sauter mean diameter predicted by the ULLN model.....	48
Table 1.10 Approach and values used as input for the cases modeled with a CFD model.....	49
Table 1.11 Description of the boundary conditions.....	50
Table 1.12 differences between simulated and experimental values for all cases	51
Table 1.13 boundary conditions employed in the CFD model	53
Table 1.14 Simulations performed with the CFD model of the separator prototype.....	54
Table 1.15 CFD model results compared with experimental results	55
Table 1.16 CFD water volume fraction contours compared with experimental photos	55
Table 1.17 Separation results comparison between CFD model and experimental data.....	56
Table 1.18 Entry development length estimated from the CFD model	57
Table 1.19 Development length for flow between tapping 1 and 2.	58
Table 2.1 Production system modeling and optimization tools employed for each case	87
Table 2.2 Parameters of the optimization engines employed in case 2	91
Table 2.3 Optimum frequencies found with different optimization engines	91
Table 2.4 Comparison of the performance indicators of the current operation and the minimum	94
Table 3.1 Fluid properties and pipe properties and characteristics.....	117
Table 3.2 Piping geometrical characteristics.....	117
Table 3.3 General data for the calculation of the sinusoidal and Ramp piston discharge.....	118

Nomenclature

Chapter 1

HP	High pressure
LP	Low pressure
FPSO	Floating Production, Storage and Offloading
SEP	Separator
μ_m	Oil water mixture viscosity, [cP, Pa s]
μ_o	Oil viscosity, [cP, Pa s]
μ_w	Water viscosity, [cP, Pa s]
GOR	Gas oil ratio
U	Overall heat transfer coefficient, [W/m ² K]
ID	Internal pipe diameter, [m], [mm]
T	Temperature, [°C]
p	Pressure, [bara]
WC	Water cut, [%], [-]
q	Flow rate [Sm ³ /d], [STBD], [scfd]
amb	ambient
d	Droplet diameter, [m, mm]
q _o	flow rate of oil, [m ³ /d, lpm]
q _w	flow rate of water, [m ³ /d, lpm]
ss	Separated stream
mpl	Main production line
A	Cross section area, [m ²]
V _{so}	Oil superficial velocity, [m/s]
V _{sw}	Water superficial velocity, [m/s]
H _w	Water holdup [%, -]
ULLN	Upper-limit log-normal
f_{tp}	Two phase friction factor
We	Weber number
ρ_m	Density of the oil-water mixture, [kg/m ³]
MUSIG	Multiple Size Group
CFD	Computational Fluid Dynamics

Chapter 2

ESP	Electric Submersible Pump
q	Compound liquid flow rate of oil and water, [bbl/d]
q _o	flow rate of oil, [bbl/d]
q _w	flow rate of water, [bbl/d]
f	ESP frequency, [Hz]
q _{maxesp}	maximum allowable ESP flow rate, [bbl/d]
q _{minesp}	minimum allowable ESP flow rate, [bbl/d]
p _{ps}	ESP suction pressure, [psia]
p _R	Reservoir pressure, [psia]
p _{sep}	separator pressure, [psia]
p _{wf}	Bottomhole pressure, [psia]

N	Number of stages in ESP pump
p_{wh}	wellhead pressure, [psia]
ρ	Density, [kg/m^3]
ρ_{mix}	Density of the oil-water mixture, [kg/m^3]
μ	Viscosity [cp]
d	Pipe internal diameter, [in]
WF	Water Fraction, [-]
J	Linear Productivity index for total fluid flow, [STBD/psi]
L	Pipe length, [ft]
g	Gravitational acceleration, [m/s^2]
F_D	Darcy friction factor, [-]
NPSH	Net positive suction head, [m], [ft]

Chapter 3

a	fluid wavespeed, [m/s]
ρ	Fluid density, [kg/m^3]
p	Pressure, [bara]
V	Fluid velocity, [m/s]
g	Gravitational acceleration, [m/s^2]
t	Time, [s]
α	Pipe inclination angle from the horizontal, [rad]
D	Pipe inner diameter, [m]
x	Position coordinate, [m]

Chapter 1

Inline Oil-Water Separation for Subsea Applications

A section of this chapter was gathered into a paper (Appendix E1) and was presented and published at the International Conference of Multiphase Flow in Jeju, South Korea (2013).

1.1 Introduction

The separation strategy consists on draining the multiphase streams while flowing upwards through an inclined tube with distributed off-take points (Fig. 1.1). The separated stream is the heaviest phase that accumulates at the lower part of the pipe. The particular application of this technology is for performing primary water-hydrocarbon separation in hydrocarbon production from mature oil wells (high associated water production). The simplicity of the separator makes it an attractive solution for downhole or subsea water separation which yields a reduced back pressure on the production oil streams and improves the production rates.

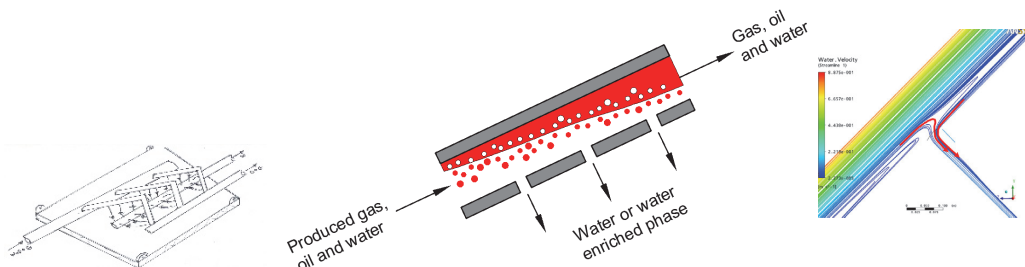


Fig. 1.1 Functioning principle of the inline multiphase separation strategy

The separation technique has a high industrial relevance and applicability, especially for water management issues in mature offshore fields. The handling, treatment and disposal of the water streams require energy, financial resources, time, space, and, in most cases, are critical for the economical profitability of the field (Ferro & Smith 2007). The separation technique is a solution that doesn't require external energy sources to operate, does not have any moving parts and has a negligible pressure drop.

The basic concept of phase separation has been validated through an experimental and modeling research project conducted by NTNU (DGRASS, 2005-2008) as part of the DEMO 2000 program from the Norwegian Research Council. Public domain publications (Rivera 2005, 2008, 2011) of the project results confirmed its industrial potential for downhole (inside wellbore) water-hydrocarbon separation in oil production operations. Furthermore, it also suggested that the greatest industrial potential of this separation concept resides in subsea separation where its configuration is unconstrained by the wellbore size and geometry. Advancing the development of the separation concept from the constraints of the wellbore to the unconstrained seabed domain is the main objective of this research. This project represents one step further in closing the gap between concept and commerciality of the inline separator.

The separation technology was analyzed from the multiphase hydraulic design point of view. The ultimate goal is to establish separator hydraulic design guidelines, methodologies and recommended configurations for a proper operation.

This framework is fundamentally different from the working strategy of previous works carried out within the DEMO 2000 project. As shown in Fig. 1.2 (a) the prototype testing was based in quantifying the

characteristics of the separated stream for a given inlet conditions and separator configuration. The design analysis (Fig. 1.2 b) carried out in the present study looks for determining the characteristics of the inline separator for preset inlet conditions that yield the most beneficial characteristics of the separated stream.

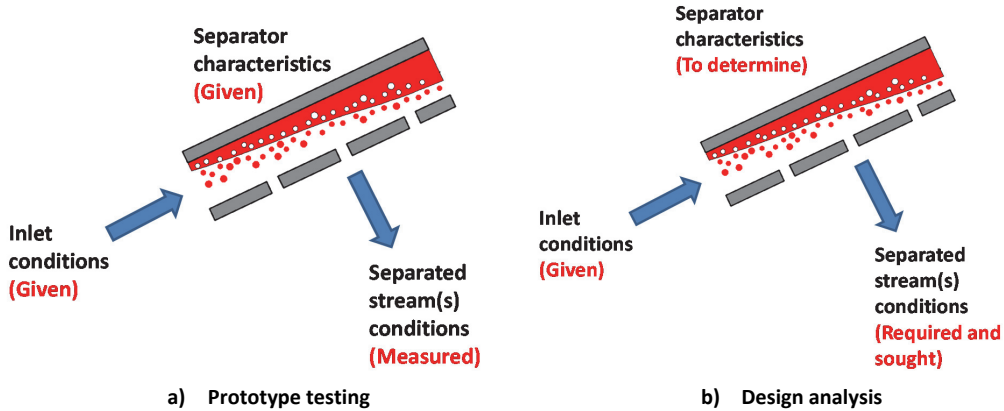


Fig. 1.2 Prototype testing (a) vs. design analysis (b) concepts of the inline separator

Chapter structure: The study departs from a macro level by screening the multiphase hydraulic performance of a simplified production system with the inline separator installed on it. This evaluation is performed with a commercial 1D canned multiphase simulator commonly employed for analyzing hydrocarbon production systems (Pipesim). The analysis identifies the required performance characteristics of the inline separator that yield best effectiveness.

Next definitions and principles useful to quantify the separation performance of the inline separator were introduced, followed by a review and examination of selected experimental data. The data assessment allowed to emit general observations about the phase segregation process in pipes and to detect configurations beneficial for the separation performance.

A 3D CFD (Computational Fluid Dynamics) numerical model is employed to perform numerical experimentation. The model was generated using a canned commercial simulator (Ansys CFX). Several modeling multiphase flow approaches within the simulator were studied by comparing the numerical results with selected experimental data and important observations were generated. This section has been published and presented in an international conference (Appendix E1).

Finally simulations were made of the separator prototype geometry of Rivera (2011) using the 3D CFD model of selected experimental cases.

1.2 Industrial application example of the inline separator

A subsea application example of the technology is presented in Fig. 1.3. Consider a field with mature oil wells with high water production grouped in two clusters and producing through a common pipeline and riser to the production facilities on the vessel (FPSO). The process on the FPSO consists of a separator chain from high pressure (HP) to low pressure (LP). The separated water goes to low pressure deoiling facilities.

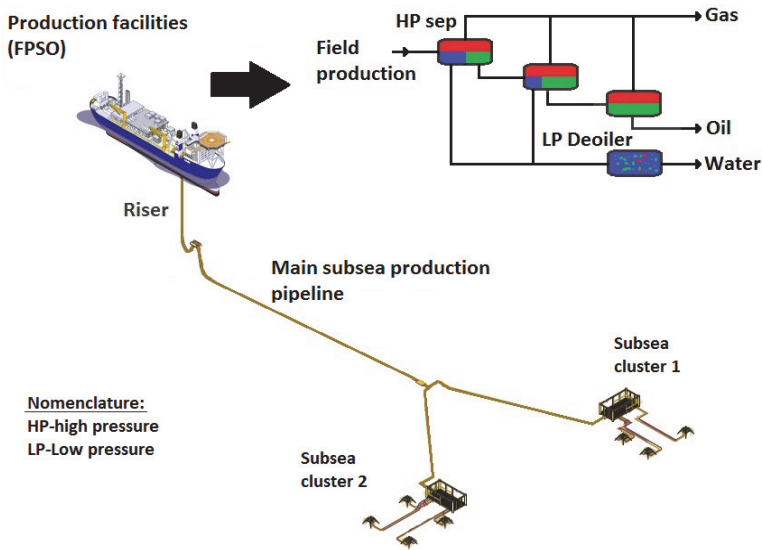


Fig. 1.3 Application case for the inline oil-water separator

A location suggested for installing the inline separator is at the beginning of the subsea production pipeline (after the commingling point of production of the two subsea clusters). In that manner there is only one separator for a group of wells (thus reducing the installation costs) and the backpressure reduction should be still effective because it is very close to the wells.

Fig. 1.4 shows the production system with the separator installed. Another pipeline has been laid parallel to the production pipeline that carries the separated stream (water rich stream tapped from the bottom of the separator). This stream is sent straight to the low pressure deoiling facilities.

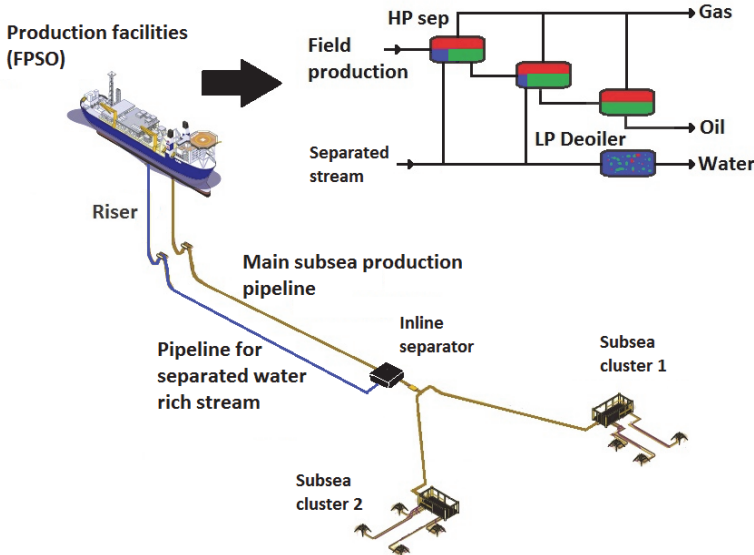


Fig. 1.4 Application case with the inline separator installed

Please note that sometimes an intermediate separator on the FPSO might be required to lower the oil content of this separated stream. This is due to the fact that the maximum allowed oil in water

concentration for the intake of the deoiling facilities is typically between 10000 ppm and 5000 ppm. This corresponds to a very high water cut (99.4 % for typical oil properties) a value that cannot always be guaranteed by the inline separator (according to the results of Rivera 2011).

The production subsea pipeline has now less water content thus reducing the pressure drop in the pipe (Fig. 1.5). The pressure reduction in the subsea production pipeline is originated mainly by two sources: a reduction of the flow rate (as a big percentage of the water has been removed) and a reduction in density of the flow stream.

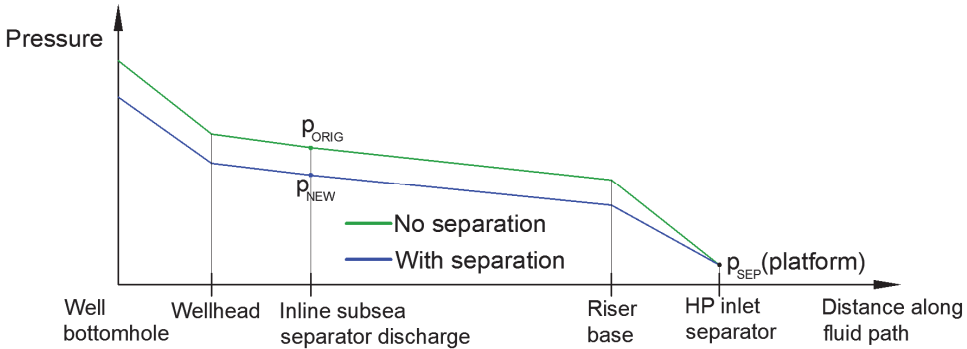


Fig. 1.5 Pressure reduction on the Production pipeline achieved by installing the inline separator

This pressure reduction can be translated to other points upstream the production system: Inlet to the inline separator, cluster, wellhead and well bottomhole. If the pressure at the bottomhole of the well is reduced consequently the well production is increased thus fulfilling the goal of the inline separator. Alternatively, if the reservoir pressure diminishes due to depletion, lowering the bottomhole pressure allows to maintain the same flow rate.

It is not always easy to determine the relationship between pressure reduction and production increase as it depends on the characteristics of the wells (Inflow Performance Relationships, well layout) and the characteristics of the upstream production system (pipeline distances, number of clusters, etc). However, usually a significant pressure reduction is strongly correlated with an increase in production. The following section presents a quantitative estimation of the pressure reduction on a simplified production system downstream the inline separator.

1.2.1 Pressure reduction estimation with the deployment of the inline separator

In this section a general methodology to estimate quantitatively the pressure reduction achieved with the deployment of the inline separator and to determine the required performance of the inline separator is demonstrated. The production system employed in the analysis represents a typical subsea field in the North Sea.

This simulation was performed using a canned simulation program for hydrocarbon production systems (Pipesim). The modeled system has two independent branches as shown in Fig. 1.6: One branch formed by the production subsea pipeline, the production riser and the high pressure separator, and a second branch formed by the separated stream pipeline, the separated stream riser and the deoiler facilities. Some relevant data employed in the simulation is also presented in the figure. As a starting point the viscosity of the oil-water mixture was modeled by fixing arbitrarily a cut off value (60% WC) and assigning the viscosity of the oil for lower water cuts and the viscosity of the water for higher water cuts. The oil viscosity behavior with temperature was assumed to be similar to kerosene (Roymech, 2013) and a 4 points table was introduced in the simulator.

The model selected for estimating the pressure drop in pipes is the default: "bj" correlation (based on the work by Baker, Nielson & Gabb 1988) with no slip assumption and using the Moody friction factor.

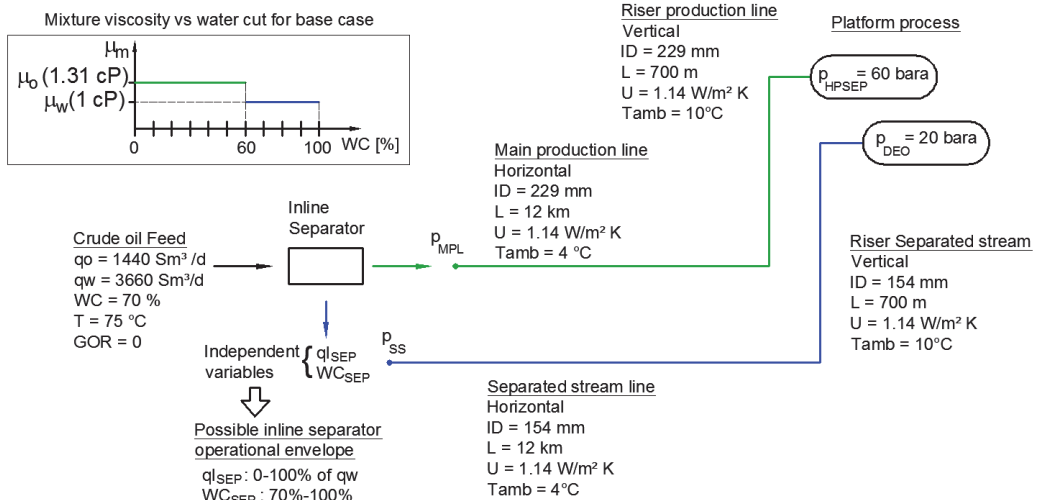


Fig. 1.6 Simplified production system downstream the inline separator and relevant data

The system was modeled in the following manner: the two end nodes (i.e. High pressure separator and deoiler) are considered as pressure nodes and the two start nodes (i.e. discharges coming from the inline separator) are considered flow rate nodes. The results of the simulation yield the pressure at the inlet of the main production pipeline (p_{MPL}) and the pressure at the inlet of the separated stream pipeline (p_{SS}).

A first simulation with no inline separator was made to record the production line inlet pressure with no separator installed ($p_{\text{MPL}}^{\text{NOSEP}}$). Afterwards several simulations were made for 130 combinations of different values of separated stream liquid flow rate (q_{SEP}) and water cut of separated stream (WC_{SEP}). The separated liquid flow rate ranged from 10% to 100% of the water rate at the inline separator inlet and the water cut of the separated stream ranged from the water cut value at the inlet of the inline separator to 100%. The combinations were designed to cover all possible separation efficiencies (in this context separator efficiency refers to the amount of oil in the separated stream) and operational conditions of the inline separator.

The resulting flow rate and water cut of the main production pipeline were calculated using these values and the fixed inlet to the inline separator.

The calculation for each one of the cases were made in MS Excel calculation sheet and the Pipesim simulations were modified, run and results read using a VBA excel routine (through the Openlink functionality).

The pressure reduction (in %) of each case was calculated according to Eq. 1.1.

$$\Delta p = \left(\frac{p_{\text{MPL}}^{\text{NOSEP}} - p_{\text{MPL}}}{p_{\text{MPL}}^{\text{NOSEP}}} \right) \cdot 100 \quad \text{Eq. 1.1}$$

The following cases were analyzed:

1. **Base case:** low viscosity oil (kerosene-like) with no emulsion behavior
2. Low viscosity oil (kerosene-like) with emulsion behavior (from Brinkman model)
3. High viscosity oil with emulsion behavior (Using a tuned Richardson model)
4. Presence of gas in the crude oil feed

For each one of these cases the inlet pressure to the production line with no separator installed ($p_{\text{MPL}}^{\text{NOSEP}}$) was recorded and then the pressure reduction was computed for the 130 combinations of different values of separated stream liquid flow rate (q_{SEP}) and water cut of separated stream (WC_{SEP}). The results are presented using a color map where the x axis is the liquid flow rate of the separated stream, expressed

in % of the total water flow, the y axis is the water cut of the separated stream, and the color scale represents the pressure reduction achieved in the main production pipeline.

The following conditions were also checked for consistency purposes:

- The pressure at the inlet of the production line (p_{MPL}) has to be greater than the pressure at the inlet of the separated stream line (p_{SS}). This to ensure the feasibility of the fluid extraction through the tapping points.
- Only a pressure reduction is plotted, if a pressure increase is registered, the pressure reduction is set to zero ("0").

1. Results of base case

Fig. 1.7 shows the color map of pressure reduction for the combinations of drained flow rate and water cut. The maximum pressure reductions are achieved, as expected, for high separated flow rates and high water content of the separated stream.

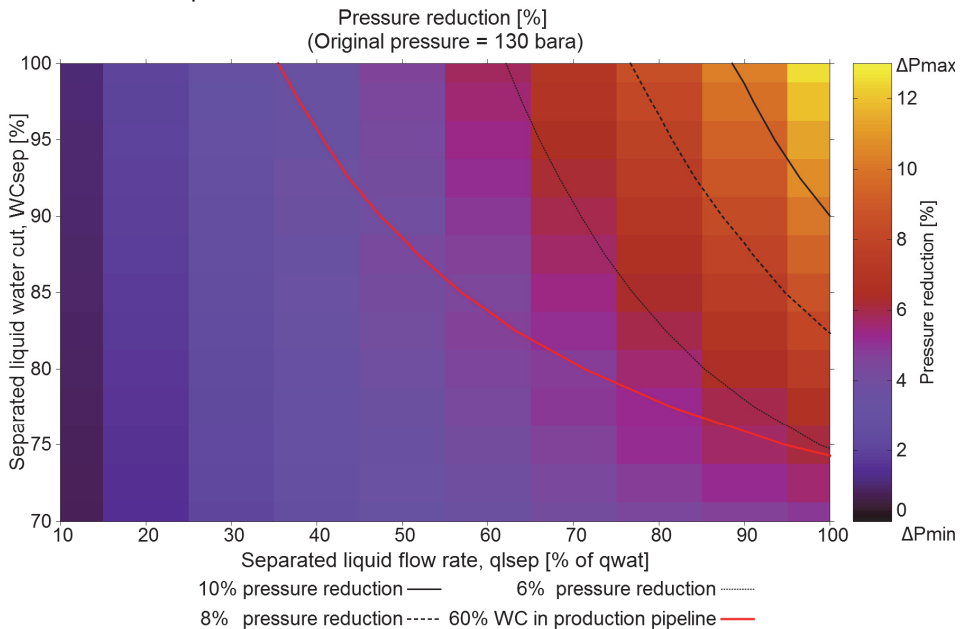


Fig. 1.7 Pressure reduction color map vs Water cut and rate of the separated stream

The highest pressure reductions are obtained for when an oil continuous regime exists in the production pipeline (less than 60% WC). Within this region, Iso-value curves of pressure reduction have been plotted for 6%, 8% and 10%. These curves indicate that the same pressure reduction can be obtained for example either with a high separated liquid rate and low separation efficiency or a lower separated liquid rate but with high separation efficiency. Additionally, for a given separated liquid rate value, an increase in the water cut of the separated stream improves the pressure reduction.

Generally speaking a low separation efficiency is not desired for many reasons but mainly to reduce to a minimum the preprocessing on the FPSO before the deoiling facilities and to minimize the possibility of gas in the deoiling facilities (coming in solution from the oil).

The regions close to the transition line of 60% WC in the production pipeline have a change on trend in the pressure reduction when changing the water cut of the separated stream. This is due to the change of flow regime in the production pipeline from water continuous to oil continuous and vice versa.

It is also important to note that if a relevant (e.g. 5%<) pressure reduction is desired, even if the separator has a high efficiency, more than 50% of the total water rate has to be drained by the inline separator.

These types of plot and iso-curves could be used for design purposes of the inline separator system: for screening the potential benefits of installing the inline separator, for selecting an appropriate operational point and to determine performance requirements of the inline separator. The regions close to the emulsion inversion point in the production pipeline should be avoided because of the previously discussed change in trend.

The pressure difference between the inlet of the production pipeline and the separated stream pipeline ($p_{MPL} - p_{SS}$) is plotted in Fig. 1.8 for all 130 combinations of WC and flow rate calculated earlier. The pressure reduction iso-value curves and the 60% WC line are taken from the previous plot.

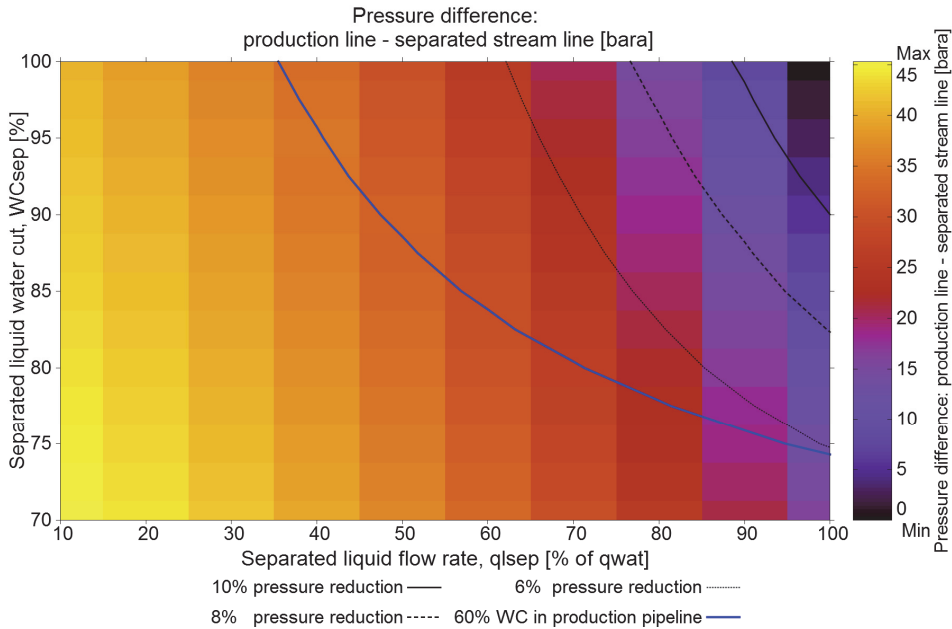


Fig. 1.8 Color map of pressure difference between main line and separated line vs water cut and flow rate

The pressure difference between the inlet to the production pipeline and the inlet to the separated stream pipeline is significant for the majority of points. As the separator intake pressure in general should be very similar to the inlet of the production pipeline (negligible pressure drop in the separator), this indicates that a control valve is required to regulate the flow rate of the separated stream (Fig. 1.9).

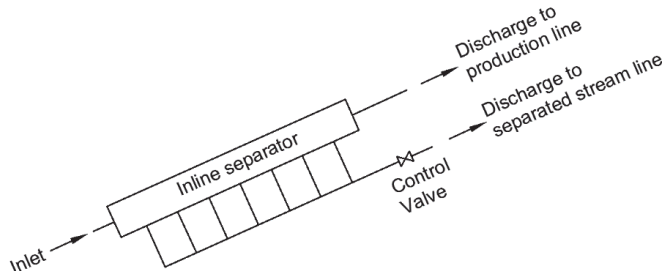


Fig. 1.9 Inline separator operating with a control valve to control the flow rate separated

2. Low viscosity oil with emulsion behavior:

The mixture emulsion behavior in the Pipesim model was activated by using the Brinkman emulsion model (Schlumberger, 2011). The results of this case were very similar to the one presented previously.

3. High viscosity oil with emulsion behavior:

The oil viscosity behavior with temperature was introduced as a 3 points table (Table 1.1). The experimental emulsion viscosity data available vs. water cut was represented by tuning the exponents of the Richardson model (Schlumberger, 2011). The exponents found and the Richardson expressions for mixture viscosity are presented in Table 1.2.

Table 1.1 Viscous oil viscosity dependence with temperature

T [°C]	Oil viscosity [cP]
48.9	858
60.0	374
71.1	186

Table 1.2 Richardson exponents for emulsion viscosity

Regime	Richardson exponent	Emulsion viscosity expression
Oil continuous (WC < 60%)	3.215	$\mu_m = \mu_o \cdot e^{\frac{3.215 WC}{100}}$
Water continuous (WC > 60%)	3.089	$\mu_m = \mu_w \cdot e^{\frac{3.089 (100 - WC)}{100}}$

The color map of pressure reduction of this case is presented in Fig. 1.10. The maximum and minimum values of the color map scale are kept the same as for the base case (from 0 to 13%). A pressure increment rather than a reduction was recorded for cases where the production pipeline is in the oil continuous regime (less than 60% WC). These values have been colored with black in the figure.

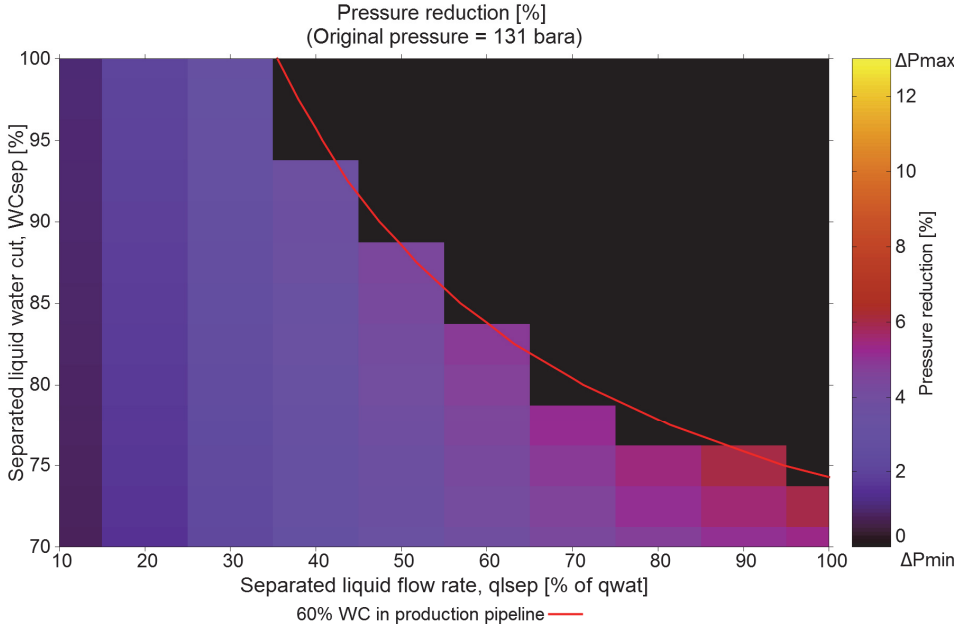


Fig. 1.10 Pressure reduction color map vs Water cut and rate of the separated stream (for viscous oil case)

The maximum pressure reductions registered are confined to high separated liquid rates and low separation efficiency. The maximum is 6.0% which is roughly half the value recorded for the base case. This might indicate that this type of separation is not so beneficial for systems handling high viscosity oils.

4. Effect of gas

The presence of gas was included in the analysis by inputting to the Pipesim model a gas oil ratio (GOR) of 124.7 and a gas specific gravity of 0.65. The simulations are made assuming that the inline separator doesn't drain any gas and that no gas is liberated from the oil after the inline separator. The Pipesim simulator has the capability of modeling these two phenomena, but these assumptions were made to keep the analysis simple.

The color map of pressure reduction of this case is presented in Fig. 1.11. The white color represents points for which the pressure at the inlet of the separated stream pipeline is higher than the pressure at the inlet of the production pipeline, thus an infeasible operating condition.

The maximum pressure reduction registered is 15.6%. It is important to note that the amount of liquid rate of the separated stream has a greater impact in the pressure reduction than the water cut. These results for this particular system indicate that when gas is present in the system it is beneficial to drain liquid, without caring much about its water content.

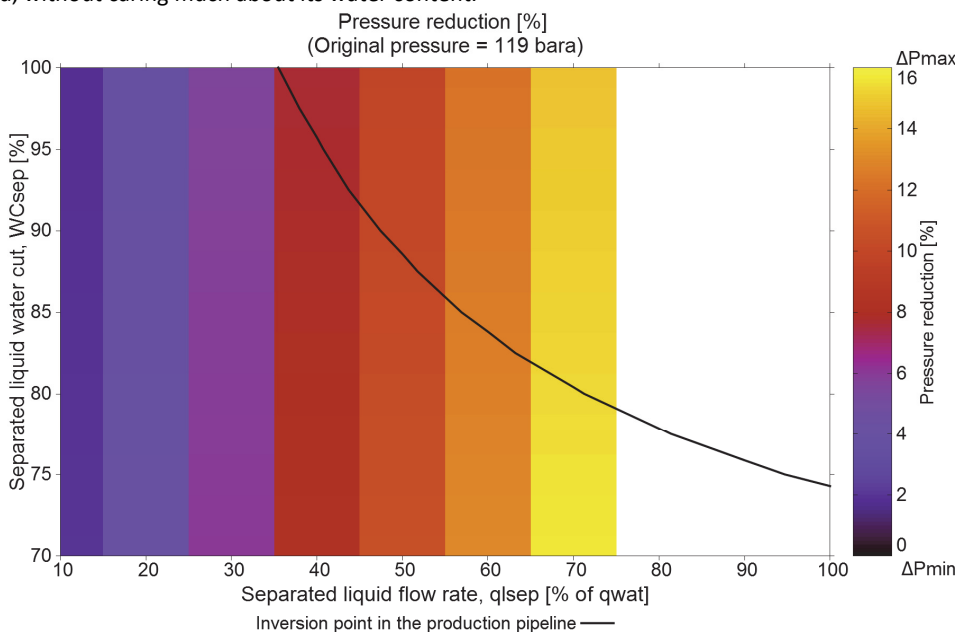


Fig. 1.11 Pressure reduction color map vs Water cut and rate of the separated stream (for gas case)

These results indicate that it is possible to define for a particular case a required operational envelope for the inline separator with the help of simulation tools. It can be assessed later if the inline separator is capable of delivering the required combinations of flow rate and water cuts and then take the operational decision of going forward or not with the implementation. A custom analysis for each case is strongly advised. It is also recommended to include the production system upstream the separator.

1.3 Inline separation definitions, design principles and strategies

A distinctive characteristic of the inline segregation/separation process is that it is occurring while the fluids are flowing (i.e. possess relevant velocities), contrary to what happens in a bulk separation vessel. Additionally the separation depends of two interrelated phenomena: the amount of "clean" water that is transported at the bottom of the pipe and the capability of the tapping point to drain this fluid stream. These distinctive characteristics motivated the introduction of some new concepts and methodologies to quantify the separation efficiency and performance. This section is divided in the following parts:

- A methodology for determining the separation performance of a single tapping point is presented and discussed. Unfortunately no experimental data is available to observe how this performance looks like, so an alternative estimation methodology using single pipe values is presented and discussed next.
- A methodology for estimating the single tapping point performance from single pipe values/no tapping situation is presented and discussed. The limitations of this approach are also discussed.
- The drainage performance of a single tapping point is presented in a phase superficial velocity map. Some practical observations are discussed.
- The separation employing a multiple tapping point arrangement is addressed using the phase superficial velocity maps.

1.3.1 Concept of single tapping point separation performance

A general methodology to quantify (e.g. experimentally) the separation performance of an “isolated” tapping point is provided next.

Consider the set up presented in Fig. 1.12. Water and oil (of known properties) are circulating in a pipe separator with flow rates q_o and q_w . A series of experiments are run by varying the liquid drainage flow rate (q_t) from values close to zero up to the total liquid rate $q_o + q_w$. For each one of these points the water cut of the drained stream is recorded (WC_t) and the tapped oil and water flow rate are calculated (q_{ot} , q_{wt}). The resulting set of values can be organized in a table or presented in a plot. Please note that any pair of values in one row can accurately define the others.

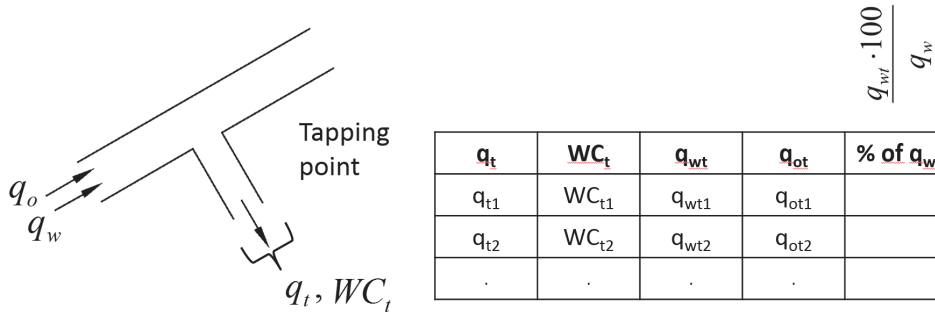


Fig. 1.12 Simplified setup to quantify the separation performance of a single tapping point

An additional variable can be computed by dividing the tapped water flow rate q_{wt} by the total water flow rate carried by the pipe q_w . This value expresses what fraction of the total water flow rate carried by the pipe is being tapped by the tapping point.

The information in the table fully characterizes the separation performance of a tapping point. For simplicity reasons, this set of values will be referred to as “Drainage potential”. The Drainage potential depends primarily on:

- Oil and water properties
- Oil and water flow rates
- Separator configuration (pipe diameter, inclination from the horizontal)
- Tapping point configuration (tapping point size, orientation, orifice shape)

For the present study the effect of the shear stress history of the fluid, the wettability of the walls, the presence of demulsifiers or surfactants, entry or upstream effects are not considered.

From the tapping planning point of view, the drainage potential can be used in two different ways:

- Specify the desired water cut of the separated stream and interpolate in the table to obtain the liquid flow rate that will be drained or
- Specify the desired liquid liquid flow rate to drain and interpolate in the table to obtain the water cut of the separated stream.

The drainage potential can be employed to compare two different separator configurations or tapping point configurations: for example setting the desired water cut of the separated stream and then selecting the configuration that yields the highest water flow rate tapped of the two.

In this discussion the total liquid flow drained (q_t) has been varied up to the total liquid rate of the pipe ($q_o + q_w$) for keeping the generality. However, for practical applications, the upper limit of (q_t) should be limited to the total water rate, as it is of no interest to drain more.

It is important to note that the drainage potential reveals information about two superimposed phenomena: (1) the phase distribution in the main pipe as defined by the dynamics of the multiphase flow upstream the tapping point and (2) the effect of the tapping point on the multiphase flow dynamics.

1.3.1.1 Estimation of the Drainage potential using single pipe/no tapping values

Unfortunately no experimental data is available to see how the single tapping point drainage potential looks like, so an alternative estimation methodology is proposed in this section using single pipe values.

The drainage potential can be also estimated if the phase velocity and volume fraction distribution in the main pipe are known (for flow conditions with no drainage) and if some assumptions are made:

- The tapping point is draining from only one direction (either upstream or downstream)
- The shape of the cross section area drained by the tapping point is known and
- The presence of the tapping point doesn't modify in a significant way the multiphase flow dynamics of the oil in water dispersion in the main pipe as compared with the case where no tapping is performed.

The validity of this assumptions are discussed after presenting the methodology.

The present study is focused on the specific case where the multiphase mixture is arranged spatially as a dispersion of oil in water. Fig. 1.13 shows the cross section view of a pipe were an oil in water dispersion is flowing.

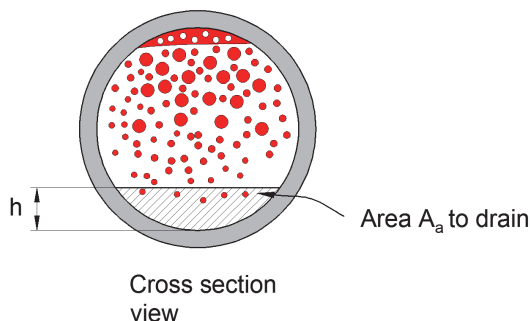


Fig. 1.13 Cross section of a pipe displaying the area to drain

An area " A_a " of interest (i.e. to be drained), has been defined arbitrarily based on a height " h " from the bottom of the pipe. The flow rates of oil and water that are being transported in this layer (q_w and q_o) can be estimated by integrating on area " A_a " the product of the axial phase velocity (V perpendicular to the cross section) and the phase volume fraction (α) as indicated in Eq. 1.2 and Eq. 1.3 respectively:

$$q_w = \int_{A_a} \alpha_w \cdot V_w \cdot dA \quad \text{Eq. 1.2}$$

$$q_o = \int_{A_a} (1 - \alpha_w) \cdot V_o \cdot dA \quad \text{Eq. 1.3}$$

The water cut (WC) of this area is estimated according to Eq. 1.4

$$WC = \frac{q_w}{q_w + q_o} \cdot 100 \quad \text{Eq. 1.4}$$

The drainage potential values can be determined in the following manner (Fig. 1.14): vary the height “h” from a value of zero (0) to the diameter of the pipe (assuming a flat interface). Compute for each one of these heights the oil and water flow rate transported by the layer and the water cut.

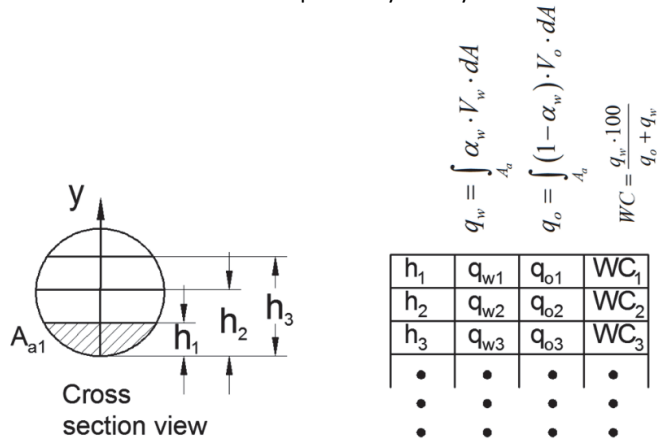


Fig. 1.14 Drainage potential quantification procedure

The amount of clean water transported at the bottom of the pipe depends mainly on two factors: the water velocity and the water volume fraction. Usually in inclined dispersed oil in water flow patterns there is a balancing effect between this two parameters: for high inclinations the water segregation increases, but the fluid at the bottom of the pipe moves with a slow velocity (Fig. 1.15 a); while for low inclinations the water segregation diminishes but the fluid at the bottom of the pipe is moving faster (Fig. 1.15 b).

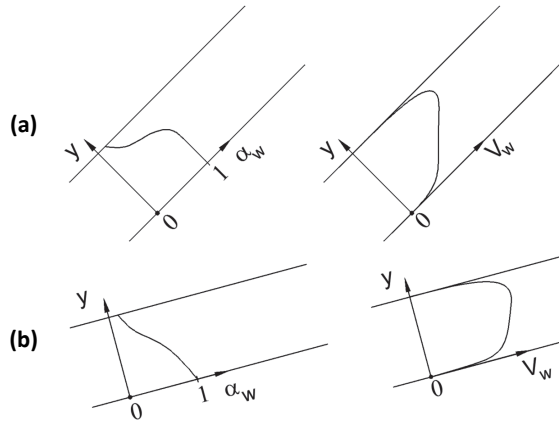


Fig. 1.15 water volume fraction and velocity distribution along the diameter for high inclination (a) and low inclination (b)

As a demonstration example the drainage potential estimation procedure has been applied to cross section values of axial velocity and water volume fraction extracted from fig. 8.51 from Elseth (2001). It was assumed that the two phases travel at the same velocity. The values are available only along the pipe diameter (axis y in Fig. 1.14) thus the integration was performed using a 1D approach (presented in Appendix A1). The mixture velocity is 1.02 m/s, the water cut is 85%, horizontal 56 mm ID pipe. The result of the integration is presented in Fig. 1.16 by plotting the percentage of total water flow rate drained vs water cut in the drainage area.

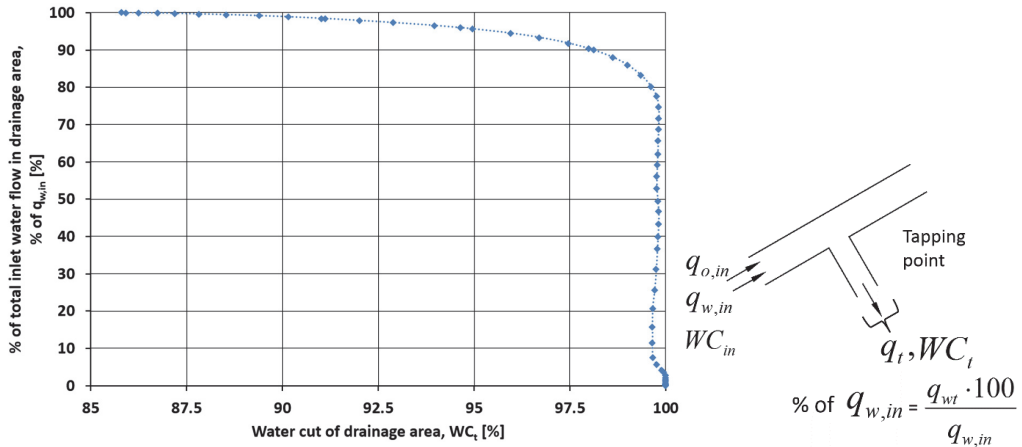


Fig. 1.16 Sample drainage potential curve

It is important to note that the minimum water cut of the figure obtained by integration is 85.8%, when the correct value is 85%. This might be caused by several factors: the 1-D approximation for the cross section integration, the uncertainty associated with the experimental data or the assumption that the phases travel at the same velocity for a given cross section position (no slip).

From the tapping planning point of view, this drainage potential curve can be used in two different ways:

- Specify the desired water flow rate to drain and read the water cut of the separated stream (Fig. 1.17 a)
- Specify the desired water cut of the separated stream and read the water flow rate that will be drained (Fig. 1.17 b).

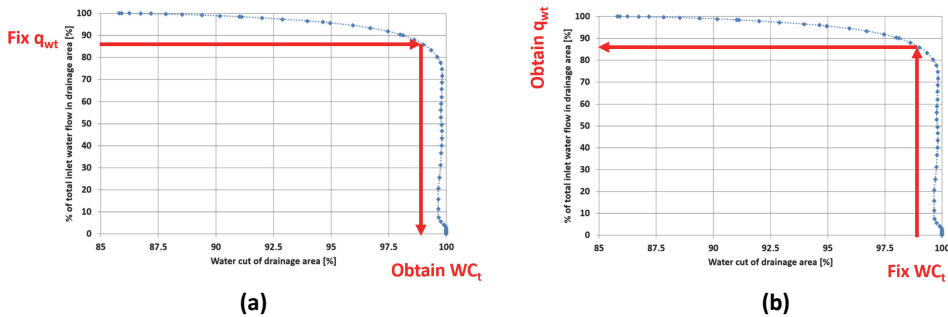


Fig. 1.17 two different ways to use the drainage potential curves for tapping planning and design

It is also important to note that, if the integration is done from a height “h” equal to zero up to the pipe diameter, the beginning and end point of the curve are known (as presented in Fig. 1.18): the curve should begin at water cut equal to 100% for 0% water flow drained (if there is water accumulation at the bottom of the pipe) and should finish at the total water cut of the mixture when 100% of the water is drained through the tapping point (when the height is equal to the pipe diameter). This observation suggests that the drainage potential might be represented employing a catenary function, where the exponent can be adjusted to represent the shape of the curve between the two points.

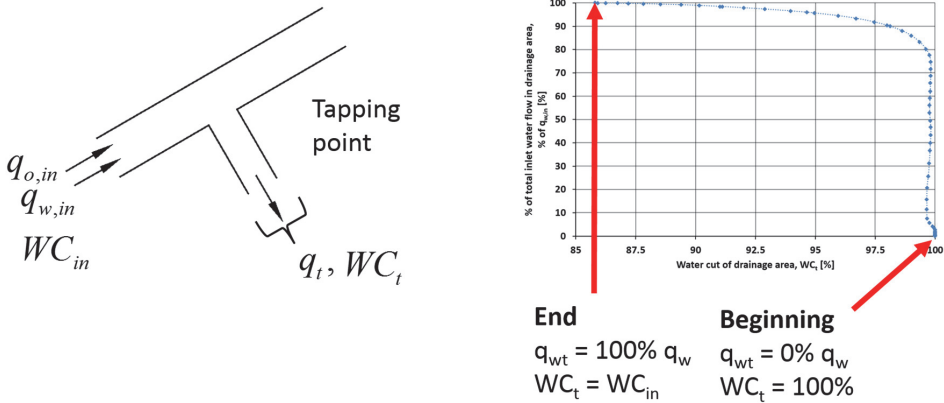


Fig. 1.18 Beginning and end of the drainage potential curve: tapped water flow rate vs tapped stream water cut

Deviations between the actual measured and estimated drainage potential

There might be a deviation between the drainage potential estimated numerically from a no tapping situation and the actual drainage potential. This is due mainly to the disturbances in the oil in water dispersion flow caused by the tapping point. For example the tapping could change the velocity distribution in the cross section upstream the tapping point (create a “sucking” effect) and consequently to change the phase segregation. In consequence, the approaching velocity and volume fraction profiles might be different from those in the case where there is no drainage.

If the tapping point flow rate is high enough, it might induce drainage both from locations upstream and downstream the tapping point thus invalidating the assumption of a unique approaching direction. The tapping point might not drain exactly the bottom layer defined previously, i.e. the actual drainage cross section area might have a different shape from the one defined in the previous section. A workaround for this is to assume a different drainage area shape and compute the drainage potential curve for that area. Some examples of other different cross section drainage areas are presented in Fig. 1.19.

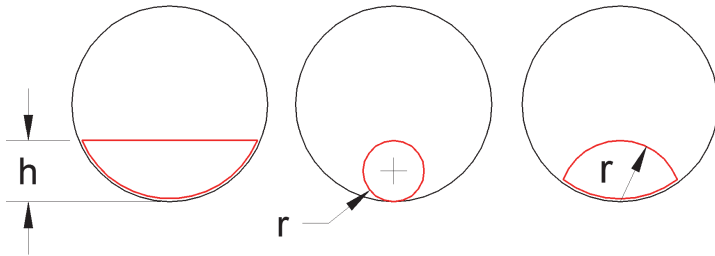


Fig. 1.19 Different proposals for drainage area in the cross section to compute the drainage potential

Intuitively speaking, if the tapped liquid flow rate is low enough, it is unlikely to create any relevant disturbance in the flow in the main pipe so the drainage potential estimation from a no tapping situation would give a good approximation. If, on the contrary, the tapping points introduces important disturbances, there will be a big deviation between real and estimated drainage potential.

For the present study it will be assumed that the tapping point is designed appropriately (with regards to size and orientation) for taking the amount of flow that it is supposed to drain without causing much disturbances to the main fluid stream.

1.3.1.2 Visualizing the drainage potential in a phase superficial velocity map - Separation Triangle with unit slope

Consider a x-y scatter plot where the oil superficial velocity (V_{so} : oil flow rate divided by pipe cross section area) is in the x axis and the water superficial velocity (V_{sw}) is in the y axis. If a given combination of oil and water flow rates approaching a tapping point is given (q_{o1}, q_{w1}) and the pipe diameter is known, it is possible to locate this point on the map (Point 1 in Fig. 1.20, V_{so1}, V_{sw1}).

Consider that a total liquid rate (q_{lt}) is being drained by the tapping point. As discussed earlier, in principle the drained stream might have a water cut ranging from 100% to the original water cut of the main stream (WC_1). If all of those possible drained water cuts are deducted from the initial conditions “1” (keeping the liquid flow rate q_{lt} drained constant) all the possible resulting values downstream the tapping point (2) lie in a line shown in Fig. 1.20.

Please note that the upstream point (1), the best downstream case (2) and the worst downstream case (2) form a triangle. This triangle will be referred to as the “Separation Triangle”. The deduction of the 45° angle is presented in detail in Appendix B1.

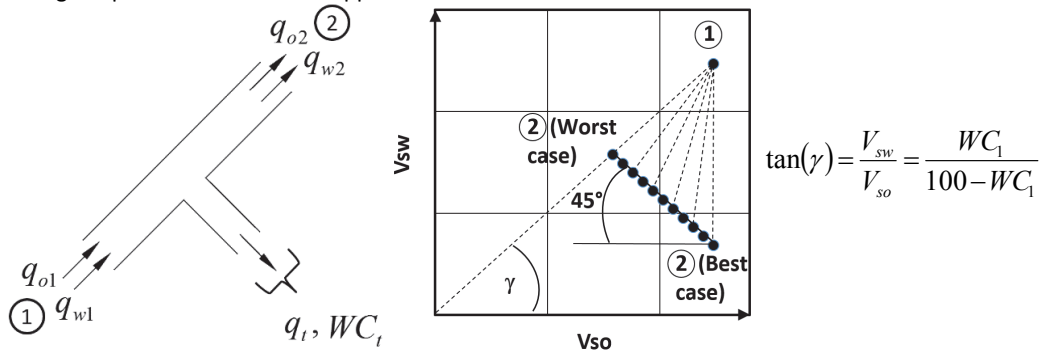


Fig. 1.20 Representation of all possible separation efficiencies in a superficial velocity plot (fixed separated rate)

In reality each drained flow rate (q_{lt}) has a **unique** (physically feasible) water cut (WC_1) as given by the drainage potential curve (i.e. only one point on the line is physically feasible). This applies for every drained flow rate value.

As an example with real data, all the pairs presented in the drainage potential curve calculated in Fig. 1.16 are subtracted to the initial oil and water superficial velocities and are plotted in Fig. 1.21.

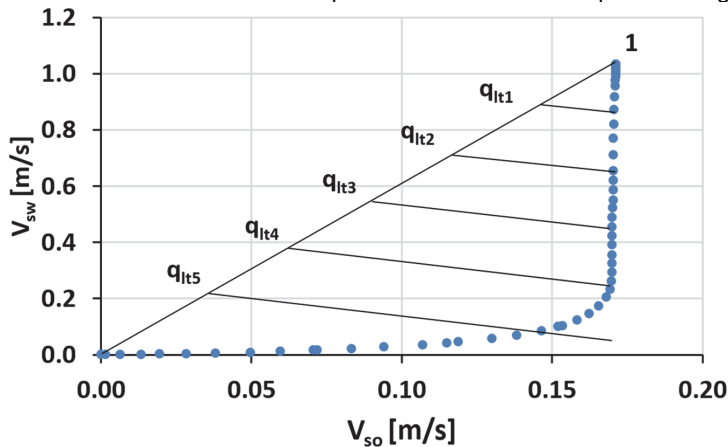


Fig. 1.21 Drainage potential presented in a phase superficial velocity map

It is possible to see the same trend as in the drainage curve: up to a certain value of drained flow rate the water content of the resulting condition downstream the tapping point remains more or less constant. However there is a turning point (after q_{lit4} in the figure) where more and more oil begins to be drained by the tapping point.

It is desirable, for separation performance purposes, for the drainage potential of a point in the phase superficial velocity map to have a shape as vertical as possible (like in Fig. 1.21). This is because more water can be drained with a low oil content.

Please note that **every** combination of oil and water superficial velocities in the map **has a drainage potential**. Remember that the drainage potential is associated to a particular pipe inclination and diameter, fluid properties, tapping point configuration, etc.

1.3.2 Performance of a multiple tapping point arrangement

The inline separator consists of an arrangement of tapping points to drain sequentially the water rich layer located at the bottom of the pipe. For the discussion presented next a main assumption taken is that the performance of an arrangement of multiple tapping points can be safely predicted by adding the performance of each individual tapping point.

This assumption might not be valid if there is not sufficient distance between the tapping points to ensure that a new momentum equilibrium in the phase velocity and distribution profile is achieved. Additionally the turbulence and mixing created by the drainage in one tapping point could also affect the performance of the next tapping point.

Consider the situation given in the phase superficial velocity plot of Fig. 1.22. The inlet conditions to an inline separator have been given (tagged “in” in the figure) and a certain total liquid rate to be drained is fixed (q_t in the figure). The purpose is that the outlet of the separator (tagged “out” in the figure) to be located as close as possible to the vertical line passing through the inlet conditions. The area inside the Separation Triangle is the separator domain. Let’s assume, for the sake of the discussion, that all the drainage potential is known for all the points inside this triangle (e.g. from experimental measurements on a given single tapping inline separator geometry).

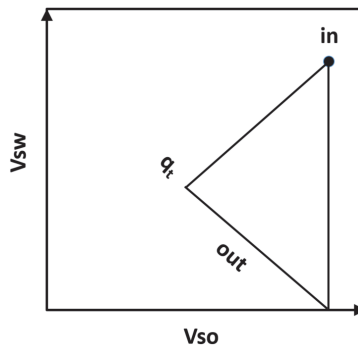


Fig. 1.22 Inlet and all possible outlet conditions of the inline separator plotted in a phase superficial velocity plot

Let’s consider three types of draining strategies for the inline separator (all of them with 6 tapping points): Uniform distributed tapping (Fig. 1.23 a), gradually increasing tapping (Fig. 1.23 b) or gradually decreasing tapping (Fig. 1.23 c).

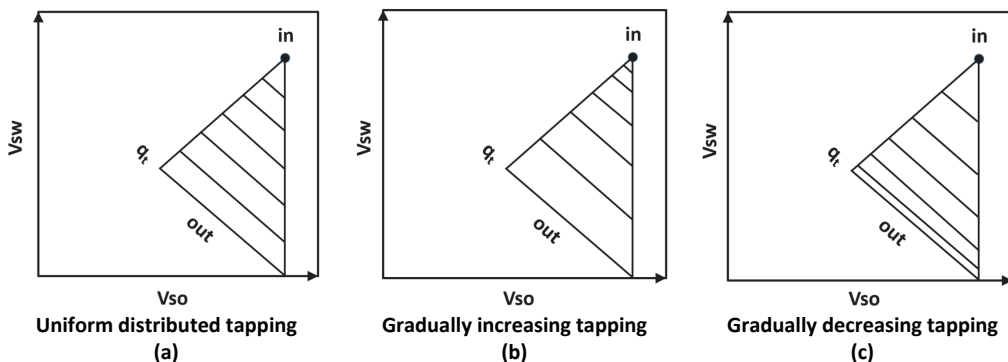


Fig. 1.23 Different drainage strategies proposed for the inline separator

If the drainage potential is known for every point inside the main triangle in the phase superficial velocity map then the separator outlet for each one of this separation strategies can be computed, and the best among the three of them can be selected. One example of this process with fictitious data is shown in Fig. 1.24. Please note that, for the particular invented data, it is more beneficial to drain the flow rate q_t using only one tapping point.

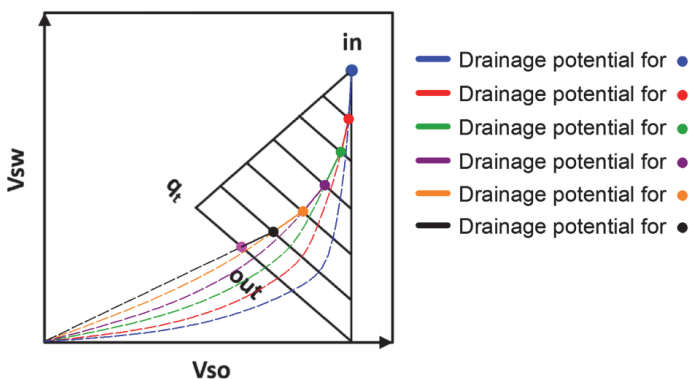


Fig. 1.24 Fictitious example of calculating the separator output with a uniform tapping strategy and the drainage potential

1.4 Separation analysis using experimental data

In this section some selected data from the literature and from the study of Rivera (2011) are analyzed. The main purpose is to emit some observations about best configurations for best separation efficiency, based on concepts introduced previously.

1.4.1 Effect of pipe inclination in drainage potential – estimation from literature data

The drainage potential curve, specifically the drained percentage of total water flow vs water cut of the drained stream, was estimated (as presented in section 1.3.1.1, and described in Appendix A1) from experimental velocity and volume fraction profiles available in the literature (Kumara et al. 2010, Amundsen et al 2011). The data corresponds to a mixture velocity of 1.00 m/s, water cut of 50% (stratified flow), pipe diameter 56mm and for inclination angle from the horizontal: -10° , 0° , 5° , 10° . The fluids used are Exxsol D60 and tap water.

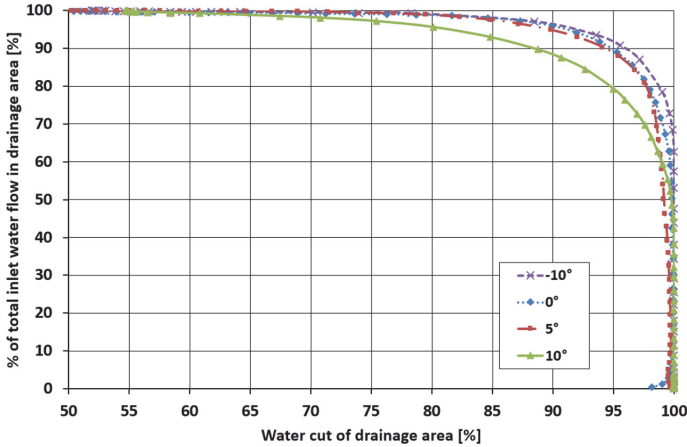


Fig. 1.25 Percentage of total inlet water flow drained vs water cut of drained stream

The figure indicates that, for a given water cut of the drainage area, lower inclinations (even below the horizontal, -10°) yield more water in the separated stream. It is important to note that it is not recommended to tap flow rates greater than 95% the total inlet water flow because the water cut of the drained decreases very rapidly.

1.4.2 Separation assessment based on experimental data of the separation prototype of Rivera (2011)

The experimental work of Rivera (2011) was focused on testing a prototype of the inline separator. This consisted of measuring and quantifying experimentally the performance of the separator under a combination set of inlet conditions and separator characteristics.

The experimental bench consisted on a 5 m horizontal pipe section followed by a 5 m inclined pipe section (both of 154 mm ID). The 5 m inclined pipe section had 5 tapping points (2 inch ID) uniformly distributed where the flow rate was controlled using a needle valve, and the flow rate was measured with a turbine flow meter. Quick closing valve arrangements were installed at each tapping point for measuring the water cut of each tapping point (Fig. 1.26). The water holdup of the tapping point was calculated reading the oil and water levels from a graduated container.

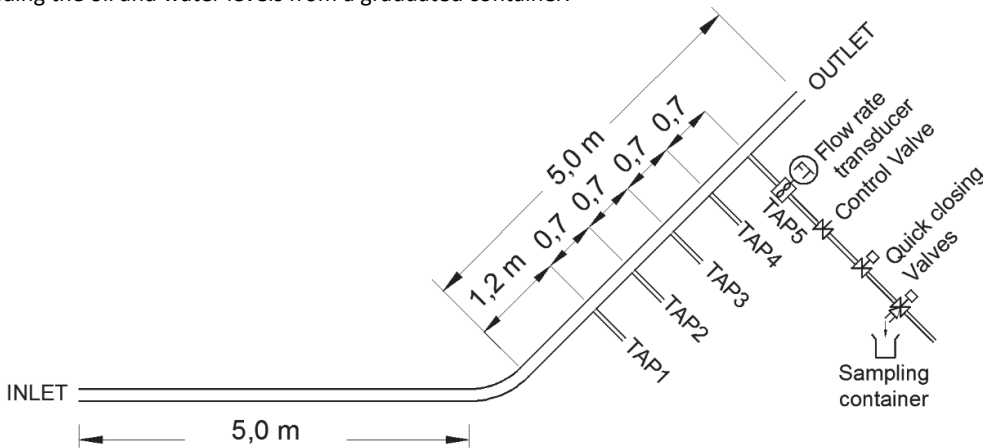


Fig. 1.26 Experimental setup for Rivera (2011)

Observations about the experimental setup and measurement campaign of Rivera (2011)

- The tapping flow rate measurements have a 2% accuracy (as given by the turbine flow meter manufacturer).
- The measured tapping water holdup has a very acceptable accuracy (as estimated by the author using partial derivatives method). This is because the graduated cylinder employed had a reading precision of 0.1 ml.
- Please note that the tapping points are relatively close to each other (4.5 D). This distance might not be enough to ensure that the multiphase flow is developed from one tapping point to another.
- The elbow between the horizontal and inclined section might affect the multiphase dynamics in the inclined section (entry effects).
- Rivera considered that the conditions approaching any tapping point can be estimated by deducting what has been drained by the previous tapping point (Fig. 1.27). In this approach the water cut of the tapping point has been assumed equal to the water holdup of the tapping point.

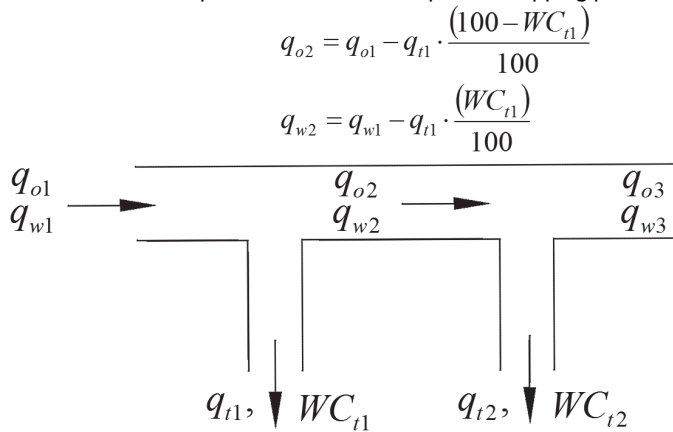


Fig. 1.27 Calculating the oil and water flow rates approaching a tapping point

- The Oil water flow regimes in inclined pipes were classified according to the nomenclature presented by Brauner (2004) (as presented in Table 1.3)

Table 1.3 Flow regimes in upwards inclined oil-water flows

Water dominated flow regimes		
Intermittent dispersion of oil in water and water	Dispersion of oil in water and water with backflow	Transitional flow
I Do/w & W	Do/w & W BF	TF
Dispersion of oil in water and water	Dispersion of oil in water	
Do/w & W	Do/w	

1.4.2.1 Influence of inclination on oil content of tapped flow

The main objective of this section is to determine if the inclination has an impact on the amount of oil drained by a tapping point (Fig. 1.28). This analysis was performed based on a single tapping point geometry.

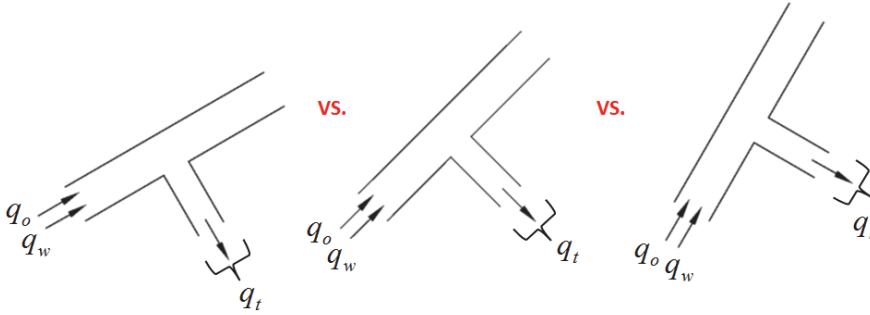


Fig. 1.28 Different inclinations to drain a liquid flow rate q_t

The experimental data was revisited and 39 single tapping experimental measurements were extracted. These experimental points had (approximately) the same upstream oil and water flows and the same tapping flow while the separation inclination from the horizontal varied from 30° to 60°. These points were grouped in 13 different cases (according to the upstream oil and water flows and tapping flow) and are presented in Table 1.4 .

Table 1.4 Oil volume fraction in tapped stream depending on the inclination for multiple inlet conditions

Pipe inclination from horizontal:				30°	45°	60°
Water flow	Oil flow	WC	Tapping flow	Tapping oil volume fraction	Tapping oil volume fraction	Tapping oil volume fraction
[lpm]	[lpm]	[%]	[lpm]	±0.1 [%]	±0.1 [%]	±0.1 [%]
80.0	80.0	50.0	3.8	0.5	5.0	5.0
40.0	80.0	33.3	4.2	0.5*	1.9	12.1*
20.0	80.0	20.0	4.1	0.5	2.5	8.9*
300.0	120.0	71.4	15.0	0.0	4.6	2.4
250.0	120.0	67.6	15.0	1.9*	4.9*	6.1*
200.0	120.0	62.5	15.0	0.5	4.1	8.8
150.0	120.0	55.6	15.0	2.8*	6.6*	6.0*
100.0	120.0	45.5	15.0	1.9	8.7	15.2
50.0	120.0	29.4	15.0	4.7*	12.5*	23.8*
250.0	27.0	90.3	5.5	0.5	0.5	0.5
150.0	27.0	84.7	5.0	0.5*	0.5*	0.5*
75.0	27.0	73.5	5.0	0.5*	0.5*	0.5*
25.0	27.0	48.1	5.0	1.0	1.0	1.0
	I Do/w & W		D o/W & W BF		D o/W & W	
	TF		Do/w			

*Experimental values corresponding to the first tapping point

For 7 cases as inclination increases the oil content of the tapped stream also increases. For 4 cases there was no change in the tapped stream oil content with inclination. These cases had flow patterns Do/w & W and I Do/w & W. Lastly 2 cases exhibited a peak in oil content of the tapped stream at 45°.

These results seem to indicate, with some exceptions, that less oil will be tapped with a low inclination of the inline separator. These observations are limited to the operational range tested by Rivera (2011).

1.4.2.2 Effect of the number of tapping points on the amount of oil drained.

The main objective of this section is to determine if the number of tapping points chosen to drain a total amount of flow (q_t) has an impact on the amount of oil drained (Fig. 1.29). For that purpose the experimental data of Rivera (2011) was revisited and 21 cases (presented in Table 1.5) were extracted.

Inlet: q_o, q_w

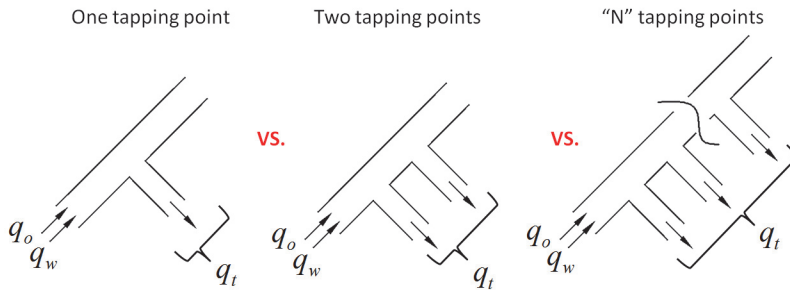


Fig. 1.29 Different number of tapping points chosen to drain a total amount of flow q_t

Due to the manner how the measurements were taken, it was not possible to make a comparison between more than two numbers of tapping points for the same inlet conditions and the same total flow tapped.

Table 1.5 Selected experimental points with the same upstream conditions, total flow drained but different number of tapping points

Inlet Flow pattern	Total flow tapped [lpm]	Inlet oil flow [lpm]	Inlet water flow [lpm]	N° of Tappings	Oil flow tapped [lpm]	Error in oil flow tapped [lpm]	Increment in oil flow tapped [%]
45°, I Do/w & W, 85 lpm W, 27 lpm O	10.8	25.0	85.0	1	0.05	±0.01	0
	10.5	27.0	85.0	2	0.05	±0.01	0
	17.0	27.0	85.0	1	0.13	±0.02	-38
	15.8	27.0	85.0	3	0.08	±0.02	-38
	21.4	25.0	85.0	2	0.11	±0.02	0
	20.8	27.0	85.0	4	0.10	±0.02	0
	33.4	27.0	85.0	2	0.25	±0.04	-36
31.5	25.0	85.0	3	0.16	±0.03	-36	
45°, Do/w & W, 250 lpm W, 28 lpm O	10.0	28.0	250.0	1	0.05	±0.01	0
	10.1	27.0	250.0	2	0.05	±0.01	0
	16.6	28.0	250.0	1	0.21	±0.02	-67
	14.9	27.0	250.0	3	0.07	±0.02	-67
	20.7	28.0	250.0	2	0.10	±0.02	0
	20.0	27.0	250.0	4	0.10	±0.02	0
	25.1	28.0	248.0	1	0.00	-	+100
	25.0	27.0	250.0	5	0.12	±0.03	+100
	33.0	28.0	250.0	2	0.39	±0.04	-59
31.0	28.0	250.0	3	0.16	±0.03	-59	
50.5	28.0	248.0	2	0.00	-	+100	
51.4	28.0	250.0	5	0.26	±0.06	+100	
45°, Do/w & W, 166 lpm W, 27 lpm O	10.9	27.0	163.0	1	0.05	±0.01	0
	10.1	27.0	166.0	2	0.05	±0.01	0
	16.7	28.9	166.0	1	0.07	±0.02	0
	15.1	27.0	166.0	3	0.08	±0.02	0

	21.9	27.0	163.0	2	0.11	±0.02	0
	20.2	27.0	166.0	4	0.10	±0.02	
	25.1	28.0	164.0	1	0.00	-	+100
	25.2	27.0	166.0	5	0.13	±0.03	
	32.9	28.9	166.0	2	0.19	±0.04	0
	32.3	27.0	163.0	3	0.16	±0.04	
	50.4	28.0	164.0	2	0.00	-	+100
	53.3	27.0	163.0	5	0.27	±0.06	
45°, TF, 127 lpm W, 85 lpm O	15.8	85.0	127.0	1	1.19	±0.04	+32
	13.0	88.0	135.0	2	1.57	±0.05	
45°, Do/w & w BF, 80 lpm W, 80 lpm O	8.1	80.0	81.0	1	0.32	±0.01	+78
	8.2	82.0	80.0	2	0.57	±0.02	
	15.7	80.0	81.0	2	0.79	±0.03	+82
	16.2	82.0	80.0	4	1.44	±0.05	
45°, Do/w & w BF, 80 lpm W, 40 lpm O	8.6	40.0	80.0	1	0.36	±0.02	-25
	7.9	41.0	81.4	2	0.27	±0.01	
	16.6	40.0	80.0	2	0.81	±0.03	0
	16.2	41.0	81.4	4	0.82	±0.03	

For 9 cases there was neither an increase nor a decrease in the amount of oil tapped when increasing the number of tapping points. For 7 cases there was an increase in the amount of oil tapped when increasing the number of tapping points. For 5 cases there was a decrease in the amount of oil tapped when increasing the number of tapping points.

It is important to highlight that those cases that exhibited a decrease in the amount of oil tapped when increasing the number of tapping points had a slightly smaller tapping flow for more tapping points. These results seem to indicate, with some exceptions, that increasing the number of tapping points used for the extraction doesn't reduce the amount of oil tapped.

1.5 Evaluating the capability of a CFD model to represent the segregation and separation phenomena in oil in water dispersions

The work presented in this section has been published in the International Conference of Multiphase Flow in Jeju, Korea 2013 and is included as a reference in Appendix E1.

A three dimensional Computational Fluid Dynamics (CFD) model is proposed as a way of reproducing the multiphase flow fluid dynamics inside the inline separator. The main motivations to create the model are: to have a tool for analyzing in detail the internal fluid dynamics of the inline separator, to perform numerical experimentation and to be able to predict separator performance. A canned commercial simulator called Ansys CFX is employed to create, run and visualize the results of the model. The guideline followed for the development of the model is for it to require as little customization (i.e. input data) as possible.

The objective of this section is to evaluate the prediction capacity of the CFD model for dispersed oil in water flows and to define an appropriate modeling approach to employ for future analysis. This is performed by reproducing five (5) selected experimental cases taken from the literature and comparing the results of the CFD model with the measurements available.

1.5.1 Selected experimental data from the literature

The selected experimental cases used in the present study are shown in Table 1.6. The physical properties of the fluid of each one of these studies is presented in Table 1.7. The experimental data available is presented in table Table 1.8. The inclination angle from the horizontal is represented by θ .

Table 1.6 Experimental cases simulated in the present study

N°	Flow pattern	Source	V_M [m/s]	WC [-]	θ [°]	D [m]
1	Do/w&w	Kumara et al. (2009a)	1.50	0.75	0	0.056
2	Do/w&w/o	Kumara et al. (2009b)	1.06	0.75	0	0.056
3	lDo/w&w	Tabeling et al. (1994)	0.12	0.90	25	0.200
4	Do/w&w	Vigneaux et al. (1988)	0.47	0.90	25	0.100
5	Do/w&w BF	Tabeling et al. (1994)	0.12	0.50	65	0.200

Table 1.7 Physical properties of the experimental fluids for each case

	Oil	ρ_w [kg/m ³]	ρ_o [kg/m ³]	μ_w [mPa s]	μ_o [mPa s]	σ [mN/m]
1&2	Exxol D60	996	790	1.00	1.64	43.0
3&5	Kerosene	996	779	1.00	5.00	47.0
4	Kerosene	996	740	1.00	2.05	47.0

Table 1.8 Experimental information available for each case

N°	α_w profile	V_M profile	H_w [-]	Image	dp/dx [Pa m ⁻¹]
1	A	NA	0.69	A	431.0
2	A	A	0.70	A	213.6
3	A	NA	0.97	NA	NA
4	A	NA	0.94	NA	NA
5	A	NA	0.67	NA	NA

NA Non available, A Available

1.5.2 Background information about the CFD model employed

Computational Fluid Dynamics (CFD) is the utilization of computational methods to solve fluid flow problems and its interaction with contours. This is done by solving the differential conservation equations together with correlations or particular models that represent the physical phenomena using numerical methods.

The canned simulator Ansys CFX employs the Finite Volume Method for solving these equations. Summarizing, it consist on subdividing the fluid domain of interest in small subdomains or “volumes” and to integrate the equations on each one of them. The result is a set of algebraic equations that are solved using numerical methods.

There are many variations of CFD methods for multiphase flow in the literature, but for the present study the particle approach is chosen. Its fundamental assumption is that the phases are arranged in a dispersion where water is the continuous phase and oil is the dispersed phase.

Separated conservation equation of mass and momentum are usually solved for the continuous and dispersed phase using the Euler-Euler formulation (Ansys 2010). The conservation equations include interfacial interaction terms to account for the momentum exchange between the dispersed phase and continuous phase. The interfacial interaction terms considered are the following:

- Buoyancy
- Drag force
- Lift force
- Lubrication force
- Turbulent dispersion force

This terms are estimated through equations derived from theoretical fundamentals that usually include variables that have to be calculated from correlations. This expressions are preprogrammed in the canned commercial software.

1.5.2.1 Treatment of the dispersed phase in the CFD simulator

There are several approaches available in the CFD software to model the dispersed phase. They can be classified in two main categories: (1) Dispersions that exhibit a unique droplet size (also called monodispersions) and (2) dispersions that exhibit several droplet sizes (also called polydispersions). In the present study the following approaches were considered:

- Single oil droplet size with a fixed diameter “d” (given as an input).

The starting dispersion diameter value was the Sauter mean diameter (d_{32}) obtained from the results of a droplet size distribution function (Upper log-limit normal or ULLN) as discussed in detail in Appendix C1. This value was then increased or decreased manually depending on the quality of the prediction. The maximum diameter and the Sauter mean diameter obtained by the ULLN function for the experimental cases are shown in Table 1.9.

Table 1.9 Maximum droplet diameter and Sauter mean diameter predicted by the ULLN model

N°	V_M [m/s]	WC [-]	d_{MAX} * 1e-3 [m]	d_{32} * 1e-3 [m]
1	1.50	0.75	1.19	0.33
2	1.06	0.75	1.40	0.39
3	0.12	0.90	9.77	2.68
4	0.47	0.90	2.35	0.64
5	0.12	0.5	27.98	7.68

It is important to note that for cases 1 and 2 the maximum diameter predicted (0.3 mm) is considerably less than the average droplet diameter exhibited in the experimental photos (~3 mm, Fig. 4. of Kumara et al. 2009b).

- “N” characteristic oil droplet sizes (also called “classes”, as seen in Fig. 1.30), each one with a fixed diameter “d” and an associated size fraction (given as input). Size fraction is defined as the volume of oil contained in droplets of diameter “d” divided by the total volume of oil. In this study N=2 and N=4 were tried.

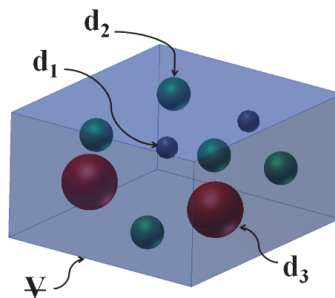


Fig. 1.30 A 3 droplet class dispersion of oil in water

The droplet diameter values and their corresponding size fraction were taken from: (1) the results of a droplet size distribution function as shown in Appendix C1, (2) manual modification by the author to improve the prediction.

- 5 characteristic oil droplet classes, equally spaced between a fixed minimum droplet diameter and a maximum droplet diameter (given as an input). The size fraction of each droplet class in each part of the system is calculated by a population balance that attempts to model the breakage and coalescence mechanisms of the dispersed phase. This approach assumes that all droplet classes share the same

velocity field, in consequence only one momentum conservation equation is solved. This approach is called homogeneous MUSIG (Multiple Size Group)

Table 1.10 shows a summary of the modeling approach used for the dispersed phase and its relevant values for all 5 cases.

Table 1.10 Approach and values used as input for the cases modeled with a CFD model

Case	Monodispersion simulations	Polydispersed simulations
1	<ul style="list-style-type: none"> • 0.33 mm (d_{32}) • 1 mm • 2 mm 	Not performed
2	<ul style="list-style-type: none"> • 1 mm • 2 mm • 3 mm 	<ul style="list-style-type: none"> • Population balance ($d_{\min} = 0.1$ mm and $d_{\max} = 5$ mm) • 2 droplet class (multiple)
3	<ul style="list-style-type: none"> • 2.68 mm (d_{32}) 	<ul style="list-style-type: none"> • 4 droplet classes (ULLN)
4	<ul style="list-style-type: none"> • 0.64 mm (d_{32}) • 1 mm 	Not performed
5	<ul style="list-style-type: none"> • 7.70 mm (d_{32}) • 3 mm • 5 mm • 6 mm • 15 mm 	Not performed

1.5.2.2 General settings of the CFD model

The fluids were considered as Newtonian. The turbulence treatment was homogeneous using the K epsilon model. All the simulations were made under steady state conditions unless specified otherwise.

The modeled geometry consists of half a pipe with an inlet and an outlet (Fig. 1.31). The total length of the pipe changed for each case, and was approximately 45D. The boundary conditions are presented in Table 1.11.

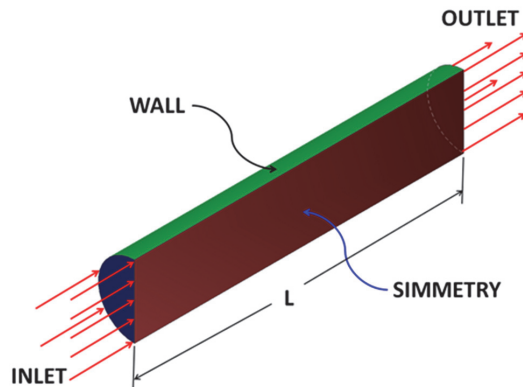


Fig. 1.31 Geometry and boundary conditions location

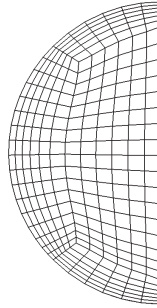
Table 1.11 Description of the boundary conditions

Location	Dispersion treatment	Boundary conditions
Inlet	Mono-dispersion	Mixture velocity and water cut
	Multi-dispersion	Mixture velocity, non-slip average volume fraction of water and droplet class
	Hom. MUSIG	Mixture velocity, size fraction of each droplet class*
Outlet	All cases	Average static pressure**
Walls	All cases	Non slip wall
Symmetry	All cases	Geometry and flow Symmetry conditions

*1 for the smallest droplet class and 0 for the rest

**for some simulations water holdup or average volume fraction of each phase were required

An extruded mesh type is used, formed by hexahedrons, with the same cross section along the pipe. The cross section of the mesh is shown in Fig. 1.32. The axial discretization used was approximately 0.1D. The total number of elements is 122850. This mesh was the result of a mesh independence study (independent results with number of elements) under multiphase flow conditions (Stanko, 2009).

**Fig. 1.32 Cross section of the mesh**

1.5.3 Comparison between the experimental data and CFD model results

The following variables were compared between the simulation results and the experimental data:

- Flow regime (arrangement of phases)
- Pressure gradient (dp/dx)
- Water holdup (H_w)
- Water volume fraction profile (α_w) along the diameter in the cross section
- Mixture velocity profile (\mathbf{V}_M) along the diameter in the cross section

The average error definition presented in Eq. 1.5 was employed in order to quantify the existing deviation between the simulated (water volume fraction or mixture velocity) profile and the experimental profile.

$$\Delta\alpha_{wavg.} = \frac{1}{M} \cdot \sum_{j=1}^M abs(\alpha_{wCFD.} - \alpha_{wEXP.}) \quad \text{Eq. 1.5}$$

Where M is the total number of experimental points available in the cross section.

All the relevant errors for each case are presented in Table 1.12. The simulations with the best agreement with experimental data are highlighted in grey in the table.

Table 1.12 differences between simulated and experimental values for all cases

Case N°	Droplet diameter	dp/dx-Diff. with exp. [%]	H _w - Diff with exp. [%]	α _w profile average diff. with exp. [-]	V _M profile average diff. with exp. [m/s]
Case 1	d = d ₃₂ (0.33 mm)	7.7	8.9	0.20	-
	d = 1 mm	7.9	8.4	0.04	-
	d = 2 mm	8.7	8.0	0.07	-
Case 2	d = 1 mm	0.2	6.6	0.09	-
	d = 2 mm	0.4	6.4	0.05	-
	d = 3 mm	1.3	6.1	0.06	-
	Population balance	1.8	6.4	0.06	-
	2 classes (tuned)	1.1	6.2	0.04	0.13
Case 3	d ₃₂ = 2.68 mm	-	0.6	0.05	-
	4 droplet classes	-	0.3	0.06	-
Case 4	d ₃₂ = 0.64 mm	-	2.0	0.04	-
	d = 1 mm	-	3.1	0.05	-
Case 5	d ₃₂ = 7.7 mm	-	31.8	0.18	-
	d = 3 mm	-	27.8	0.16	-

Mono-dispersion simulations showed a fair agreement with the experimental water volume fraction profiles when an adequate droplet diameter is used. The droplet diameter can, for some cases, be used as a tuning parameter to match to a certain tolerance the model results to the experimental data. However it was not possible to obtain a satisfactory prediction of Case 5. The results for Case 1 are presented in Fig. 1.33.

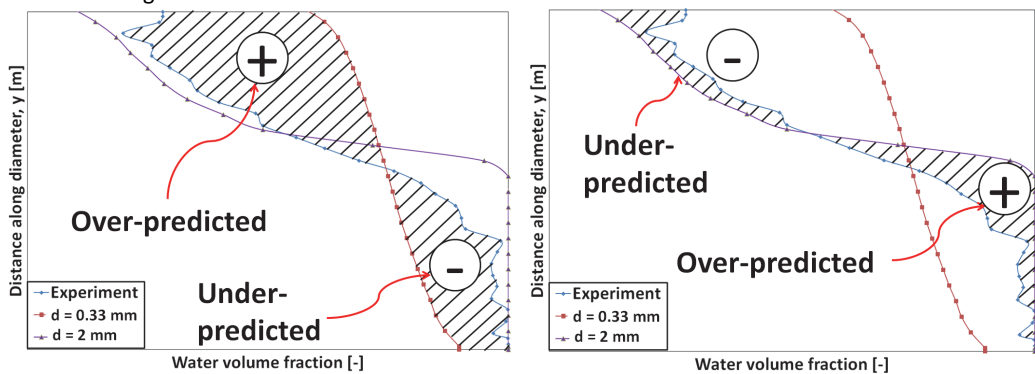


Fig. 1.33 Simulated water volume fraction profile variation with droplet diameter for case 1

The manual adjust of the parameters (droplet diameters and size fraction) of a two droplet class dispersion simulation allowed a better representation of the experimental water volume fraction profile (Fig. 1.34). However it didn't modify significantly the axial mixture velocity profile (Fig. 1.35).

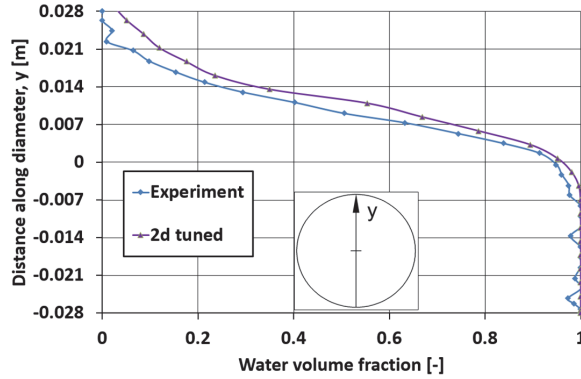


Fig. 1.34 Simulated water volume fraction profile for a tuned two diameters class dispersion for Case 2

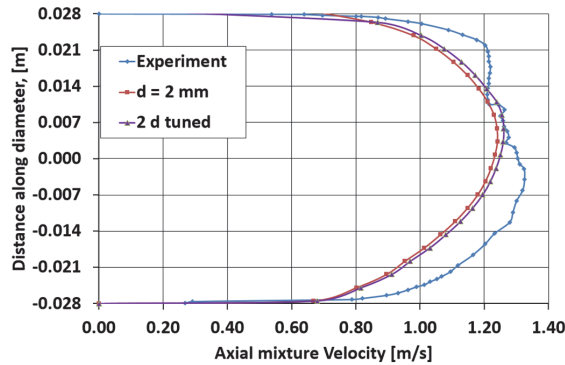


Fig. 1.35 Simulated axial mixture velocity profile for case 2

The population balance model estimates a droplet size similar in size to the average particle size observable in the tests and the results have a fair agreement with the experimental volume fraction and velocity profiles. However it did not improve the CFD model prediction significantly compared to the mono-dispersed approach.

A multi-size dispersion simulation using data from the ULLND model did not improve the CFD model prediction significantly compared to the mono-dispersed approach.

1.5.4 Concluding Remarks

- The complete simulation results can be found in Appendix E1.
- In order to be able to predict accurately the phase and velocity distribution of a dispersion of oil in water using a CFD model it is necessary either to tune it with experimental measured data along the pipe cross section or to input detailed information about the drop size distribution. Neither of those are available from the experimental prototype results of Rivera (2011).
- It was not possible to reproduce satisfactorily the experimental results of the case of low water cut and high inclination using a steady state mono-dispersed CFD model.
- The modeling strategy of using a mono-dispersion with single oil droplet diameter is selected to perform subsequent numerical simulations. This decision was based in the fair agreement exhibited with experimental data in the literature despite of the reduced input introduced to the model from real measurements.

1.6 CFD simulations to evaluate the inline separator performance

In this section a mono-dispersion CFD model of the separator prototype of Rivera (2011) is employed to: reproduce some experimental test conditions measured by Rivera, calculate the drainage potential curves for selected cases and analyze the fluid dynamic details of the separator and its performance. It is important to note that the volume fraction and velocity profiles were not measured in the experimental work of Rivera (2011).

1.6.1 Settings of the CFD simulations

The CFD multiphase model employed is very similar to the one discussed in the previous section. The initial diameter value for the dispersed phase was estimated from a tuned droplet size distribution function as explained in Appendix C1. These calculated values were compared against the average droplet diameter observed in photos taken by Rivera (2011). It was assumed that the pipe inclination angle doesn't affect the droplet size distribution.

The modeled geometry consists of half a pipe (taking advantage of the symmetry of the geometry) with an inlet and an outlet and with 5 tapping points as presented in Fig. 1.36. The details about the boundary conditions are presented in Table 1.13. The details about the geometry are presented in Fig. 1.37. The inner diameter of the main pipe is 154 mm, and the inner diameter of the tapping points is 50.8 mm.

Table 1.13 boundary conditions employed in the CFD model

Location	Boundary conditions
Inlet	Uniform mixture velocity and water cut
Outlet	Average static pressure
Walls	Non slip wall
Tapping points	Mass flow rate
Symmetry	Geometry and flow Symmetry conditions

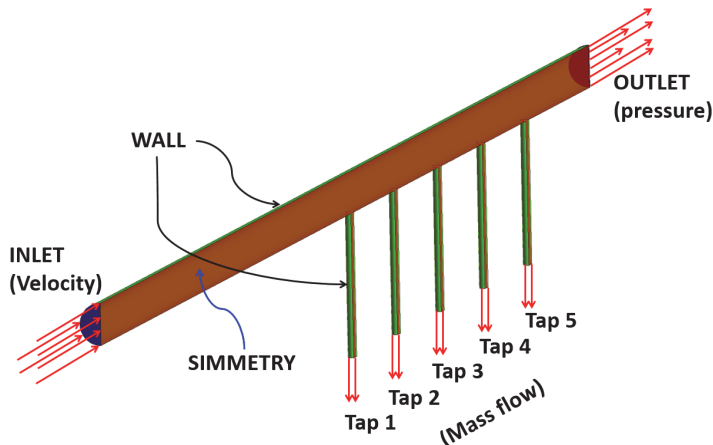


Fig. 1.36 Boundary conditions employed in the CFD model

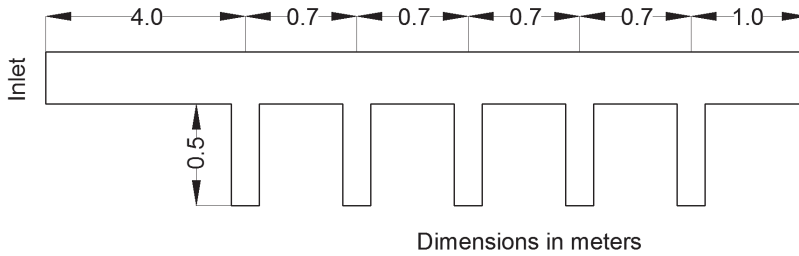


Fig. 1.37 Domain dimensions

The inlet distance before the first tapping point was chosen based on the flow development length predicted from the expression for single phase flow given in White (2008). This development length was calculated with mixture properties for all the cases simulated and the biggest value was taken (25 D). An extruded mesh type is used, formed by hexahedrons, with the same cross section along the pipe (similar to Fig. 1.32). The total number of elements is 129864. The details about the mesh, the mesh independence study, numerical uncertainty are presented in Appendix D1.

1.6.2 Simulations performed with the CFD model

A summary of the simulations performed with the CFD model are presented in Table 1.14. The oil and water mass imbalance of each simulation is also included. The cases shaded in gray color do not have experimental data available.

Table 1.14 Simulations performed with the CFD model of the separator prototype

qo [lpm]	qw [lpm]	Inclination angle [°]	Number of Tapping points	Tapped flow [lpm]	Droplet diameter [mm]	Flow regime	Oil mass imbalance [%]	Water mass imbalance [%]
27	250	15	5	5	2	Do/w & w	0.0001	0.02
		30	5	5	2	Do/w & w	0.0004	0.02
		45	5	5	2	Do/w & w	0.007	0.001
		45	5	25	2	Do/w & w	0.02	0.009
		45	2 (1 st and 5 th)	5	2	Do/w & w	3	0.08
		45	2 (1 st and 5 th)	25	2	Do/w & w	3	0.03
70	187	45	5	5	2	Do/w & w	0.002	0.02
		45	5	35	4	Do/w & w	3	1

1.6.3 General procedure for acceptance of results of the CFD model

The procedure employed to check, quality control and accept the results of the CFD model consisted on the following steps:

- Verification that the Root Mean Square (RMS) of the residuals (of the equations of momentum, mass, turbulence) of the numerical solution were below an acceptable value ($5e-5$). The RMS value contains all the residuals for all the elements in the domain.
- Verification that the mass imbalance for both oil and water was below an acceptable tolerance (<3%).
- Verify that the obtained flow regime coincides with what is expected from literature. This is done by doing a contour plot of the cross section water volume fraction and verifying the direction of the cross section phase velocity profile)
- Compare the experimental and calculated values for water holdup and pressure gradient (if available).
- Compare the experimental and calculated values for water cut of the streams drained through the tapping points (if available).

1.6.4 Results of the CFD model

1.6.4.1 Comparison between CFD model and measured data

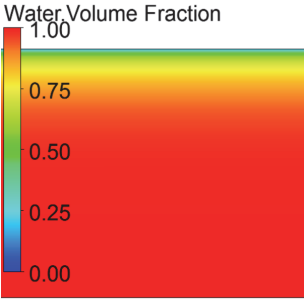
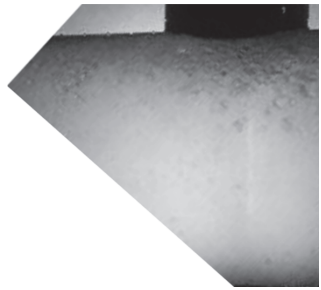
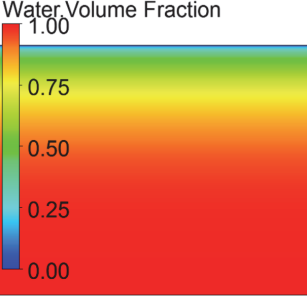

Table 1.15 presents the calculated and measured water holdup and pressure gradient for all cases (without considering the separation). The measured water holdup and pressure gradient were taken from the thesis of Ghajari (2005) who worked in the same experimental bench of Rivera. The relative differences (in percentage) between the measured and calculated values are highlighted in gray in the table.

Table 1.15 CFD model results compared with experimental results

Case		Water holdup [%]	Pressure gradient [Pa/m]
250lpmW-27lpmO (30°)	Exp.	93.26	4270
	CFD	95.71	4989.7
	Diff [%]	3	17
250lpmW-27lpmO (45°)	Exp.	95.17	6440
	CFD	95.69	7051.8
	Diff [%]	0.5	10
250lpmW-27lpmO (60°)	Exp.	92.96	7670
	CFD	95.20	8622.6
	Diff [%]	2	12
180lpmW-70lpmO (45°)	Exp.	79.88	6300
	CFD	89.61	6958.6
	Diff [%]	12	10

The calculated water volume fraction contours (lateral pipe view) are compared against experimental pictures for two cases in Table 1.16. For case **180lpmW-70lpmO (45°)** the CFD model seem to predict pretty well the thickness of the heavy packed dispersion located at the top of the pipe. However, for case **250lpmW-27lpmO (45°)** the CFD model seems to over predict the segregation at the top of the pipe.

Table 1.16 CFD water volume fraction contours compared with experimental photos

Case	CFD model contour	Experimental photo
250lpmW-27lpmO (45°)		
180lpmW-70lpmO (45°)		

In Table 1.17 the comparison is made between the drained oil cut calculated by the CFD model and measured. The relative difference (in percentage) between the measured and calculated values is highlighted in gray on the table. The CFD model consistently under predicts the amount of oil drained by the tapping points for all the cases studied.

Table 1.17 Separation results comparison between CFD model and experimental data

qo [lpm]	qw [lpm]	Inclination angle [°]	Tapped flow [lpm]		Oil cut [%]				
					Tap 1	Tap 2	Tap 3	Tap 4	Tap 5
27	250	30	5	Exp [%]	0.5	0.5	0.5	0.5	0.5
				CFD [%]	0.00	0.00	0.00	0.00	0.00
				Diff [%]	100	100	100	100	100
27	250	45	5	Exp [%]	0.5	0.5	0.5	0.5	0.5
				CFD [%]	0.00	0.00	0.00	0.00	0.00
				Diff [%]	100	100	100	100	100
27	250	45	25	Exp [%]	0.0	0.0	1.4	1.4	1.9
				CFD [%]	0.00	0.00	0.03	0.05	0.07
				Diff [%]	0	0	98	97	96
27	250	60	5	Exp [%]	0.5	0.5	0.5	0.5	0.5
				CFD [%]	0.00	0.00	0.00	0.00	0.00
				Diff [%]	100	100	100	100	100
70	187	45	35	Exp [%]	2.1	5.8	3.3	12.0	1.9
				CFD [%]	0.20	0.40	0.50	0.70	0.80
				Diff [%]	89	93	84	94	58

1.6.4.2 Case 250 lpm water 27 lpm oil: Effect of Inclination in the drainage potential curve.

The drainage potential curve was estimated for case 250lpmW-27lpmO using the numerical procedure presented in Fig. 1.14 (varying the height of the layer and perform an area integration). The water flow drained (in % of total water flow) vs the water cut of the drained stream is presented in Fig. 1.38 for 4 pipe inclinations from the horizontal. A low inclination has significantly better separation performance.

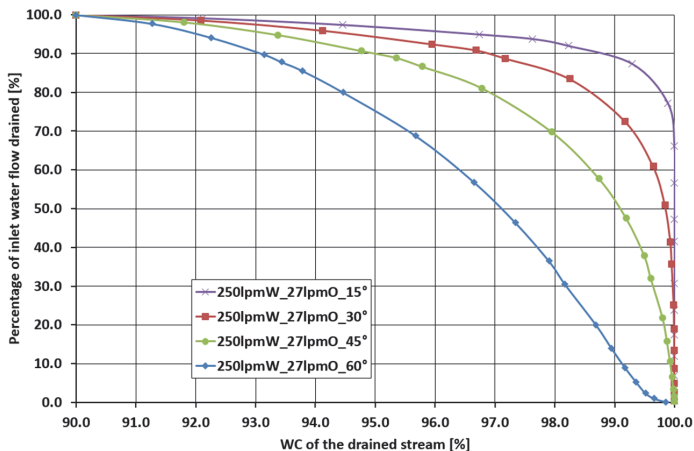


Fig. 1.38 drainage potential curve for 250 lpm water and 27 lpm oil for different inclinations

The drained layer height vs layer water flow rate (in % of total water flow) is presented in Fig. 1.39. For the same layer height, the lowest inclination transports 10% more water as compared to the highest inclination.

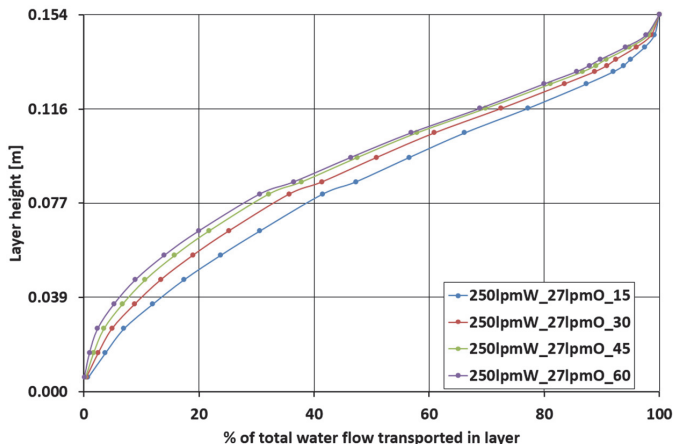


Fig. 1.39 Layer height vs water flow transported in layer

1.6.4.3 Development length

The entry development length was determined as the axial distance from the inlet (depicted as z1, z2, etc in Fig. 1.40) where there is no longer an important change in the phase volume fraction and velocity profiles along the diameter. A relative difference of 0.05% was chosen as the tolerance. The values for all the simulated cases are shown in Table 1.18. The values are roughly half the value estimated with the single phase approximation.

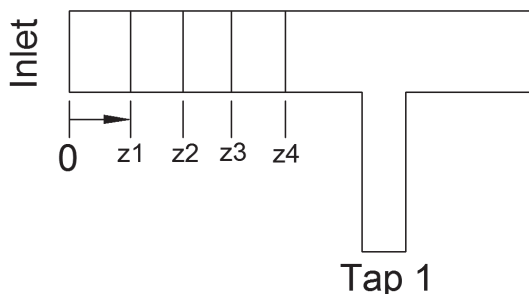


Fig. 1.40 Different axial positions measured from the inlet in the CFD model

Table 1.18 Entry development length estimated from the CFD model

qw [lpm]	qo [lpm]	Inclination angle [°]	Entry development length [m]
250	27	15	2.80
250	27	30	2.10
250	27	45	2.10
250	27	60	2.30
170	80	45	1.56

A similar procedure was repeated to check if the flow is developed in between the tapping points 1 and 2. The obtained development length values are presented in Table 1.19. It is important to note that when the tapping flow is higher the development length required is also higher. There is one condition (170lpmW-80lpmO) for which there is not enough distance between the tapping points to ensure developed flow.

Table 1.19 Development length for flow between tapping 1 and 2.

qw [lpm]	qo [lpm]	Inclination angle [°]	Tapped flow [lpm]	Development length from tapping 1 centerline [mm]
250	27	15	5	<60
250	27	30	5	<60
250	27	45	5	<60
250	27	45	25	360
250	27	60	5	160
170	80	45	35	Not developed

Conclusions and Recommendations

- A methodology for analyzing the applicability of the inline separator technology for a production system was presented and demonstrated using a typical subsea pipeline-riser-separator system. The results of the example case show the following:
 1. The required inline separator performance (water cut and its corresponding extracted flow rate) can be determined depending on the pressure reduction desired.
 2. In order to achieve a significant pressure reduction (>5%) in the system with the separator, a significant amount of fluid (~50%) has to be drained.
 3. Cases of production systems running with high viscosity oils have to be carefully analyzed. The inline separator might yield a pressure increase instead of a pressure reduction.
 4. For systems with gas content a simple liquid extraction yields a greater pressure reduction than water tapping.
 5. A control valve is necessary to adjust the flow rate drained by the separator.
- A general concept for characterizing the drainage performance of a tapping point was explained and demonstrated. The performance can either be measured from tapping experiments (preferred option), or computed through a numerical estimation from single pipe measurements (pipe profile phase volume fraction and velocity) or results of a single pipe numerical simulation. However, some limitations apply to the numerical estimation procedure from single pipe measurements.
- The drainage performance concept for a tapping point was expanded to a sequence of tapping points using the phase superficial velocity maps.
- A mono-dispersion CFD model can be used satisfactorily to reproduce experimental conditions of oil in water dispersions flowing in pipes. However, model tuning with experimental data might be required to determine the correct droplet diameter to employ.
- The CFD model of the separator prototype of Rivera (2011) under predicts the amount of oil drained by the tapping points.
- According to experimental data and CFD results, a lower pipe inclination from the horizontal yields a higher separation efficiency (less oil tapped) than a higher pipe inclination.
- Suggestions for improvement of the CFD model prediction:
 1. Customize the correlations employed for the interfacial forces. This might improve the prediction for flow regimes with lower water cut (50-70%).
 2. Use a two droplet class dispersion for modeling the separator geometry. One droplet class might be used to represent the fluid dynamics in the main pipe while the second droplet class is employed to represent the fluid dynamics of the tapping.

References

- Amundsen, L. 2011. *An experimental study of oil-water flow in horizontal and inclined pipes*. (Doctoral dissertation). Norwegian University of Science and Technology (NTNU). Trondheim. Norway.
- ANSYS (2010). *CFX-solver 13.0 modeling guide*.
- Baker, A., Nielsen, K., Gabb, A., 1988. Pressure loss, liquid holdup calculations developed. *Oil Gas. J.* (March 14), 55–59.
- Brauner, N. (2004) *Liquid-liquid two-phase flow systems. Modeling and control of two-phase flow phenomena*. Ed V Bertola. CISM Center, Italy.
- Celik, I. (2008). Procedure for estimation and reporting of uncertainty due to discretization in CFD applications. *ASME J. Fluids Eng.* 130, 078001
- Elseth, G. (2001). *An experimental study of oil/water flow in horizontal pipes*. (Doctoral dissertation). Norwegian University of Science and Technology (NTNU). Trondheim. Norway.
- Ferro, B. and M. Smith (2007). Global onshore and offshore water production. HSE Produced water. *Proceedings from Exploration and production. Oil and gas review – OTC edition*.
- Flores, J., X. Chen, C. Sarica, and J. Brill. (1998). Characterization of oil water flow patterns in vertical and deviated wells. *Proceedings from SPE Annual Technical Conference and Exhibition, San Antonio, Texas*.
- Ghajari, A. (2005). *An experimental study of Oil-water flow in upwards inclined pipes*. (Master thesis). Norwegian University of Science and Technology (NTNU). Trondheim. Norway.
- Kumara, W., B. Halvorsen, and B. Melaaen. (2009a). Pressure drop, flow pattern and local water volume fraction measurements of oil-water flow in pipes. *Meas. Sci. Technol* 20.
- Kumara W., Halvorsen B. & Melaaen M.C. (2009b). Particle image velocimetry, gamma densitometry and pressure measurements of oil–water flow. *Multiphase Science and Technology*, 21 (1–2), 51–64.
- Kumara W., Halvorsen B. & Melaaen M.C. 2010 Particle image velocimetry for characterizing the flow structure of oil-water flow in horizontal and slightly inclined pipes. *Chemical Engineering Science*, 65, 4332-4349.
- Rivera, M. R., (2005). Analysis of the performance of the patented downhole oil-water separator-DGRASS. Semester project report, NTNU. Trondheim. Norway.
- Rivera, R, Golan, M, Friedemann, J, Bourgeois, B. (2008). Water separation from wellstream in inclined separation tube with distributed tapping. *SPE Journal of Projects, Facilities & Construction. SPE article N°102722*.
- Rivera, R. (2011). *Water separation from wellstream in inclined separation tube with distributed tapping*. (Doctoral dissertation). Norwegian University of Science and Technology (NTNU). Trondheim. Norway.
- RoyMech. (2013, January 28). *Dynamic viscosities of various liquids at different temperatures* Retrieved from http://www.roymech.co.uk/Related/Fluids/Fluids_Viscosities.html.
- Schlumberger. (2011). *PIPESIM User Guide*. Pp. 506. Houston, USA. Electronic version in installation folder.
- Simmons, M. and B. Azzopardi. (2001). Drop size distributions in dispersed liquid-liquid pipe flow. *International Journal of Multiphase Flow* 27, 843–859.
- Stanko, M. (2009). *Analysis of the gravitational segregation phenomenon in water oil flows using CFD tools. [Análisis del fenómeno de separación gravitacional agua-petróleo utilizando herramientas DFC]*. (Master thesis). Simón Bolívar University (USB). Caracas, Venezuela.
- Tabeling, P. and B. Theron. (1994). *Method of analysing a two-phase flow in a hydrocarbon well*. US patent No. 5.361.206.
- Vigneaux, P., G. Catala, and J. Hulin. (1988). Oil/water flow structure measurements in inclined pipe. *SPE Annual Technical Conference and Exhibition, Houston, Texas*.
- White, F. M. (2008). *Fluid Mechanics*. 6th Edition, Mc Graw-Hill.

- Xu, J., D. Li, J. Guo, and Y. Wu. (2010). Investigations of phase inversion and frictional pressure gradients in upward and downward oil water flow in vertical pipes. *International Journal of Multiphase Flow* 36, 930–939.

Appendix A1

1D Integration method for obtaining the water and oil rates of a cross section layer

Consider that the oil and water velocities (V_w and V_o) and volume fractions (α_w and α_o) are known (either from experimental measurement or simulations) along the diameter in the cross section of the pipe as presented in Fig. A1.1:

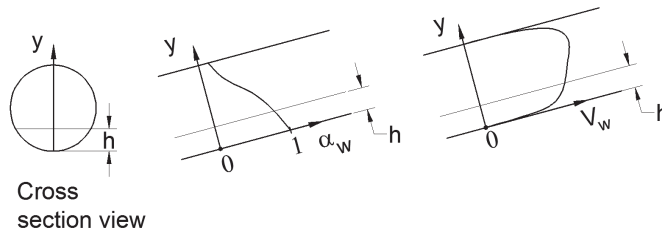


Fig. A1.1. Water velocity and volume fraction profiles along the pipe diameter

The oil and water flow rate of the layer defined by a given height “h” are estimated by Eq. A1.1 and Eq. A1.2.

$$q_w = \int_0^h \alpha_w(y) \cdot V_w(y) \cdot W(y) \cdot dy \quad \text{Eq. A1.1}$$

$$q_o = \int_0^h \alpha_o(y) \cdot V_o(y) \cdot W(y) \cdot dy \quad \text{Eq. A1.2}$$

Where $W(y)$ is the width of the pipe for a given cross section position “y” as presented in fig. A1.2, and defined by Eq. A1.3.

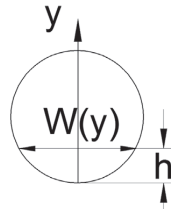


Fig. A1.2. Pipe width “W”

$$W(y) = 2 \cdot \sqrt{y \cdot (D - y)} \quad \text{Eq. A1.3}$$

These integrals were evaluated using the trapezoidal rule.

This procedure assumes that the velocity and volume fraction measured along the diameter are representative of the mean velocity and volume fraction of a given cross section position “y”.

Appendix B1

Deduction of the inclination angle of the line representing all possible conditions downstream a tapping point

As discussed earlier, if the flow rate to drain (q_t) is fixed all the possible conditions downstream the tapping point (depending on the tapping point efficiency) fall in the line presented in Fig. B1.1 in the phase superficial velocity map.

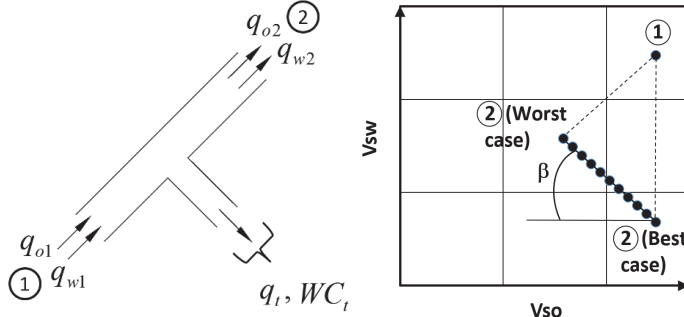


Fig. B1.1. Representation of all possible separation efficiencies in a superficial velocity plot

The oil and water superficial velocities of any possible condition downstream the tapping point (depending on the separator efficiency) can be expressed using the generic expressions Eq. B1.1 and Eq. B1.2:

$$V_{so2} = V_{so1} - V_{st} \cdot (1 - WC_t) \tag{Eq. B1.1}$$

$$V_{sw2} = V_{sw1} - V_{st} \cdot (WC_t) \tag{Eq. B1.2}$$

Where V_{st} is the tapped liquid flow rate divided by the cross section area of the main pipe (q_t/A). Please note that in this deduction the water cut (WC) is expressed in fraction.

Eq. B1.1 and Eq. B1.2 were particularized for the best case and for the worst case. The resulting expressions are presented in Table B1.1.

Table B1.1. Best case and worst case oil and water superficial velocities

	Oil	Water
Best case	$V_{so2}^b = V_{so1}$	$V_{sw2}^b = V_{sw1} - V_{st}$
Worst case	$V_{so2}^w = V_{so1} - V_{st} \cdot \left(\frac{V_{so1}}{V_{so1} + V_{sw1}} \right)$	$V_{sw2}^w = V_{sw1} - V_{st} \cdot \left(\frac{V_{sw1}}{V_{so1} + V_{sw1}} \right)$

The angle between the line representing all possible conditions downstream a tapping point and the horizontal (β) is estimated with Eq. B1.3.

$$\tan(\beta) = \frac{(V_{sw2}^w - V_{sw2}^b)}{(V_{so2}^b - V_{so2}^w)} \tag{Eq. B1.3}$$

Substituting the expressions from table B1.1. in Eq. B1.3 yields:

$$\tan(\beta) = \frac{V_{sw1} - V_{st} \cdot \left(\frac{V_{sw1}}{V_{so1} + V_{sw1}} \right) - V_{sw1} + V_{st}}{V_{so1} - V_{so1} + V_{st} \cdot \left(\frac{V_{so1}}{V_{so1} + V_{sw1}} \right)} \tag{Eq. B1.4}$$

Simplifying terms in Eq. B1.4 yields Eq. B1.5:

$$\tan(\beta) = 1 \tag{Eq. B1.5}$$

Leading to the conclusion that $\beta = 45^\circ$.

Appendix C1

Droplet size prediction of an oil in water dispersion

The multiphase models employed in the present study sometimes require as an input representative diameters of the dispersed phase in order to perform the calculations. One of the methods employed in the present study for predicting the relevant droplet sizes in an oil in water dispersion is the cumulative droplet size distribution function. This is a standard way of treating dispersion size information.

This function (as used in the present study) gives back for a given droplet diameter “d” the ratio between oil volume contained in droplets of diameter “d” or smaller divided by the total volume of oil. The particular statistical function used is the Upper-Limit log-normal function (ULLN) as presented in Eq. C1.1.

$$CV(d) = \frac{1}{\sqrt{\pi}} \cdot \int_{\delta \cdot z}^{\infty} \exp(-x^2) \cdot dx \quad \text{Eq. C1.1}$$

Where:

$$z = \ln\left(\frac{a \cdot d}{d_{\max} - d}\right) \quad \text{Eq. C1.2}$$

The values of δ , a and d_{\max} (maximum droplet diameter in the dispersion) are characteristic for a given oil in water dispersion and are an input to the function. The standard procedure is to measure experimentally the characteristics of a given dispersion and then calculate the best set of values δ , a that provide an appropriate match (d_{\max} is usually observable from experimental photos).

When only one droplet size is to be employed, the representative droplet diameter value taken is the Sauter mean diameter as defined by Eq. C1.3.

$$d_{32} = \frac{d_{\max}}{1 + a \cdot \exp\left(\frac{1}{4 \cdot \delta^2}\right)} \quad \text{Eq. C1.3}$$

If “N” droplets classes are to be used, the procedure followed is presented next:

1. The diameter of each droplet class “i” is calculated as

$$d_i = \left(i - \frac{1}{2}\right) \cdot \left(\frac{d_{\max}}{N}\right) \quad \text{Eq. C1.4}$$

2. The size fraction of each droplet class (Volume of oil contained in droplets of a given diameter “d” divided by total volume of oil) is calculated as:

$$f_i = CV\left(i \cdot \left(\frac{d_{\max}}{N}\right)\right) - CV\left((i-1) \cdot \left(\frac{d_{\max}}{N}\right)\right) \quad \text{Eq. C1.5}$$

Determination of ULLN parameters: δ , a and d_{\max}

In the present study it will be considered that δ and a are fixed for given oil and water fluid properties, while d_{\max} depends on the flow conditions. The values were obtained from the following sources:

- Literature data (applicable for any oil in water dispersion except the data of Rivera (2011))
- Rough tuning with oil in water dispersion pictures (applicable only for the oil in water dispersions of Rivera (2011)). It is important to note that this tuned model should be used with caution as usually much more data than the one employed in this work should be used to generate and corroborate an ULLN function. Unfortunately, the experimental data of Rivera (2011) provided limited information about dispersion size.

The details of these two approaches are discussed next.

Literature data

The values of δ , a were taken from the work of Simmons & Azzopardi (2001) (1.35 and 0.61 respectively). The maximum diameter exhibited for the dispersion (d_{\max}) was taken as the maximum between the model of Hinze (Brauner 2004) for dilute dispersions (Eq. C1.6) and Brauner (2004) for dense dispersions (Eq. C1.7). The variables are introduced in the equation in coherent metric units.

$$\left[\frac{d_{\max}}{D} \right]_{\text{diluted}} = 0.55 \cdot We_w^{-0.6} \cdot f_{ip}^{-0.4} \quad \text{Eq. C1.6}$$

$$\left[\frac{d_{\max}}{D} \right]_{\text{dense}} = 2.22 \cdot We_w^{-0.6} \cdot \left[\frac{\rho_M}{\rho_w \cdot (WC)} \cdot f_{ip} \right]^{-0.4} \cdot \left[\frac{(1-WC)}{(WC)} \right]^{0.6} \quad \text{Eq. C1.7}$$

Where f_{ip} is the two-phase friction factor, We_w is the water Weber number (Eq. C1.8), V_M is the mixture velocity and WC is the water cut (in fraction), ρ_M is the mixture density, ρ_w is the water density and D is the internal pipe diameter.

$$We_w = \frac{\rho_w \cdot V_M^2 \cdot D}{\sigma_{ow}} \quad \text{Eq. C1.8}$$

In the Weber number equation σ_{ow} is the interfacial tension between oil and water.

The two phase friction factor was estimated by using a single phase friction factor correlation as suggested by Flores et al. (1998) (Eq. C1.9).

$$f_{ip} = C_f \cdot Re_M^{-n_f} \quad \text{Eq. C1.9}$$

Where:

The values of C_f and n_f were taken from the work of Xu et al. (2010) and are 9.078E7 and 1.822 respectively

The mixture Reynolds number is defined as:

$$Re_M = \frac{\rho_M \cdot V_M \cdot D}{\mu_w} \quad \text{Eq. C1.10}$$

Where μ_w is the water viscosity.

Rough tuning with oil in water dispersion data from Rivera (2011)

A moderate quality photo (Fig. C1.1) available from the work of Rivera (2011) was analyzed manually. The photo corresponds to an inclination of 45° (Oil rate 70 lpm and water rate 180 lpm).

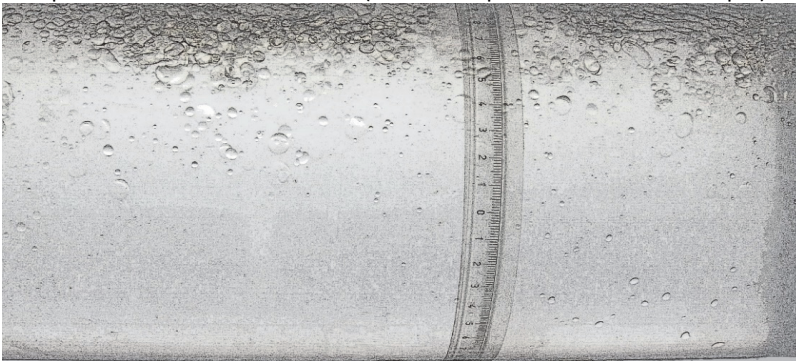


Fig. C1.1. Photo available from the experimental work of Rivera (2011) (preprocessed).

The procedure consisted in detecting particles with the same size (i.e. diameter) and counting them. The resulting data is presented in Table C1.1. It is important to note that there are a group of droplets of

sizes between 6.0 and 8.0 mm that were not accounted for properly because they are existing in a heavy packed area thus their interfaces were not clear.

Table. C1.1. Resulting droplet count table.

Drop diameter [mm]	Number of droplets [-]
0.8	131
1.7	73
2.0	46
2.5	59
3.8	40
4.5	19
6.0	23
8.5	13
9.0	2
10.0	1

These values were used in a tuning process of the parameters of the ULLN function (using MS Excel solver). The resulting tuned values are presented in Table C1.2.

Table. C1.2. Tuned parameters of the ULLN function.

δ	0.6724
a	0.6509

Tuning the d_{\max} equation of Brauner (Eq. C1.7)

In the d_{\max} equation of Brauner (Eq. C1.7), a tunable multiplying constant C_H might be included in order to improve its predictability. This parameter was included in the equation and tuned to reproduce the d_{\max} observed in two photos available from the work of Rivera (2011). The tuned value was $C_H = 1.4273$.

Appendix D1 Details of the CFD model of the separator prototype (mesh analysis)

A mesh independence study under two phase flow conditions was performed for the separator prototype geometry described in Fig. 1.36. This study determines an adequate mesh sizing (minimum number of nodes or elements) that ensures that the results of the CFD model are not mesh dependent. This is done by comparing the results of different mesh sizes against a very dense mesh. If the differences are below a certain pre chosen tolerance, it can be considered that the model is mesh independent. For the present study it was considered that the results are mesh independent when the relative difference with the densest mesh is less than 1%.

The study was based on the results of Stanko, (2009). Five meshes of the geometry were generated of 67k, 115k, 145k, 268k, 610k nodes. CFD simulations were then made using as boundary conditions: inlet flow rates of 250 lpm of water and 27 lpm of oil, tapping flow rate of 5 lpm and outlet static pressure. The results of the simulations had similar RMS residuals and mass imbalances.

The following variables were extracted from the results

- Oil and water velocity and volume fraction profiles along the diameter for 11 axial positions in the main pipe
- Pressure, Mass rates of oil and water drained for each tapping point
- Average water volume fraction and pressure in cross section planes for 13 axial positions in the main pipe.

The relative differences between the variable's values for each mesh compared to the densest mesh were computed. The results of the mesh with 145k nodes (129864 elements) displayed an average difference with the densest mesh lower than 1% therefore it was selected as the final working mesh for the CFD model. Some images of the mesh are shown in Fig. D1.1. The number of elements in the axial direction for each section are described in detail in Fig. D1.2.

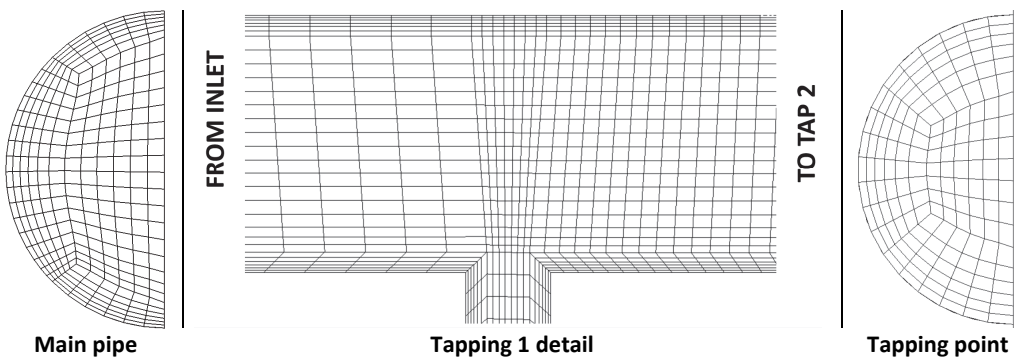


Fig. D1.1 Details of the mesh employed in the present study.

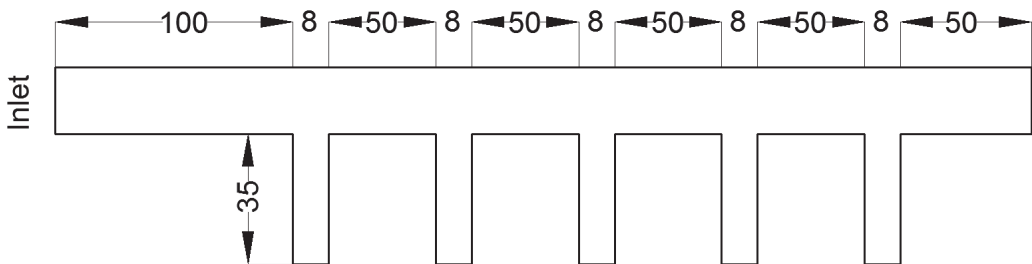


Fig. D1.2 Details of the mesh employed in the present study.

Estimating the discretization uncertainty of the CFD model

The discretization uncertainty of the CFD model was estimated according to the procedure presented by Celik (2008). As an example some uncertainties for representative variables are shown in table D1.1.

Table D1.1. Representative uncertainties for some variables calculated with the CFD model

	Discretization uncertainty [%]
Average pressure in plane	1e-6
Average water volume fraction in plane	0.04
Water volume fraction profile	3
Water Velocity profile	0.6

For some cases the calculated uncertainty is very small when compared with the mass imbalance in the domain. In those cases the mass imbalance was used to define the error rather than the uncertainty value.

Appendix E1 Paper

3D-CFD numerical simulation of gravity induced segregation in water dominated dispersed oil-water pipe flow

Presented and published in the 8th International Conference on Multiphase Flow (ICMF) 2013, Jeju, Korea, May 26-31

3D-CFD numerical simulation of gravity induced segregation in water dominated dispersed oil-water pipe flow

Milan Stanko¹, Miguel Asuaje², Michael Golan¹

¹*Department of Petroleum Engineering and Applied Geophysics, Norwegian University of Science & Technology, Trondheim, Norway*

²*Department of Energy Conversion and Transport, Universidad Simón Bolívar, Caracas, Venezuela*

Keywords: multiphase cfd model, oil water segregation,

Abstract

This paper evaluates CFD (computational fluid dynamics) models to predict phase segregation in dispersed oil in water flows. This evaluation has been conducted in an attempt to use CFD models to improve the design methodology of an inline separator of oil-water flow for subsea petroleum production systems.

Five reported cases simulating water dominated dispersed oil-water flow in horizontal and upward inclined pipes are reported in this paper. The simulations in all the cases are made using Euler-Euler, 3D, CFD techniques considering the oil as a dispersed phase and the water as the continuous phase. The commercial software Ansys CFX is used in the simulation. The forces in the conservation equations considered in the analysis are: drag, lift, buoyancy, turbulent dispersion and lubrication. Three different approaches are used to represent the dispersed phase: mono-size droplet dispersion, multi-size droplet dispersion and population balance using the MUSIG (Multiple Size Group) model. An upper-limit log-normal (ULLN) droplet distribution is used as an input for some of the mono-dispersion and multi-size dispersion simulations.

The simulation results are compared against public domain reported experimental data. This data include water volume fraction and velocity profiles and high speed images. The validation is focused on comparing the water volume fraction profile and using the images for quality control of the droplet size.

Mono-dispersion simulations of high water cut cases showed a fair agreement with the available experimental data when an adequate droplet diameter is used. The droplet diameter in the mono dispersed simulation can be used as a tuning parameter to match, to a certain tolerance, the model results to the experimental data. This when the droplet size is selected within the physical range of the problem.

For high velocity in a small pipe diameter cases the maximum droplet size predicted by the ULLN distribution is considerably smaller than the average droplet size observed in the available images. The MUSIG model estimates a droplet size similar in size to the average particle size observed in the available images. The results agree with the reported volume fraction and velocity profiles. A multi-size dispersion simulation using the MUSIG model or input data from the ULLN model did not improve significantly the prediction of the CFD model compared to the mono-dispersed approach. A better agreement with the experimental water volume fraction profile reported has been obtained by manual tuning of the parameters of a two droplet class dispersion.

In conclusion, this paper identifies relevant limitations and constraints for each one of the addressed CFD methods to predict successfully a dispersion of oil in water flow.

Introduction

Inline separation of oil and water is based on draining progressively the water enriched phase accumulated at the bottom of an inclined pipe through distributed tapping points (Fig. 1.). This separation technology is of high interest for mature oil fields producing with high water cuts specifically for downhole or seabed applications where a decrease in the transport pressure drop yields an increase in production (Rivera, 2008).

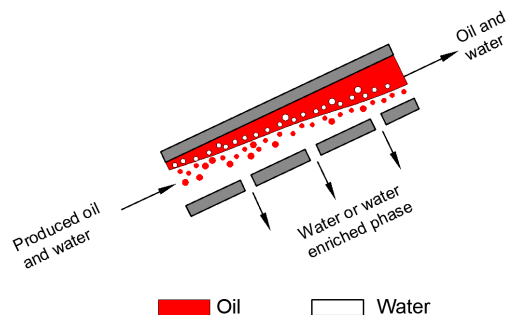


Fig. 1. Functioning principle of the inline separation of oil and water

Experimental observations (Rivera, 2008) have demonstrated that many flow patterns in inclined upwards oil-water flow exhibit such a water enriched layer suitable for drainage. The knowledge of the dynamics and dimensions of that layer is critical for design, prediction and evaluation purposes of the inline separation technology. A CFD numerical model is proposed to predict the multiphase flow dynamics existing in dispersed oil in water flow. It would provide the level of detail required for separator design and enough flexibility to represent the broad range of fluid properties and operational conditions of oil-water flow in the petroleum production systems.

This paper reports some observations, conclusions and recommendations about the prediction of the dynamics and phase distribution of dispersed oil in water flows using computational fluid dynamics (CFD). The configuration of interest is inclined pipes. As the main field of applications is for high water cut oil fields, the work is limited to water dominated flow patterns.

Nomenclature

CFD	Computational fluid dynamics
D	pipe diameter, (m)
d	droplet diameter (m)
x	auxiliary integration variable
y	distance along diameter (m) departing from center of pipe
g	gravitational constant (ms^{-1})
P	pressure (Nm^{-2})
L	Pipe axial length
V	velocity (m s^{-1})
∇	Volume
WC	water cut
V_{xs}	Superficial velocity of phase “x” (m/s)
d_{32}	Sauter mean diameter
H_w	water holdup
E_o	Eötvös number (-)
N	Total number of classes existing in the dispersed phase
M	Total number of experimental points available

Greek letters

ρ	density (kg m^{-3})
α	volume fraction (-)
σ	oil-water interfacial tension (N m^{-1})
θ	pipe inclination from horizontal [$^\circ$]
μ	viscosity (Pas)

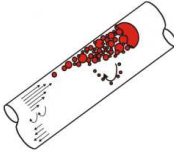
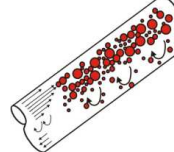
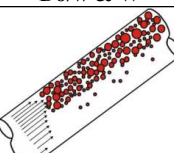
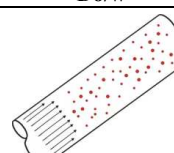
Subscripts

w	water
o	oil
M	mixture
i	dispersed class “i”
MAX	Maximum
avg.	average

Dispersed oil-water flow in inclined pipes

Table 1 presents the water dominated oil-water flow patterns in upwards inclined pipes according to the nomenclature presented by Brauner (2004).

Table 1. Water dominated flow regimes in upwards inclined oil-water flows

Intermittent dispersion of oil in water and water	Dispersion of oil in water and water with backflow
I Do/w & W	Do/w & W BF
	
Dispersion of oil in water and water	Dispersion of oil in water and water
Do/w & W	Do/w
	

The majority of these flow patterns exhibit phase segregation caused by the density difference, with the water accumulated at the bottom of the pipe and the oil dispersion close to the top of the pipe.

Due to this phase segregation, the mixture velocity is high at the top of the pipe and low at the pipe bottom. Depending of the flow rate, the water rich layer at the bottom of the pipe will circulate downwards or upwards.

A detailed description of experimental data available in the public literature for oil water flow in inclined pipes is presented in Brauner (2004).

Dispersed oil-water flow modeling using CFD tools

Computational Fluid Dynamics, (CFD), is the utilization of computational methods to solve fluid flow problems and its interaction with contours. This is done by solving the differential conservation equations together with correlations or particular models that represent the physical phenomena using numerical methods.

The most common method used for solving these equations is the Finite Volume Method. Summarizing, it consist on subdividing the domain of interest in small subdomains or “volumes” and to integrate the equations on each one of them. The result is a set of algebraic equations that are solved using numerical methods.

There are many variations of CFD methods for multiphase flow in the literature. The section below explains briefly the fundamentals of the CFD method employed in the present work.

Water is assumed as the continuous phase and the oil is considered the dispersed phase. The oil is arranged in N droplets sizes (classes), each one with a different characteristic diameter d_i (See fig. 2, $N = 3$). A

mono-dispersion displays only one characteristic droplet diameter. A multi-size dispersion displays several (N) droplet diameters.

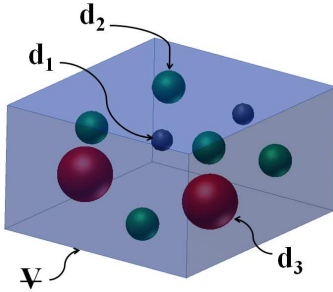


Fig. 2. 3 droplet class dispersion of oil in water

The volume fraction of each droplet class is defined as:

$$\alpha_{di} = \frac{V_{odi}}{V} \quad (1)$$

Where:

V_{odi} ...volume of oil allocated in droplets of diameter “i.” inside the volume V .

The size fraction of the droplet class is given by:

$$f_i = \frac{V_{odi}}{V_o} = \frac{\alpha_{di}}{\alpha_o} \quad (2)$$

Where:

V_o ...Total oil volume inside volume V .

Note the following relationship:

$$\alpha_o = \sum_{i=1}^N \alpha_{di} \quad (3)$$

Separated conservation equation of mass and momentum are solved for the continuous phase and dispersed class(es) using the Euler-Euler formulation (Ansys 2010). The equations include the interfacial interaction terms and they are estimated from correlations and models existing in the literature.

The CFD method does not compute the interphase between the continuous and dispersed classes, rather assumes that the dispersed class is distributed in droplets of diameter d_i . It also assumes that there is no interaction (mass or dynamic wise) between the droplet classes in the dispersed phase.

Population balance can also be incorporated in the CFD analysis. In the present study it is only used for referential purposes and the details will be discussed later.

The homogeneous MUSIG (Multiple Size Group) model assumes that all the classes in the dispersed phase travel at the same speed. The mass conservation equations of the dispersed phase are modified to take into account breakage and coalescence between classes. The droplet size distribution is a result of the simulation.

Selected experimental works

In order to validate the CFD model, the experimental data has to provide detailed information on phase and mixture velocity distribution in the pipe. In the public literature there are few works about oil-water flow in inclined pipes that report data with the required level of detail. The authors selected relevant cases from the works of Vigneaux et al.

(1988a), Tabeling et al. (1994) and Kumara et al. (2009a, 2009b). The selected experimental cases used in the present study are shown in table 2. The cases are organized by inclination angle.

Table 2. Experimental cases simulated in the present study

Nº	Flow pattern	Source	V_M [m/s]	WC [-]	θ [°]	D [m]
1	Do/w&w	Kumara et al. (2009a)	1.50	0.75	0	0.056
2	Do/w&w/o	Kumara et al. (2009b)	1.06	0.75	0	0.056
3	IDO/w&w	Tabeling et al. (1994)	0.12	0.90	25	0.200
4	Do/w&w	Vigneaux et al. (1988)	0.47	0.90	25	0.100
5	Do/w&w BF	Tabeling et al. (1994)	0.12	0.50	65	0.200

The cases taken from the work of Kumara (2009a, 2009 b) are for horizontal flow. They were included in the present study because their flow patterns are also present in inclined pipes and because of the level of detail of the experimental information.

The relevant properties of the fluids used in the experimental cases are presented in table 3.

Table 3. Physical properties of the experimental fluids for each case

	Oil	ρ_w [kg/m ³]	ρ_o [kg/m ³]	μ_w [mPa s]	μ_o [mPa s]	σ [mN/m]
1&2	Exxol D60	996	790	1.00	1.64	43.0
3&5	Kerosene	996	779	1.00	5.00	47.0
4	Kerosene	996	740	1.00	2.05	47.0

Table 4 presents a summary of the relevant experimental data gathered in each one of the cases. The validation was focused primarily in reproducing the experimental phase distribution profile in the pipe and the water holdup.

Table 4. Experimental information available for each case

Nº	α_w profile	V_M profile	H_w [-]	Image	Δp [Pa m ⁻¹]
1	A	NA	0.69	A	431.0
2	A	A	0.70	A	213.6
3	A	NA	0.97	NA	NA
4	A	NA	0.94	NA	NA
5	A	NA	0.67	NA	NA

*A = available, NA = Non Available

Multiphase CFD model details

Ansys CFX® (V-13) commercial software was used for the modeling.

General settings of the CFD model

The fluids were considered as Newtonian. The turbulence treatment was homogeneous using the K epsilon model. All the simulations were made under steady state conditions unless specified otherwise.

Geometry and boundary conditions

The geometry consists in half pipe with an inlet and an outlet (fig. 3.). The total length of the pipe changed for each case, and was approximately 45D. The boundary conditions are presented in Table 5.

Table 5. Boundary conditions of the CFD model

Location	Dispersion treatment	Boundary conditions
Inlet	Mono-dispersion	Mixture velocity and water cut
	Multi-dispersion	Mixture velocity, non-slip average volume fraction of water and droplet class
	Hom. MUSIG	Mixture velocity, size fraction of each droplet class*
Outlet	All cases	Average static pressure**
Walls	All cases	Non slip wall
Symmetry	All cases	Geometry and flow Symmetry conditions

*1 for the smallest droplet class and 0 for the rest

**for some simulations water holdup or average volume fraction of each phase were required

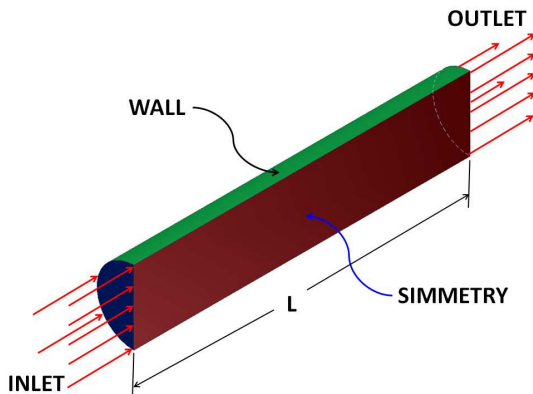


Fig. 3. Geometry and boundary conditions

An extruded mesh type is used, formed by hexahedrons, with the same cross section along the pipe. The cross section of the mesh is shown in Fig. 4. The axial discretization used was approximately 0.1D. The total number of elements is 122850. This mesh was the result of a mesh validation process in multiphase flow conditions (Stanko, 2009).

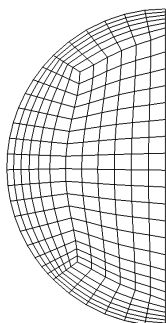


Fig. 4. Cross section of the mesh

The following forces are considered:

-Drag force: The total drag force is calculated by the drag coefficient given by the correlation of Ishii-Zuber (Ansys, 2010). This correlation considers the drag coefficient independent of the Reynolds number but dependent on the droplet Eötvös number. It is suitable for dense and sparsely distributed droplets.

-Lift force: The total lift force is calculated by the lift coefficient using the Tomiyama correlation (Ansys, 2010). It considers that the lift coefficient depends only on the droplet Eötvös number.

-Lubrication force: The lubrication force is estimated using the Frank model (Ansys, 2010). The wall lubrication coefficient depends only on the droplet Eötvös number.

-Turbulent dispersion force: The turbulent dispersion force is estimated using the Favre averaged drag model (Ansys, 2010).

Specific settings of the MUSIG model

Table 6 shows some of the settings used for the Hom. MUSIG model.

Table 6. Settings used for the Hom. MUSIG model

Coalescence model	Prince and Blanch
Breakage model	Luo and Svendsen
Diameter discretization	Equal diameter
Number of sizes	5
d_{min} [m]	0.1e-4
d_{max} [m]	Max(d _{max} Brauner, d _{max} hinze)*

*Or d_{max} experimental, if available.

Results and discussion

1. Droplet size prediction with the ULLN model

The droplet distribution characteristics of the flow regimes under study are predicted using an Upper-limit log-normal distribution (ULLN). The details of the model are presented in Appendix I. Table 7 presents the maximum diameter and the Sauter mean diameter calculated for the cases.

Table 7. Maximum droplet diameter and Sauter mean diameter predicted by the ULLN model

Nº	V _M [m/s]	WC [-]	d _{MAX} * 1e-3 [m]	d ₃₂ * 1e-3 [m]
1	1.50	0.75	1.19	0.33
2	1.06	0.75	1.40	0.39
3	0.12	0.90	9.77	2.68
4	0.47	0.90	2.35	0.64
5	0.12	0.5	27.98	7.68

For cases 1 and 2 the maximum diameter predicted (0.3 mm) is considerably less than the average droplet diameter exhibited in the experimental photos (~3 mm, Fig. 4. of

Kumara et al. 2009b).

For cases 3, 4 and 5 there were no photos available, so no comparison is made.

The CFD mono-dispersed simulations are performed using as a starting point the Sauter mean diameter and then increasing or decreasing the droplet diameter depending on the prediction.

2. Water volumetric fraction profile, water holdup and pressure drop prediction

2.1. Mono-dispersion simulations

Case 1: $\theta = 0^\circ$, Do/w&W

Fig. 5 shows the calculated water volume fraction profile for Case 1 using: the Sauter mean diameter, 1 mm droplet diameter and 2 mm droplet diameter; compared against the experimental profile reported.

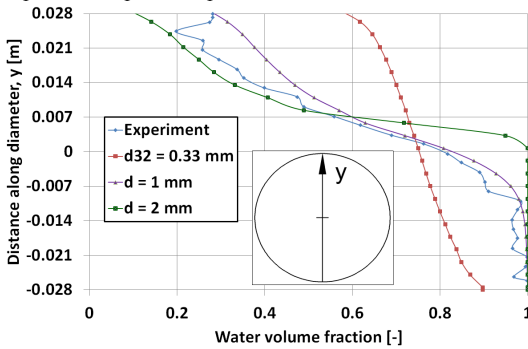


Fig. 5. Computed water volume fraction profile for Case 1 using a mono-dispersion

The simulation performed with the Sauter mean diameter is under-predicting the oil segregation in the pipe. In Fig. 6 two areas are highlighted: one in the upper part of the pipe, where the water volume fraction is over-predicted and one in the lower part of the pipe, where the water volume fraction is under-predicted.

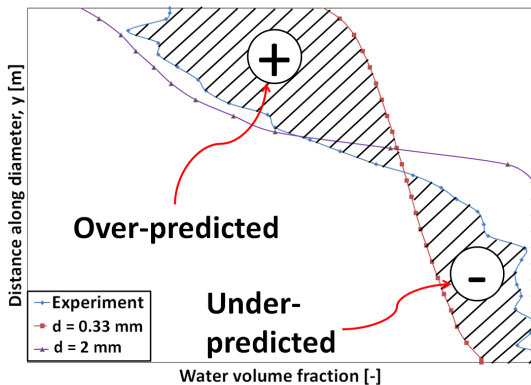


Fig. 6. Water volume fraction predicted by a small droplet diameter for case 1.

When the diameter is increased (Fig. 7) the CFD simulation over-predicts the oil segregation.

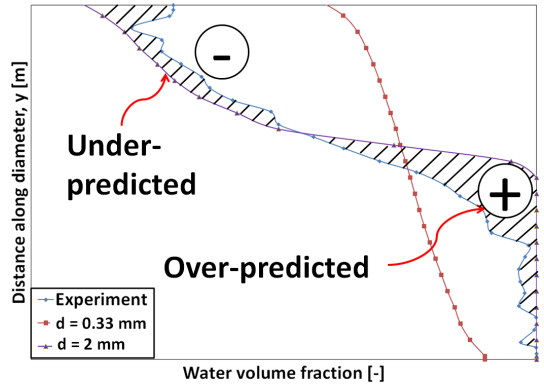


Fig. 7. Water volume fraction predicted by a big droplet diameter for case 1.

In order to quantify the existing deviation between the simulated profile and the experimental profile, the following definition is introduced (eq. 4):

$$\Delta\alpha_{wavg.} = \frac{1}{M} \cdot \sum_{j=1}^N abs(\alpha_{wCFD.} - \alpha_{wEXP.}) \quad (4)$$

Where M is the total number of experimental points available.

Table 8 presents the average deviation of the simulated results against the experimental data. The simulation performed with a droplet diameter of 1 mm gives a better match with the experimental profile.

Table 8. Comparison of the mono-dispersed results against the experimental data for Case 1

Droplet diameter	$\Delta\alpha$ - Diff. with exp. [%]	H_w Diff with exp. **[%]	α_w profile average diff. with exp. [-]
d = d_{32} (0.33 mm)	7.7	8.9	0.20
d = 1 mm	7.9	8.4	0.04
d = 2 mm	8.7	8.0	0.07

*CFD value measured between planes located at 30D and 33D from the inlet

**CFD value measured at 35D from the inlet

Cases 2, 3, 4 and 5:

The comparison between the calculated and the experimental values for cases 2, 3, 4, and 5 are presented in Appendix II.

For case 2, the simulation with the Sauter mean diameter under-predicts the segregation in the pipe and it is not shown. A droplet diameter of 1 mm predicts well the water volume fraction in the lower part of the pipe, but under-predicts the oil content in the upper part of the pipe.

Increasing the droplet diameter improves the prediction in

the upper part of the pipe, but it affects the prediction in the lower part of the pipe. The simulation performed with a droplet diameter of 2 mm gives the best match with the experimental profile.

For cases 3 and 4, the Sauter mean diameter provided a fair agreement with the experimental data.

In case 3 this flow pattern is intermittent, with oil droplets conglomerates moving in the upper part of the pipe. A transient simulation was performed to verify that the steady state results are a good representation of the transient phenomena on the pipe.

The boundary conditions were the same that for the steady state simulation. The transient simulation departed from the steady state solution. The time step chosen for the simulation was 0.01 s, and the simulation was performed for a total time of 120 s.

The calculated water volume fraction and mixture velocity profile changed slightly with time. However, the variation was less than 1%.

For case 5 droplet diameters in the range between 3 mm to 10 mm were tested out but none of them gave an acceptable representation of the experimental volume fraction profile.

2.2. Multi-size dispersion simulations

Simulation with the homogeneous MUSIG Model

Case 2: $\theta = 0^\circ$, Do/w&o

A simulation was performed with the homogeneous MUSIG model. The maximum diameter was set as 5 mm (as observed in the experimental pictures).

Fig. 8 below shows the predicted mean particle diameter. There are two predominant droplet diameters in the pipe: one small diameter (0.6 mm) in the lower part of the pipe, and a big droplet diameter (4.5 mm) in the upper part of the pipe. The other 3 diameters are present in a very fine layer between these two.

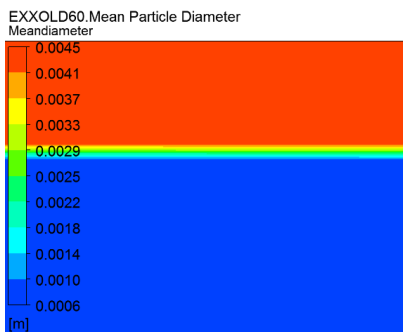


Fig 8. Mean particle diameter predicted by the hom MUSIG model

The droplet diameter distribution predicted by the homogeneous MUSIG model in the pipe cross section is presented in table 9. As observed in the previous figure, the oil phase is distributed predominantly in the smallest and the biggest droplet size.

Table 9. predicted droplet size distribution by the hom. MUSIG model.

d	Size fraction
[m]	[-]
0.0006	0.54
0.0016	0.10
0.0026	0.02
0.0035	0.01
0.0045	0.33

Fig. 9 shows the predicted water volume fraction profile compared with the experimental and the calculated with a monodispersion ($d = 2$ mm). The hom. MUSIG model improves the prediction in the upper part of the pipe but it deteriorates the prediction in the lower part of the pipe. The average difference with the reported profile is 0.06, with the reported water holdup is 6.4 % and with the pressure drop 1.8%.

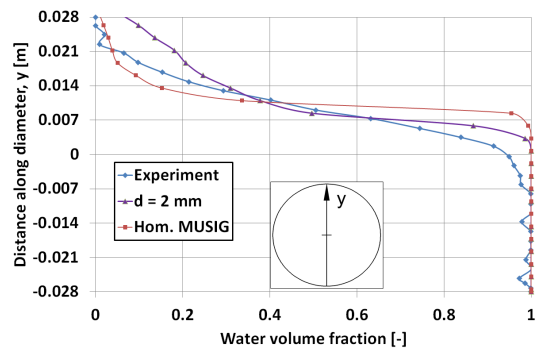


Fig. 9. water volume fraction profile predicted with the hom. MUSIG model for case 2.

Two droplet classes dispersion

Five simulations were performed using a two droplet class dispersion. The main objective was to change the two droplet diameters and the inlet size fraction until a fair agreement with the experimental data was reached. This process was performed manually.

The droplet diameters (d_1 and d_2) were changed within the range observable in the experimental picture. Generally speaking, simulations results were more sensitive to changes in the droplet size than to the inlet size fraction. The best agreement after 5 simulations was obtained for the values shown in table 10.

Table 10. Simulation parameters

	Dispersed phase 1	Dispersed phase 2
d [m]	1e-3	4e-3
Inlet size fraction [%]	50	50

Fig. 10 shows the calculated water volume fraction profile compared with the experimental. The agreement is better (average difference of 0.04 with the reported water volume

fraction profile, 1.1% difference with the reported pressure drop, and 6.2% difference with the reported water holdup) when compared against the mono-dispersion and hom. MUSIG cases.

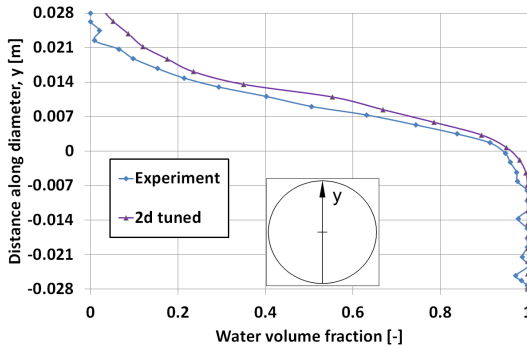


Fig. 10 water volume fraction profile predicted with a “tuned” 2 droplet classes model for Case 2.

Case 3: $\theta = 25^\circ$, IDo/w & W

A simulation was made using four droplet classes and the inlet size fraction as given by the droplet distribution model (table 11).

Table 11. Droplet size distribution parameters used for the CFD simulation

Droplet class	d [mm]	Inlet size fraction
1	1.2	0.25
2	3.7	0.36
3	6.1	0.28
4	8.5	0.11

Results are shown in fig 11. The agreement is improved in the upper part of the pipe (average difference of 0.06 with the reported water volume fraction profile).

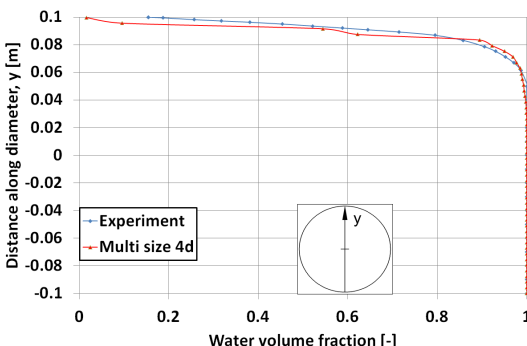


Fig. 11 water volume fraction profile predicted with a 4 droplet classes model for case 3.

Mixture velocity profile prediction

The computed mixture velocity profiles are shown below for all cases. There was no experimental data available except for case 3, so the figures are displayed for referential

purposes only.

Case 1: $\theta = 0^\circ$, Do/w&W

This flow pattern presents a parabolic mixture velocity profile, with its peak value shifted slightly towards the upper part of the pipe.

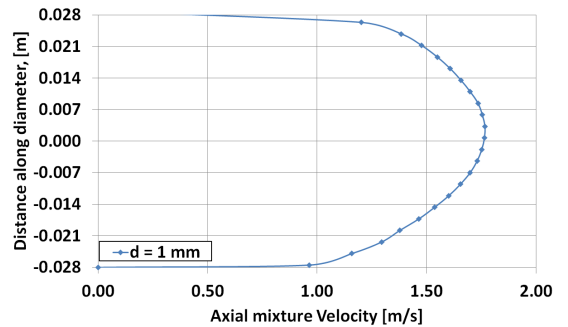


Fig. 12 Mixture velocity profile predicted for case 1 for a mono-dispersed model

Case 2: $\theta = 0^\circ$, Do/w&w/o

Fig. 13 below shows the computed mixture velocity profile compared with the experimental profile. The two profiles are parabolic, however the measured velocity profile has higher velocity values than the predicted profile. The average deviation between the simulation and the experiment is 0.13 m/s.

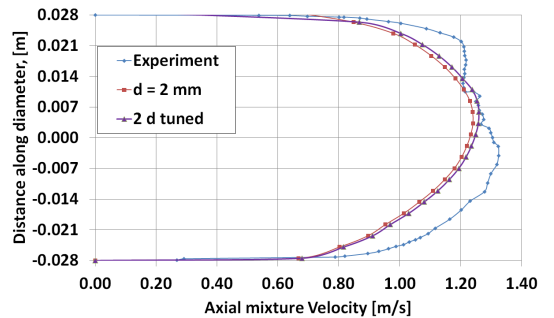


Fig. 13 Mixture velocity profile predicted for case 2 for a mono-dispersed model and a 2 class dispersion model

Case 3: $\theta = 25^\circ$, I Do/w&W

The predicted mixture velocity profiles present high values at the top of the pipe and downwards flow at the bottom of the pipe (Fig. 14). This is consistent with the expected dynamics of this flow pattern.

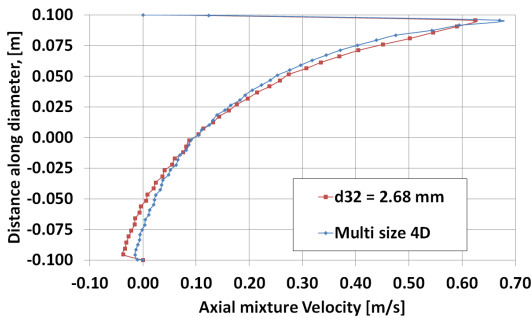


Fig. 14. Mixture velocity profile predicted for case 3 for a mono-dispersed model and a 4 droplet class dispersion model

The height of the recirculating layer is bigger for the mono-dispersion simulation.

Case 4: $\theta = 25^\circ$, $D_0/w\&W$

The predicted mixture velocity profile present high values at the top of the pipe and small values at the bottom of the pipe (Fig. 15).

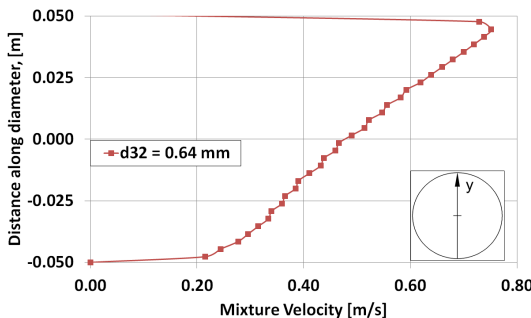


Fig. 15. Mixture velocity profile predicted for case 4 for a mono-dispersed model.

Case 5: $\theta = 25^\circ$, $D_0/w\&W$ BF

The predicted mixture velocity profiles present high values at the top of the pipe and downward flow in the lower half of the pipe (Fig. 16).

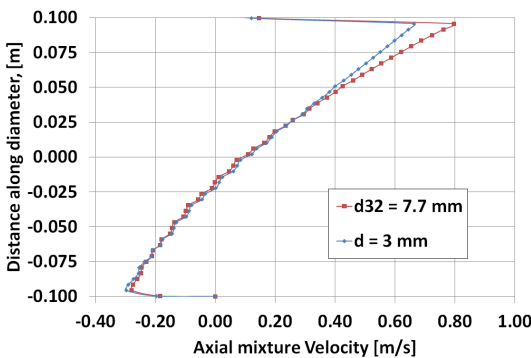


Fig. 16. Mixture velocity profile predicted for case 5 for a mono-dispersed model.

Conclusions

Mono-dispersion simulations showed a fair agreement with the experimental water volume fraction profiles when an adequate droplet diameter is used. The droplet diameter can, for some cases, be used as a tuning parameter to match to a certain tolerance the model results to the experimental data.

The manual adjust of the parameters (droplet diameters and size fraction) of a two droplet class dispersion simulation allowed a better representation of the experimental water volume fraction profile.

For small pipe diameter-high velocity cases the maximum droplet size predicted is qualitatively smaller than the average droplet size observable on the tests. The MUSIG model estimates a droplet size similar in size to the average particle size observable in the tests and the results have a fair agreement with the experimental volume fraction and velocity profiles.

The prediction of water volume fraction profiles using the proposed CFD methods was adequate for high water cuts (> 0.75).

A multi-size dispersion simulation using data from the ULLND model or the MUSIG model did not improve the prediction significantly of the CFD model compared to the mono-dispersed approach.

References

- ANSYS CFX-solver 13.0 modeling guide. Ansys Inc. (2010)
- Brauner, N. Liquid-Liquid Two-phase Flow Systems. Modeling and Control of Two-Phase Flow Phenomena. Ed V Bertola. CISM Center, Italy. (2004).
- Flores, J., X. Chen, C. Sarica, and J. Brill. Characterization of oilwater flow patterns in vertical and deviated wells. SPE Annual Technical Conference and Exhibition, San Antonio, Texas. (1998).
- Kumara, W., B. Halvorsen, and B. Melaen. Pressure drop, flow pattern and local water volume fraction measurements of oil-water flow in pipes. Meas. Sci. Technol 20. (2009a).
- Kumara WAS, Halvorsen BM, Melaen MC, Particle image velocimetry, gamma densitometry and pressure measurements of oil-water flow. Multiphase Science and Technology, 21 (1-2) (2009), pp. 51-64. (2009b).
- Rivera, R, Golan, M, Friedemann, J, Bourgeois, B.. Water Separation From Wellstream in Inclined Separation Tube With Distributed Tapping. SPE article N°102722. SPE Journal of Projects, Facilities & Construction. (2008).
- Simmons, M. and B. Azzopardi. Drop size distributions in dispersed liquid-liquid pipe flow. International Journal of Multiphase Flow 27, 843-859. (2001).
- Stanko, M. Analysis of the gravitational segregation phenomenon in water oil flows using CFD tools. Análisis del Fenómeno de Separación Gravitacional agua-petróleo utilizando herramientas DFC. Master thesis (In Spanish). Universidad Simón Bolívar. (2009).

- Tabeling, P. and B. Theron. Method of analyzing a two-phase flow in a hydrocarbon well. US patent No. 5.361.206. (1994).
- Vigneaux, P., G. Catala, and J. Hulin. Oil/water flow structure measurements in inclined pipe. SPE Annual Technical Conference and Exhibition, Houston, Texas. (1988).
- Xu, J., D. Li, J. Guo, and Y. Wu. Investigations of phase inversion and frictional pressure gradients in upward and downward oil water flow invertical pipes. International Journal of Multiphase Flow 36, 930–939. (2010).

Appendix I: Droplet size prediction

The function used for predicting the droplet size distribution is the upper-limit log-normal (ULLN). This distribution function is used to calculate the size fraction of a droplet class of diameter “d” in the dispersion.

The cumulative size fraction distribution function (CV) of droplet classes with diameters smaller or equal than d is given by eq. 5 below:

$$CV(d) = \frac{1}{\sqrt{\pi}} \cdot \int_{\delta \cdot z}^{\infty} \exp(-x^2) \cdot dx \quad (5)$$

Where:

$$z = \ln\left(\frac{a \cdot d}{d_{\max} - d}\right) \quad (6)$$

The values of δ and a (1.35 and 0.61 respectively) were taken from the work of Simmons and Azzopardi (2001). The maximum diameter exhibited for the dispersion (d_{\max}) was taken as the maximum between the model of Hinze (Brauner 2004) for dilute dispersions (eq. 7 below) and Brauner (2004) for dense dispersions (eq. 8 below):

$$\left[\frac{d_{\max}}{D}\right]_{\text{diluted}} = 0.55 \cdot We_w^{-0.6} \cdot f_{ip}^{-0.4} \quad (7)$$

$$\left[\frac{d_{\max}}{D}\right]_{\text{dense}} = 2.22 \cdot We_w^{-0.6} \cdot \left[\frac{\rho_M}{\rho_w \cdot (WC)} \cdot f_{ip}\right]^{-0.4} \cdot \left[\frac{(1-WC)}{(WC)}\right]^{0.6} \quad (8)$$

Where f_{ip} is the two-phase friction factor, and We_w is the water Weber number.

$$We_w = \frac{\rho_w \cdot V_M^2 \cdot D}{\sigma} \quad (9)$$

For the present work, the two phase friction factor was estimated by using a single phase friction factor correlation as suggested by Flores et al. (1998) (eq. 10).

$$f_{ip} = C_f \cdot Re_M^{-n_f} \quad (10)$$

Where the Reynolds number is:

$$Re_M = \frac{\rho_M \cdot V_M \cdot D}{\mu_w} \quad (11)$$

The maximum diameter predicted by the expressions of Hize and Brauner is very sensitive to the two phase friction factor correlation employed. The values of C_f and n_f are 9.078E7 and 1.822 respectively. These values were taken from the work of Xu et al. (2010) from the fitting made to the experimental results of Abduvayt et al. The Sauter mean diameter is calculated by the following expression:

$$d_{32} = \frac{d_{\max}}{1 + a \cdot \exp\left(\frac{1}{4 \cdot \delta^2}\right)} \quad (12)$$

Discretization procedure for N droplet classes

1. The diameter of each droplet class is calculated as

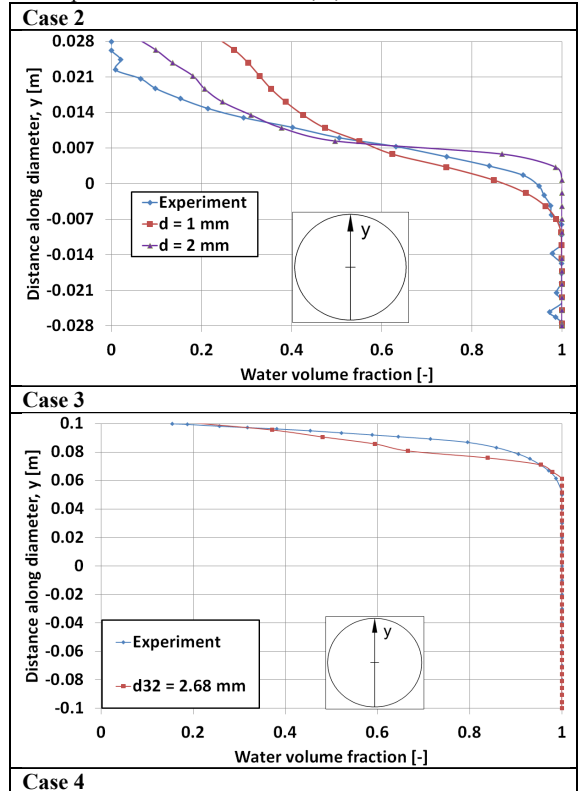
$$d_i = \left(i - \frac{1}{2}\right) \cdot \left(\frac{d_{\max}}{N}\right) \quad (13)$$

2. The size fraction of each droplet class is calculated as:

$$f_i = CV\left(i \cdot \left(\frac{d_{\max}}{N}\right)\right) - CV\left((i-1) \cdot \left(\frac{d_{\max}}{N}\right)\right) \quad (14)$$

Appendix II: Computed water volume fraction profiles using a mono-dispersion for cases 2, 3, 4 and 5.

Table 12. Results of a monodispersed CFD simulation with the experimental data for cases 2, 3, 4 and 5.



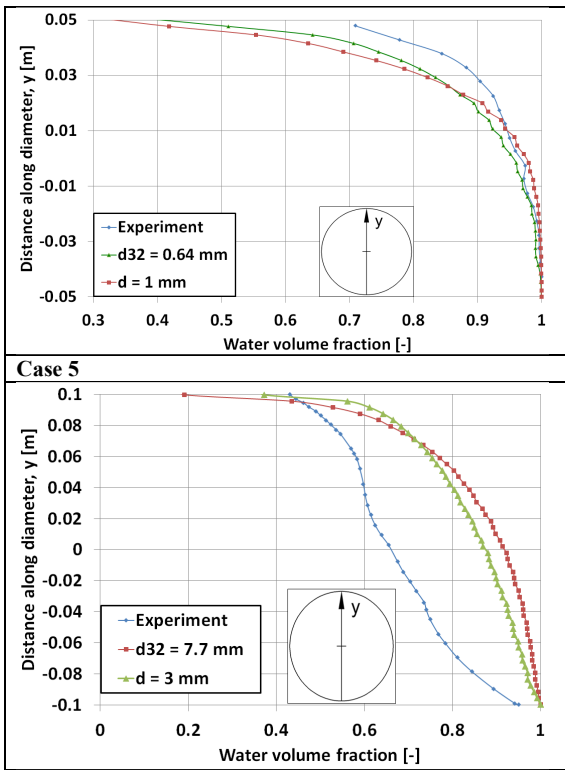


Table 13. Comparison of the mono-dispersed results against the experimental data for cases 2, 3, 4, 5.

Case N ^o	Droplet diameter	Δp -Diff. with exp. [%]	H_w - Diff with exp. [%]	α_w profile average diff. with exp. [-]
Case 2	d = 1 mm	0.2	6.6	0.09
	d = 2 mm	0.4	6.4	0.05
	d = 3 mm	1.3	6.1	0.06
Case 3	d ₃₂ = 2.68 mm	-	0.6	0.05
Case 4	d ₃₂ = 0.64 mm	-	2.0	0.04
	d = 1 mm	-	3.1	0.05
Case 5	d ₃₂ = 7.7 mm	-	31.8	0.18
	d = 3 mm	-	27.8	0.16

Chapter 2

Model based constrained optimization for production networks with ESP-produced, high water cut wells

2.1 Introduction

This research investigates certain features of a model-based constrained optimization of an oil field production system. The system constitutes of clusters of high water cut, low GOR oil wells producing by ESP (Electric Submersible Pumps) which converge into a multi-branched surface gathering system. The optimization strategy consists on modifying the ESP frequencies to maximize oil production while honoring several operational constraints.

The production of individual oil and gas wells in large fields is piped to the field processing facilities or to the field export points through a surface gathering system. The flow system is normally arranged as a converging network of material streams. The layout of gathering systems in oil and fields may differ considerably depending on the field layout, its wells and facilities spread, and on the geographical environment such as offshore platforms, subsea production, small land based fields or large land based fields.

The production gathering system addressed in this study is typical for large onshore fields with a number of clusters of wells, referred to as well-clusters, or well-pads. The wellheads at the cluster are rather close and utilize joint facilities such as electrical supply and access road.

The production of individual wells in the cluster, the material network source, is gathered and commingled in a production manifolds, normally adjacent to the wellhead cluster. In large multi-cluster fields, with a single separation and processing plant (the material sink at the end of gathering system), the clusters are piped and merged at junctions into sub trunk lines (feeder lines), and main truck lines that commingle and produced the entire field, or a major segment of the field, to the processing plant (Fig. 2.1).

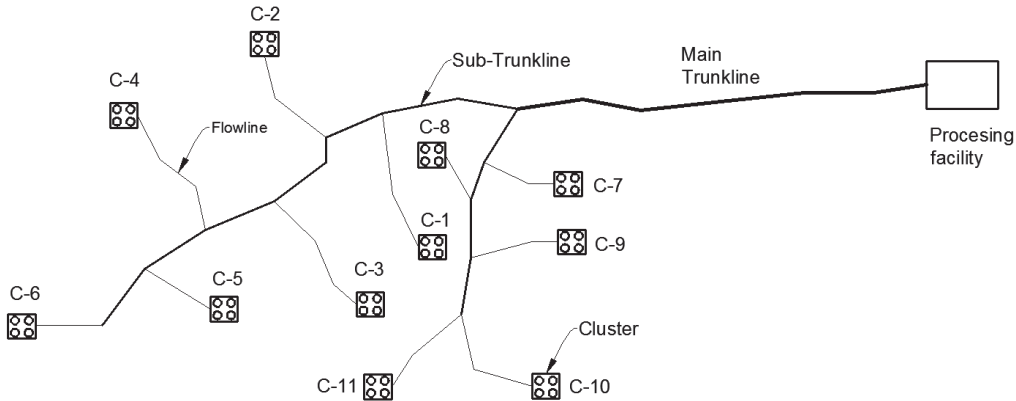


Fig. 2.1 Scheme of a surface network in a hydrocarbon production system with 4-wells cluster

Modeling and optimizing the production of the illustrated gathering system is complicated mainly due to the interdependency of the production output of the individual wells. Practically, modeling and optimization tasks of such multiwell systems are performed by a computerized process. As the number of wells, the type and number of production control measures, and the number of production constraints in the system increase, the system models and its optimization function become complicated and the computation of maximum oil production or other production optimization objectives becomes very challenging.

The production cases addressed in this work are of oil wells producing by down-hole ESP (Electric Submersible Pumps). The wells output is controlled by varying continuously the operating frequency of the ESPs. The operating frequency is expressed in Hz ($\text{Hz}=\text{cycle}/\text{sec}$). Wellhead chokes are either fully open or do not exist. The modeling of the system is a computerized numerical process that involves calculations of the flow rates and the associated pressure and temperature in the network. The search for the optimum state in the addressed problem is conducted in an iterative manner employing mathematical optimization techniques that vary step-wise the inputs to the system model and searching for the optimum output as the process progresses. The production system modeling and the optimization were performed using a canned commercial software and MS Excel.

The chapter is structured in the following manner: To identify the hurdles and hindrances often encountered in computing the global optimum production state of large fields with a large number of ESP produced oil wells, two scaled down cases are considered: (1) a single 2-well cluster and (2) two clusters with 3-wells each. A third case (3) of a real field production system with 41 wells with ESP pumps is presented for referential purposes.

2.2 Basics of the model-based optimization

Fig. 2.2 illustrates schematically an optimization loop in the optimization search process. In the computation process the optimization engine employs an algorithm to change the ESP frequencies of the wells to stepwise approach a global maximum hydrocarbon production. The production system model then solves the hydraulic equilibrium and the solution is fed back to the optimization engine. The optimization engine checks if the constraints are met and if the maximum is reached. If not, a new set of variables is generated by the optimization algorithm and the process is repeated once again.

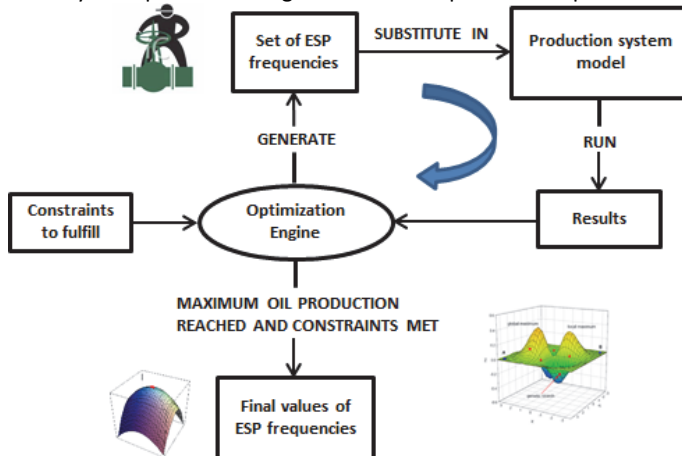


Fig. 2.2 Production optimization routine for a hydrocarbon production system with surface network

In practical production management, the mathematically obtained optimum is not necessarily the desired practical optimum. Sometimes “near optimum” state is more beneficiary from variety of practical and operations reasons. Such points can be obtained from reviewing in the history of the optimization process and the list of states computed in the path to the mathematical optimum. Thus, in addition to

calculating the optimum state, the computations performed in this study captured and report the history of the optimization computation.

2.3 Modeling cases and considerations

The field production systems addressed in the study is an oil field with high producing water cut, negligible GOR, vertical wells, and variable speed ESPs installed downhole.

The production modeling and optimization techniques and tools employed for each case are presented in Table 2.1.

Table 2.1 Production system modeling and optimization tools employed for each case

Case N°	Production system modeling	Optimization
Case 1	Pipesim®	Visual inspection of color maps generated using a case matrix
	Pipesim®	Pipe-It® (IPOPT solver)
Case 2	Pipesim®	Pipe-It® (IPOPT solver, Reflection solver and NOMAD solver),
	Pipesim®	Pipesim optimizer ®
	MS Excel®	Excel solver (GRG)
Case 3	Pipesim®	Pipe-It® (IPOPT solver)

The linking and information transfer between Pipesim and Pipe-It was performed by setting up a Pipe-It project. The Pipe-It project is a Pipe-It proprietary file type that contains all the programmable logic for passing data from one software to another. The access to Pipesim functionalities and variables from Pipe-It was done by employing the Openserver built in capability of Pipesim. The Pipe-It project was developed by Solrud (2012), Røyset (2013) and the author.

Commercial programs for production modeling and optimization differ considerably in the procedures used for solving the production network, in the manner the streams sources (wells or reservoir) input to computer the network. These variations are beyond the scope of this paper and a single commercial program is used to assess some features of various optimizers.

General considerations

The wells architecture and the gathering system layout as well as the system dimensions and data, ESP models, fluid characteristics and all other data relevant to system modeling and optimization are presented in Appendix A2. The main features of the system are as follows:

- The source of flow for each well is expressed analytically by a linear relationship between the bottomhole flowing pressure and the inflow volumetric rates of oil and water (also known as Inflow Performance Relationship or IPR).
- The well water cut is rate independent and the GOR is negligible
- The compressibilities of oil and water are negligible (only for the MS Excel model)
- The pipe wall wetting phase is water and the rheology of the flowing oil-water mixture is simple without phase inversion phenomena.
- The fluid flow is considered isothermal and thermal calculations are excluded from the modeling

2.4 Case 1. Two oil wells with common wellhead manifold discharging to a pipeline

Case 1 is illustrated in Fig. 2.3. The two wells have a commingling point and a common wellhead pressure at the wellhead manifold. The production is routed through a common horizontal pipeline to a constant pressure separation station. The two wells produce for the same reservoir and assumed to have identical reservoir pressure and have a similar mechanical layout. Well 1 has a producing water cut of 50%, and well 2 has a producing water cut of 90%. The system was modeled using the software Pipesim® and the optimization was made with the software Pipe-it®.

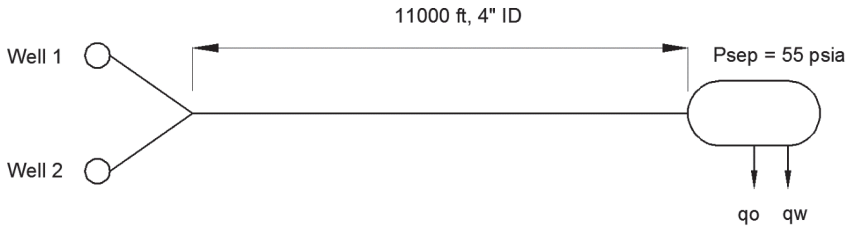


Fig. 2.3 Layout of case 1: two wells with common wellhead manifold discharging to a pipeline

The formulation of the optimization problem, optimization function and, the control variables (pumps frequencies), and the constraints, is the following:

$$\begin{aligned}
 &\textbf{Maximize: } q_o(f_1, f_2) \\
 &\textbf{with } f_1, f_2 \in (30 \dots 60) \text{hz} \\
 &\quad p_{ps1}, p_{ps2} \geq 300 \text{ psia} \\
 &\quad p_{wh} \leq 400 \text{ psia} \\
 &\textbf{Subject to: } \\
 &\quad q_1, q_2 \geq q_{\min esp} \\
 &\quad q_1, q_2 \leq q_{\max esp}
 \end{aligned}$$

Where f_1 and f_2 are the ESP frequencies, P_{ps1} and P_{ps2} are the suction pressures of the pumps and q is the liquid flow rate of the well.

The optimization engine of Pipe-It[®] modifies the frequencies of ESPs 1 and 2 (f_1 and f_2) iteratively to maximize total oil production. The minimum allowable suction pressure of the ESPs, reflecting the pump NPSH (Net Positive Suction Head) requirements, is 300 psia, and the maximum allowable wellhead pressure (p_{wh}) is 400 psia (because of pipeline pressure rating). The ESP pumps are constrained by minimum and maximum allowable flow rates. These minimum and maximum allowable flow rates depend on the ESP operational frequency of the ESP.

The optimization method selected for this case is the IPOPT solver (Wächter & Biegler 2006). This is a derivative based method. A software package for IPOPT non-linear optimization is included as an optimization option in Pipe-It[®]. The optimum solution was found after 40 iterations, and a running time of 6 min. The starting frequency values where $f_1 = 30$ hz and $f_2 = 30$ hz. The maximum oil production found was 3709.8 bbl/d corresponding to frequency values of $f_1 = 60$ hz and $f_2 = 47.2$ hz.

In order to demonstrate and investigate graphically the optimization process, a color map was made showing the oil production for each combination of ESP frequencies (Fig. 2.4). Fig. 2.4.a shows that increasing the ESP frequencies of the wells increases the oil production. However an increase of the frequency of well 1 has more impact on the amount of oil produced than well 2 (due to the fact that Well 1 has a lower water cut). The graph shows that if the constraints are not considered, the maximum oil production occurs when $f_1 = 60.0$ hz and $f_2 = 41.7$ hz ($q_o = 3723.9$ bbl/d, marked with a blue point in the plot).

Fig. 2.4.b. shows the combinations of f_1 and f_2 for which the constraints violate the specified bounds (maximum allowable wellhead pressure, minimum and maximum allowable ESP flow rates and simultaneous production of the two wells). The constraints that impose the biggest operational limitations are the minimum allowable ESP flow rates. This is an indicator that the two ESPs installed are oversized with respect to their pumping capacity.

In Fig. 2.4.c. the regions where there is a violation of the constraints were eliminated from the plot. This to limit the available domain for optimization. The maximum obtained using Pipe-It[®] was plotted with a blue circle ($q_o = 3709.8$ bbl/d). It can be seen that it coincides with the maximum amount of oil within the feasible ESP frequency region.

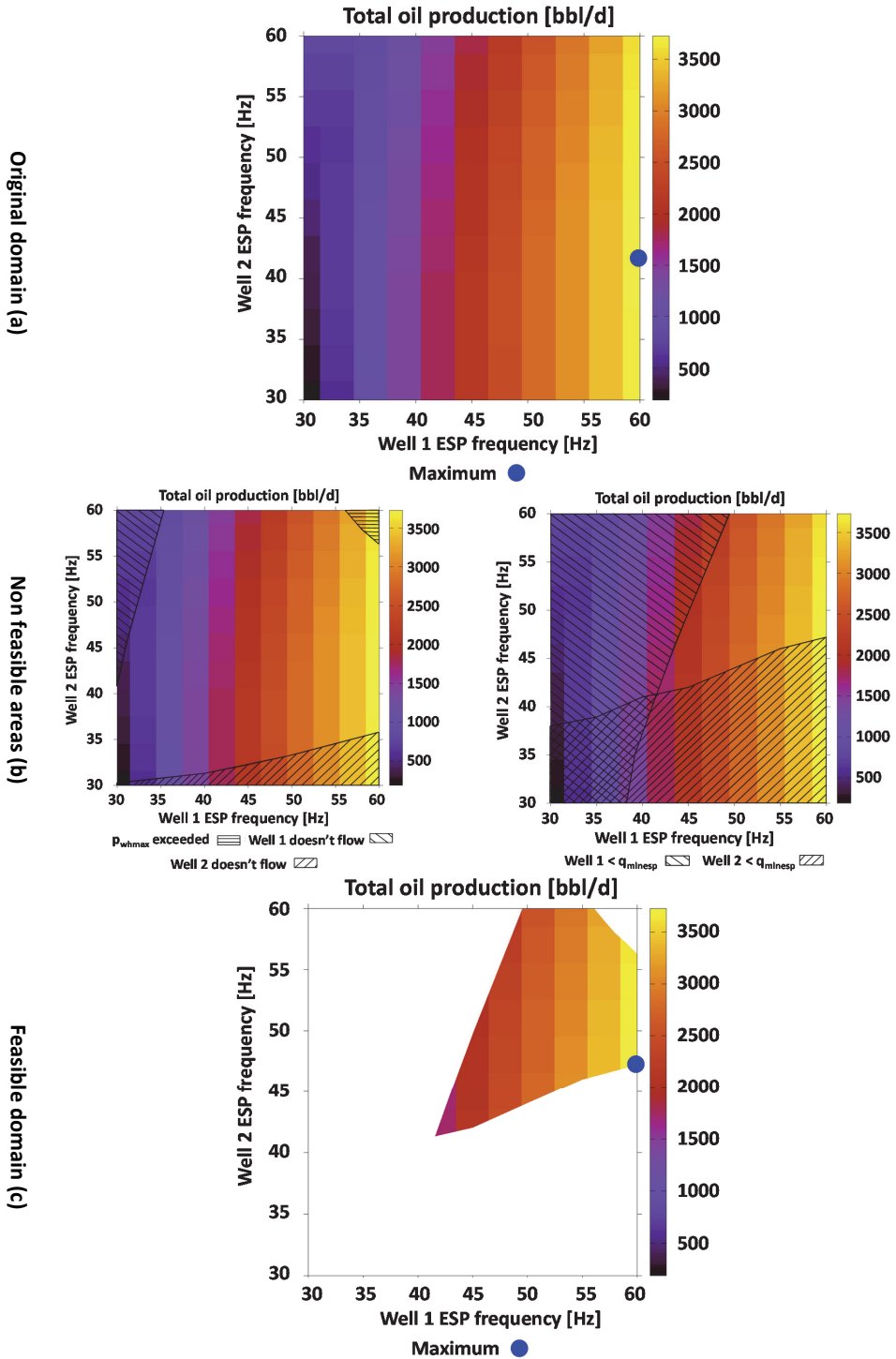


Fig. 2.4 Total oil production color map for the complete ESP frequency range of wells 1 and 2

A practical observation from the optimization map is that a smaller ESP with a lower allowable flow rate in Well 1 expands the allowable ESP frequency region and yields a higher total oil production (+ 20bbl/d).

2.5 Case 2: Two clusters of three wells each discharging to a common pipeline

Case 2 is illustrated in Fig. 2.5. The wells of each cluster have a common wellhead pressure. All the pipelines are horizontal.

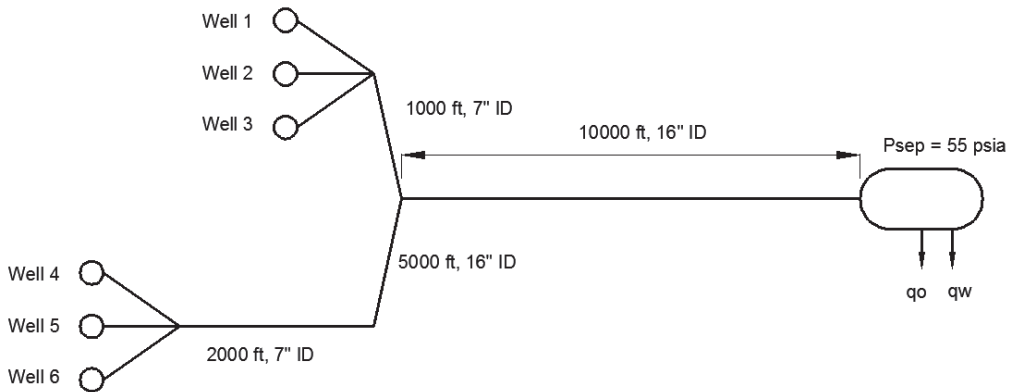


Fig. 2.5 Layout of case 2: 2 clusters of 3 wells each discharging to a common pipeline

The production system was modeled by two models one implemented with MS excel and the other with Pipesim®. For models control and verification purposes, the production rate results of the two models were compared for 4 sets of frequencies. The MS excel model exhibited an average deviation of 5.5% from the Pipesim® results. The maximum difference found was 28 % (between calculated liquid flow rates at low pump frequencies). The differences can be attributed to two issues; (a) the degree of the polynomial expression representing the ESP performance curve in MS Excel and, (b) differences in pressure gradient and pressure traverse calculations of oil water mixture in pipe flow.

The formulation of the optimization problem in this case includes 6 decision variables and is given as follows:

$$\begin{aligned}
 &\text{Maximize: } q_o(f_1, f_2, f_3, f_4, f_5, f_6) \text{ with } f_1, f_2, f_3, f_4, f_5, f_6 \in (30 \dots 60) \text{ hz} \\
 &\quad q_w \leq 30000 \text{ bbl/d} \\
 &\text{Subject to: } P_{ps1}, P_{ps2}, P_{ps3}, P_{ps4}, P_{ps5}, P_{ps6} \geq 300 \text{ psia} \\
 &\quad q_1, q_2, q_3, q_4, q_5, q_6 \geq q_{\text{min esp}} \\
 &\quad q_1, q_2, q_3, q_4, q_5, q_6 \leq q_{\text{max esp}}
 \end{aligned}$$

The optimization of the production system was performed using three tools: (a) MS Excel solver, (b) the Well Optimizer module (Schlumberger 2011) available within the Pipesim® program and (c) the optimization module of Pipe-It® (Petrostreamz 2013) linked to the Pipesim model . Due to the commercial software limitations the three last constraints (ESP suction pressure, minimum flow rate and maximum flow rate) are not included in Well Optimizer® analysis.

The outcome of the five optimizations engines are presented in Table 2.2 and Table 2.3. Table 2.2 lists the various optimization engines used for optimizing this case and their corresponding number of iterations and process time to reach the optimum state. Table 2.3 lists the final optimization state for each of the listed optimization engines, given the optimum production rates and relevant pump frequencies.

Table 2.2 Parameters of the optimization engines employed in case 2

Optimization engine	Method	Iterations	Time [min]	Starting point
MS Excel solver	GRG non linear (Frontline systems 2013)	-	553	Multistart, automatically, population: 2000
Pipesim [®] Well optimizer	SDR MINLP (Schlumberger 2011)	7	5	Automatic
Pipe-It [®] - IPOPT	Interior-Point line-search filter method (Wächter & Biegler 2006)	1530	280	30 Hz for all ESPs
Pipe-it [®] - Reflection	Nelder-Mead Simplex	570	240	30 Hz for all ESPs
Pipe-It [®] - NOMAD	Mesh adaptive direct search (MADS) (Le Digabel 2011)	2292	360	30 Hz for all ESPs

The fastest optimization engine time wise is the Well Optimizer of Pipesim[®]. The MS Excel solver is the slowest of all, probably due to the fact that the optimization engine conducts simultaneously the hydraulic network solving and the oil production maximization.

Table 2.3 Optimum frequencies found with different optimization engines

Model	Optimizer Engine	q_o [bbl/d]	q_w [bbl/d]	f_1 [Hz]	f_2 [Hz]	f_3 [Hz]	f_4 [Hz]	f_5 [Hz]	f_6 [Hz]
MS Excel*	MS Excel solver	3541	30000	42.7	37.2	60.0	37.1	60.0	50.8
Pipesim [®]	Pipesim [®] Well optimizer	2416	25246	39.8	40.5	40.5	42.2	43.2	41.4
Pipesim [®]	Pipe-It [®] - IPOPT	3553	29988	45.6	36.6	59.9	36.4	60.0	45.4
Pipesim [®]	Pipe-it [®] - Reflection	3264	30000	60.0	37.5	50.9	42.8	56.0	35.4
Pipesim [®]	Pipe-it [®] - NOMAD	3534	30000	53.1	36.6	59.8	36.3	52.3	45.2

The biggest production of oil was calculated with the optimizer Pipe-It[®] IPOPT, followed by NOMAD, Reflection, and Well optimizer.

As mentioned earlier, the network model in Excel yields slightly different results from the Pipesim[®] model so the optimization results with Excel and Pipesim in Table 2.2 and Table 2.3 are not directly comparable.

The Well Optimizer found an optimum but the value is below the optima obtained by all the other methods. The optimum found with Pipe-It Reflection reached the limit in water production and in q_{minesp} for well N° 4. The optimizer Pipe-It[®] NOMAD reached the limit in water production and the limit in q_{minesp} for wells 2 and 4.

Fig. 2.6 maps the pump frequencies obtained at the optimum state of the various optimization engines.

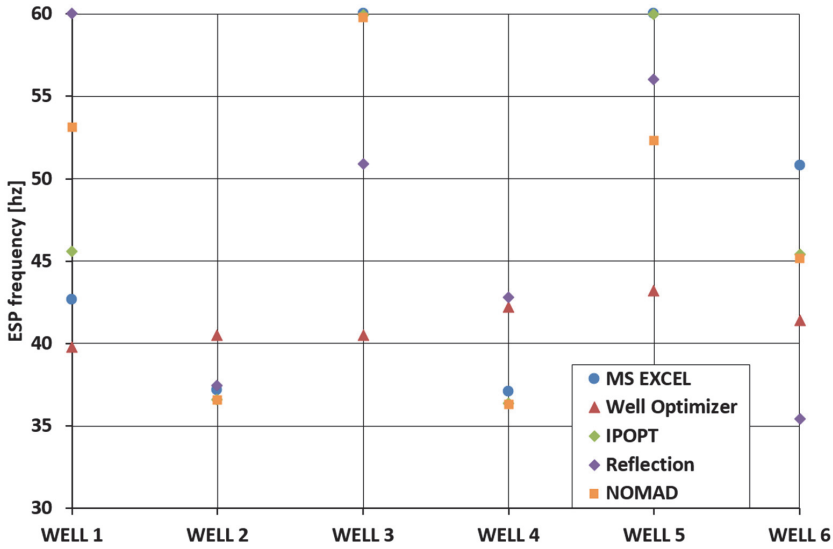


Fig. 2.6 Optimum frequencies found with different optimization engines

From Fig. 2.6 one observes that for the IPOPT case the optimum frequencies are maximum for wells 3 and 5 (wells with the lowest water cut), minimum for wells 2 and 4 (wells with highest water cut) and intermediate for wells 1 and 6. This set of optimum frequencies is very similar to the one calculated by MS Excel. These two cases reached the limit in q_{minesp} for wells 2 and 4.

Fig. 2.7 displays the history of the optimization process. It shows the total oil production calculated in each iteration step of the Pipe-it[®] optimizers (which had open access to this information): IPOPT, Reflection and NOMAD. All engines shown in the graphs departed from the same initial conditions.

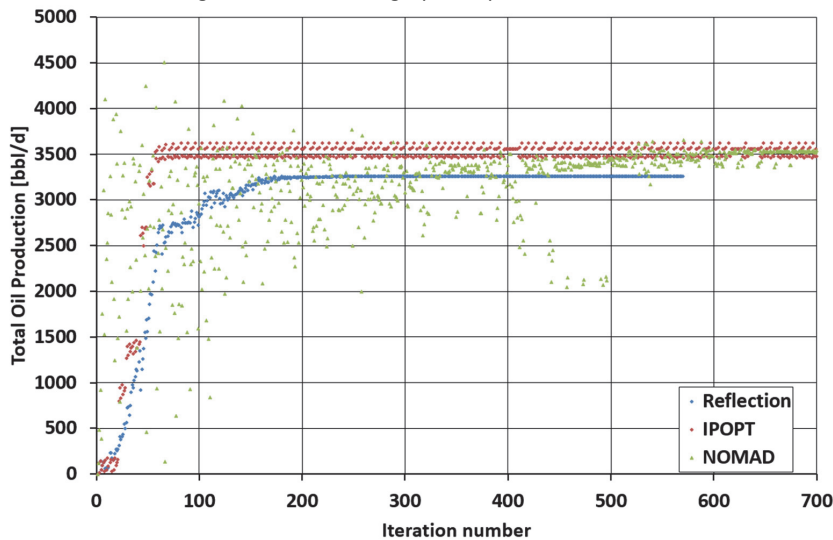


Fig. 2.7 Oil production vs. Iteration number from iteration N°1 to 700 for Pipe-It[®] optimizers: IPOPT, Reflection and NOMAD

It is possible to observe in Figure Fig. 2.7 that IPOPT reaches in fewer iterations oil production values close to the maximum than the other methods. Timewise, this makes this method the most efficient. For the cases of IPOPT and Reflection the oil production increases gradually along the iterative process until it stabilizes at values close to the final maxima obtained. After that, both convergences seem to reach

a numerical stagnation zone. In a numerical stagnation zone the changes in the optimization function are big enough not to meet the preset convergence tolerance but small enough that do not allow to progress towards the optimum.

In the case using the NOMAD solver there seem to be scattered evaluations from the beginning, until gradually, after iteration 500, it is stabilized around the final maximum reported. This is in agreement with the classification of NOMAD (Le Digabel, 2011) as a derivative free global search method.

2.6 Case 3: Real field production network model.

Case 3 is an onshore heavy oil field producing with high water cut and low GOR. The production network is illustrated in Fig. 2.8. The wells are organized in clusters and the production is collected and transported with a pipeline network to the separation facilities. Most of the wells have ESPs installed and a few have PCP (Progressive cavity pump). There is a loading terminal (named “source” in Fig. 2.8) where a constant amount of hydrocarbons are injected into the network from a neighbouring field.

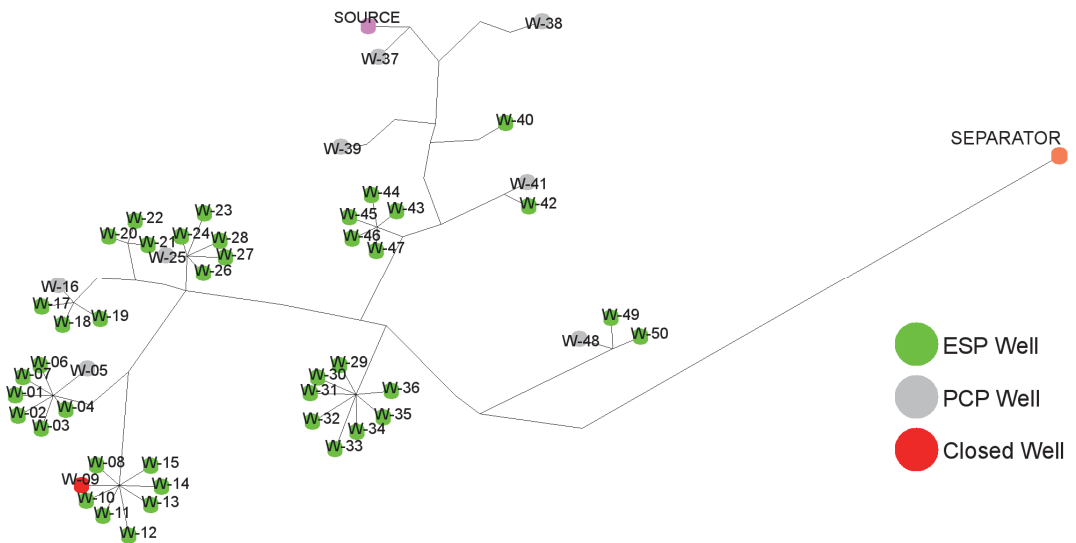


Fig. 2.8 Layout of case 2: 2 clusters of 3 wells each discharging to a common pipeline

The computer model of this system was available in Pipesim. The optimization was made with the software Pipe-it® using the IPOPT optimizer. The starting state of the Pipesim model for the optimization had substituted the current operating ESP frequencies. The formulation of the optimization problem in this case includes 41 decision variables and is given as follows:

$$\text{Maximize: } q_o(f_1, f_2, \dots, f_{41}) \text{ with } \begin{cases} \text{if } f \geq 60 \text{ then } f_1, f_2, \dots, f_{41} \in (30 \dots 60) \text{ hz} \\ \text{else } f_1, f_2, \dots, f_{41} \in (58 \dots 66) \text{ hz} \end{cases}$$

$$q \leq 286000 \text{ bbl} / d$$

$$\text{Subject to: } P_{ps1}, P_{ps2}, P_{ps3}, \dots, P_{ps41} \geq 200 \text{ psia}$$

$$q_1, q_2, q_3, \dots, q_{41} \leq 12000 \text{ bbl} / d$$

The optimization was stopped manually after 523 iterations and a total runing time of 9.5 hrs. The oil and water production and the ESP power consumption for the starting conditions and the optimum are presented in Table 2.4. The oil production of the optimum point is 18% higher than the oil production of the current operation (starting point).

Table 2.4 Comparison of the performance indicators of the current operation and the minimum

	Oil production	Inc.*	Water production	Inc.	ESP power	Inc.
	[bbls/d]	[%]	[bbls/d]	[%]	[hp]	[%]
Current operation	25207.9	-	239902.6	-	5860.2	-
Optimum	29831.8	+18.3	255779.6	+6.6	6846.3	+16.8

During the optimization iterations a total of 493 points were “feasible solutions” (complied with the specified constraints). The oil and water production of these 493 points were extracted and plotted in Fig. 2.9. In this figure three conditions have been highlighted with red arrows: the current operating conditions, the optimum found with the optimizer and a third point that produces 11% more oil but roughly the same amount of water. If the water production is a bottleneck this third point could adopted as a “practical” optimum.

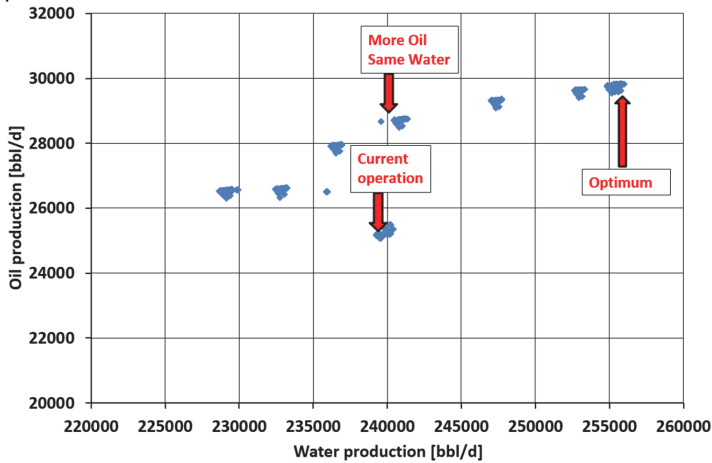


Fig. 2.9 Oil production vs. water production, feasible solutions

Fig. 2.10 shows the frequencies and Watercut for each well for the starting point (current operation, base case) and for the optimum. The frequencies of wells with low water cut have been increased.

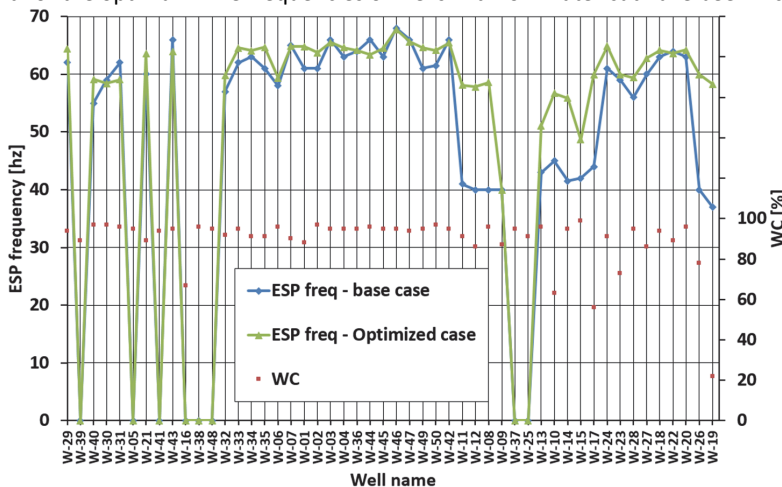


Fig. 2.10 ESP frequency and Watercut vs well name for base case and optimum

Conclusions and Recommendations

1. The chapter presents a general methodology to execute model-based production optimization of oil production systems comprised of wells with ESP and gathering system with high hydraulic interdependence between the system elements and with multiple operational constraints.
2. The study addresses a scaled-down field production system to allow easy observations on the behavior of the optimization process. The study does not constitute a systematic comprehensive study of the performance of the various optimization methods.
3. The optimization results indicate that even for the simplest case of two wells, the ESP frequency values for maximum oil production cannot be predicted intuitively by assuming maximum allowable frequencies. The maximum has to be search and calculated using a formal mathematic optimization procedure
4. In the simple case of two wells in one cluster, a graphical mapping of the optimization process revealed some interesting observations. The constraints imposed on the system are limiting considerably the domain available for optimization. The limited domain allows identification of oversized pumps and advice on better specification of the operation range of system elements.
5. In the six wells case, the highest oil production rate calculates by the optimizing program is obtained using derivative-based method (both in MS Excel and Pipe-It® IPOPT).
6. The constraints in the six well system create hindring in the progress of the optimum search process. The process might get “bogged down” in a stagnation zone where very small changes in the optimization function stops the search process, or the seach has to “cross” several regions of invalid solution and the search process might stop or divert away from progressing towards the optimum. In such cases, proper adjustment of the optimizer preference parametes is needed.
7. The ESP frequency optimization performed on a large real field model predicts a significant improvement with respect to the current operating conditions while honoring multiple operational constraints. This promotes ESP frequency optimization as a valuable tool for analyzing complex production gathering networks and encourages further investigation on the subject.
8. For large production networks the running time required for convergence could be so large that it becomes impractical. Thus a better strategy might be to run a finite number of iterations and then postprocess the pool of feasible solutions to find the most attractive operating conditions.

References

- Frontline systems. (2013). Basic solver algorithms and methods used. Retrieved from <http://www.solver.com/content/basic-solver-algorithms-and-methods-used>.
- Le Digabel, S. (2011). Algorithm 909: NOMAD: Nonlinear Optimization with the MADS Algorithm. *ACM Transactions on Mathematical Software*, 37 (4). P. 44:1-44:15.
- Petrostreamz. (2013). *Pipe-It User Guide .Optimizer*. Pp. 88. Trondheim, Norway.
- Røyset, O. L. (2013). *Simulating and optimizing production from a multi-well field*. (Master thesis), Norwegian University of Science and Technology (NTNU). Trondheim, Norway.
- Schlumberger. (2011). *PIPESIM User Guide. Well Optimizer feature description*. Pp. 19. Houston, USA.
- Solrud, S. Ø. (2012). *Simulating the production of a complex multi-well, multilayer field*. (Master thesis), Norwegian University of Science and Technology (NTNU). Trondheim, Norway.
- Wächter, A.; Biegler, L. (2006). On the implementation of an Interior-Point filter Line-Search Algorithm for Large-Scales Nonlinear Programming. *Mathematical Programming*. 106(1), pp. 25-57.

Appendix A2 General information about the considered production systems

General mechanical layout of the wells:

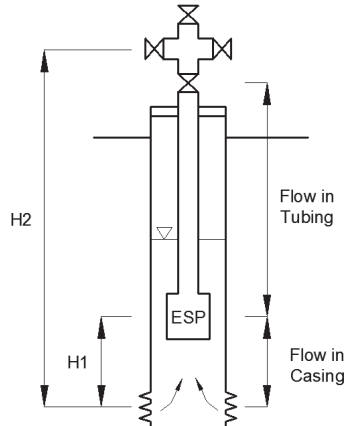


Fig. A2.1. Mechanical layout of the well

Fluid properties

Table A2.1. Fluid Properties

Fluid	Water	Oil
Density [lbs/ft ³]	64	56
Viscosity [cp]	1.00	1.31

Case 1 well performance and layout information

Table A2.2 Well performance and layout information for case 1

Wells	P _R	J, for total liquid flow	Well WF -water fraction	H1	H2	d1	d2	N° stages
-	[psia]	[STB/d/psi]	[fraction]	[ft]	[ft]	[in]	[in]	[-]
1	1000	20	0.50	700	3000	6	3	50
2	1000	30	0.90	700	3000	6	3	50

Case 2 well performance and layout information

Table A2.3 Well performance and layout information for case 2

Wells	P _R	J, for total liquid flow	Well WF -water fraction	H1	H2	d1	d2	N° stages
-	[psia]	[STBD/psi]	[fraction]	[ft]	[ft]	[in]	[in]	[-]
1	1000	50	0.90	700	3000	6	3	50
2	1000	40	0.98	700	3000	6	3	50
3	1000	30	0.85	700	3000	6	3	50
4	1000	45	0.95	700	3000	6	3	50
5	1000	25	0.89	700	3000	6	3	50
6	1000	60	0.90	700	3000	6	3	50

ESP information

Table A2.4 ESP information

ESP manufacturer:	WoodGroup
ESP model:	TE7000
Minimum allowable rate @ 60 hz [bbl/d]	4000
Maximum allowable rate @ 60 hz [bbl/d]	9700

For the MS Excel model and for the Pipe-It optimizers, the minimum allowable rate and maximum allowable rate for other operating frequencies were calculated using Eq. A2.1:

$$q_{\min esp}(f) = q_{\min esp}(60 \text{ hz}) \cdot \frac{f}{60 \text{ hz}} \tag{Eq.A2.1}$$

Single stage ESP TE7000 head and efficiency curve vs flow rate:

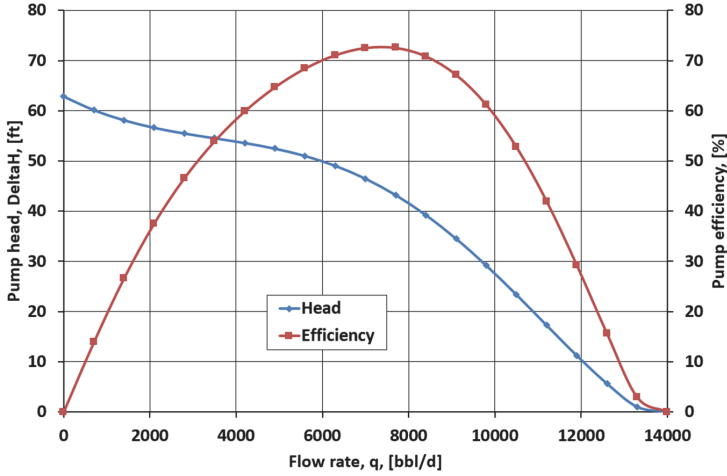


Fig. A2.2. ESP single stage head and efficiency curves vs flow rate for 60 hz.

For the MS Excel model, the ESP head curve has been fitted to a 4th degree polynomial as presented in Eq. A2.2. The values of the coefficients are presented in Table A2.5.

$$\Delta H = a_4 \cdot q^4 + a_3 \cdot q^3 + a_2 \cdot q^2 + a_1 \cdot q + a_0 \tag{Eq.A2.2}$$

Table A2.5 Fitting coefficients for ESP head curve @ 60 hz

Coefficient	Value
a_4 [ft/(bbl/d) ⁴]	8.6558E-15
a_3 [ft/(bbl/d) ³]	-2.4483E-10
a_2 [ft/(bbl/d) ²]	1.8590E-06
a_1 [ft/bbl/d]	-6.4086E-03
a_0 [ft]	63.53

For the MS Excel model, the estimation of the ESP head at other operating frequencies was done using Eq. A2.3.

$$\Delta H = \left(a_4 \cdot \left(\frac{60 \text{ hz}}{f} \right)^4 + a_3 \cdot \left(\frac{60 \text{ hz}}{f} \right)^3 + a_2 \cdot \left(\frac{60 \text{ hz}}{f} \right)^2 + a_1 \cdot \left(\frac{60 \text{ hz}}{f} \right) + a_0 \right) \cdot \left(\frac{f}{60 \text{ hz}} \right)^2 \tag{Eq.A2.3}$$

Appendix B2

Notes about solving using MS Excel the production hydraulic network of Case 1

A sketch of the production system of Case 1 displaying important nodes is presented in Fig. B2.1.

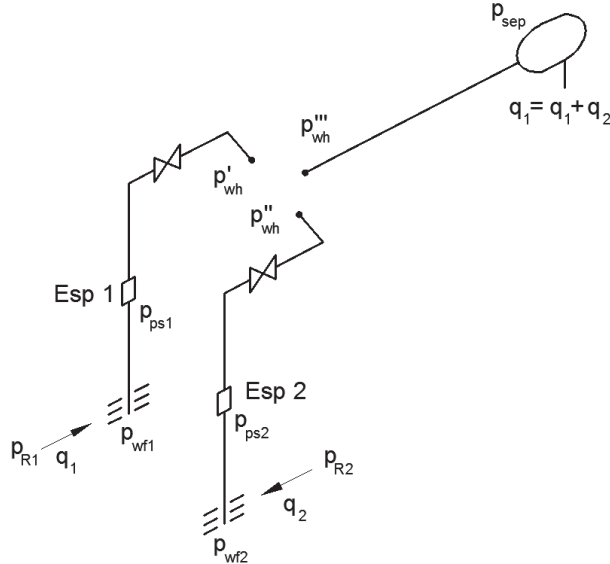


Fig. B2.1. Pressure points in the production system of Case 1

The methodology for solving the hydraulic equilibrium conditions of the system (for a fixed set of ESP frequencies) consist on the following steps:

1. Assume a bottomhole pressure for both wells
2. Use the inflow performance relationship of each reservoir to calculate the operating total liquid rate, oil and water rates.

$$q_T = J \cdot (p_R - p_{wf}) \quad \text{Eq.B2.1}$$

3. Perform pipe pressure drop calculations from the bottomhole of wells 1 and 2 to the ESP suction using the pressure drop relationship for pipes (Eq. B2.2)

$$p_{out} = p_{in} - \rho_{mix} \cdot g \cdot (z_{out} - z_{in}) - \rho_{mix} \cdot g \cdot \left(F_D \cdot \frac{L}{D \cdot 2 \cdot g \cdot A^2} \right) \cdot q^2 \quad \text{Eq.B2.2}$$

4. Calculate the pressure at the discharge of the ESP using Eq. B2.3 for wells 1 and 2

$$(p_{pd} - p_{ps}) = \rho_{mix} \cdot g \cdot N \cdot \Delta H \quad \text{Eq.B2.3}$$

5. Calculate the wellhead pressure using Eq. B2.2 from the ESP discharge for wells 1 and 2 (p'_{wh} and p''_{wh})
6. With the separator conditions, the sum of the two liquid rates and Eq. B2.3 calculate the wellhead pressure (p'''_{wh}).
7. Iterate on the bottomhole pressure for both wells until the three pressures (p'_{wh} , p''_{wh} , p'''_{wh}) are the same. This process is called hydraulic equilibrium calculation and it was done using the standard solver in Excel.

Chapter 3

Hydraulic analysis of a novel Hexagonal positive displacement pump

Some sections of this chapter were gathered into a paper and were published in the International Journal of Fluid Machinery and Systems (2012).

3.1 Introduction

This research performs a single phase hydraulic analysis of a particular type of positive displacement reciprocating pump released recently to the market and promoted with the brand name: "Hex pump". According to the vendor it has attractive features (special patented piston discharge flow rate profile, novel discharge gathering manifold, no need for pulsation dampener), that promise reduced output pulsation, small size and high efficiency. The intended and preferred application is for slurry pumping in the hydrocarbon drilling industry.

Reciprocating pumps, by the nature of their pistons motion kinematics, experience acceleration and deceleration of the pumped fluid at each pumping cycle. These produce oscillatory variations in flow and pressure at the piston discharge that may excite severe pressure pulsation in their discharge manifolds and piping systems. Therefore, the development of new designs of such pumps or introduction of novel configurations warn an investigation of their flow dynamic characteristics and their susceptibility to acoustic and mechanical resonance.

Additionally, the Hex pump has been relatively a short time in the market and there is not enough detailed information about its working principles, performance characteristics, potential problems, as there is for traditional reciprocating pumps. It is still unclear whether the same knowledge developed for traditional crank driven reciprocating pumps might be securely extended to the Hex pump case.

Information from conference papers seem to indicate that despite the vendor statements, the Hex pump displays relevant pressure pulsation at its discharge. Additionally, public drilling records (presented in Appendix A3) of a North Sea drilling platform with the pump installed display an excessive drilling operation duration of 244 days. The latest news (Økland, 2013) about the refurbishment of a semisubmersible rig to provide pumping and accommodation services to this platform seem to confirm that the pumping performance was somehow be related to the problem.

In the present study the Hex pump will be addressed with the more generic name "Hexagonal pump". The analysis was performed trying to maintain generality as much as possible, but when input data was required the specific model considered is the "Hex 240 pump" (a common model encountered in a few drilling rigs around the World). The work in this chapter is organized in the following manner: First a description of the general Hexagonal pump characteristics and configuration is given. Then the piston kinematics are extracted from data available in the literature, estimated numerically and discussed. A simulation is then made of the hexagonal pump valve dynamics using a 1D model from the literature programmed in MS excel and an axisymmetric 2D CFD simulation using a commercial CFD software.

Next, three cases are modeled with a 1D transient hydraulic simulator: (1) the discharge manifold and pistons arrangement of the hexagonal pump connected to a single pipeline, (2) a linear discharge manifold with the piston discharge flow rate profile of the hexagonal pump connected to a single pipeline and (3) a triplex reciprocating pump of similar capacity connected to a single pipeline.

Lastly two (2) pulsation remedy measures are evaluated and modeled for the hexagonal pump piston arrangement: orifice plate installed in the discharge manifold and pulsation dampener.

3.2 Hexagonal pump characteristics

The Hexagonal Reciprocating pump is a positive displacement axially reciprocating piston pump for heavy duty (high pressure and high rate) slurry pumping in the process and drilling industries. The six piston/cylinder units are distributed in a circular array and configured co-axially. At the end of each cylinder there is a valve block with suction and discharge valves acting along an axis perpendicular to the cylinder axis.

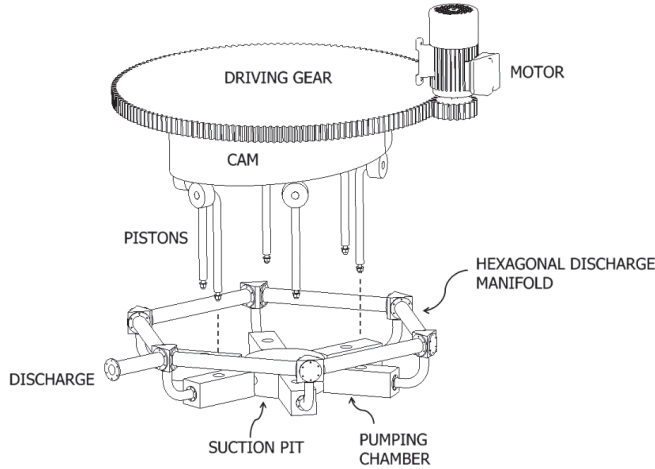


Fig. 3.1 Schematic configuration of piston assemblies and power end in the hexagonal pump

The axial piston movement is driven by a cam wheel rotating coaxially with the piston motion direction (Fig. 3.1). The profile of the constant speed rotating cam (US Patent No. 7,004,121) is designed to yield a particular piston motion resulting in a ramp-shape discharge flow rate pattern (discharge-displacement diagram) with a long rate plateau and a short build-up and decline periods. Furthermore, the compound effect of all the six cylinders, by superposition of the discharge of the individual cylinders, shifted by 60° each will give a smooth and constant compounded discharge flow rate over a pumping cycle (Fig. 3.2).

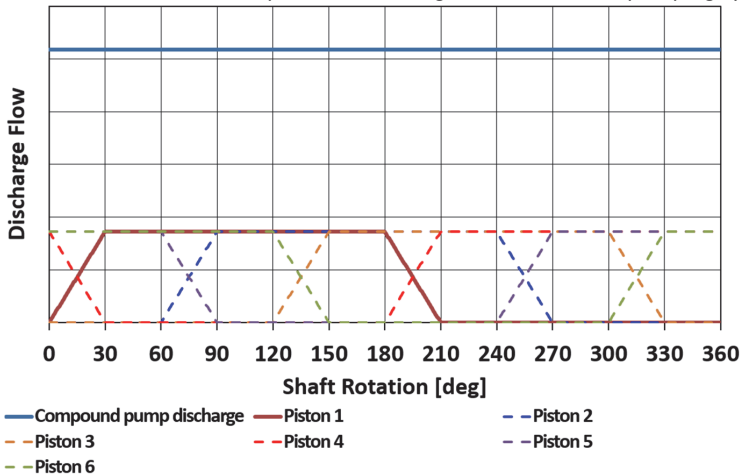


Fig. 3.2 Discharge flow of the piston used in the hexagonal manifold pump

The compound discharge of all the cylinders is aggregated into a hexagon shaped manifold with relatively small diameter and short length spools connecting the vertexes and where the cylinders discharge are positioned each at a hexagon vertex. The exit of the manifold is at one of the vertexes (Fig.

3.3). The suction manifold is a tubular shape tank in the center of the bottom part of the Hexagonal piston array.

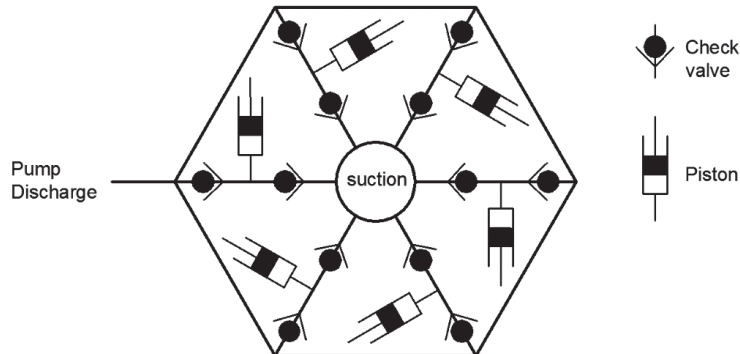


Fig. 3.3 Pump with hexagonal discharge manifold

Employing a cam wheel to drive the pistons and the hexagonal shaped manifold are new in this category of process slurry pumps. The conventional pumps for this category of application are normally three-cylinder (triplex) pumps where the cylinders are arranged in a parallel manner in a single plane. The pistons are driven by a crankshaft producing a simple harmonic piston motion (SHM or Sinus shape motion). The suction and the discharge manifold are two parallel tube shape (Fig. 3.4c) where the discharge manifold is normally equipped with a pulsation damper to smooth the rate and pressure fluctuation resulted from the reciprocating motion of the pistons.

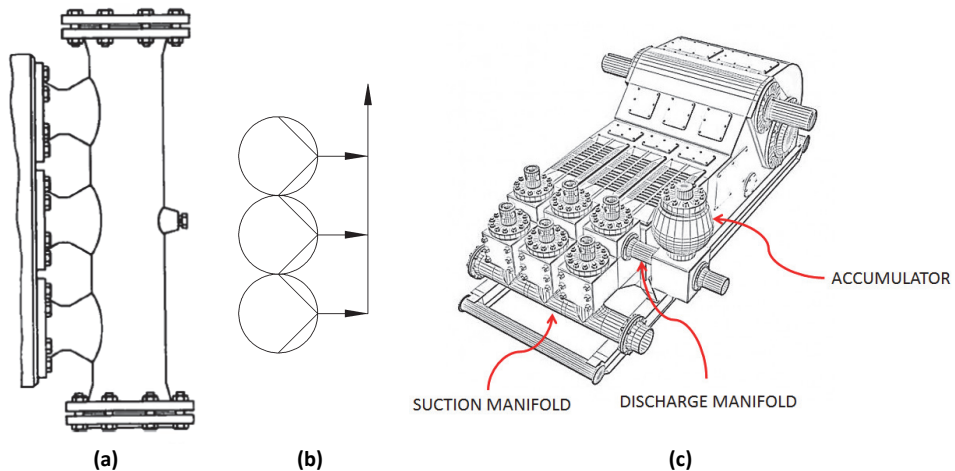


Fig. 3.4 Discharge manifold in reciprocating pumps

The theoretical smooth discharge flow rate expected from the 6 piston pump is one of the main drivers for introducing this pump design. However, prototype tests conducted as part of the qualification test (Kverneland, Kyllingstad & Moe, 2005) gave a few subtle clues that in real operation conditions, with valve action delays and with non-ideal liquids, the pump may develop severe fluctuation. While the novel kinematic of a piston motion and the compounding effect of a six cylinder pump has promised ideally a smooth discharge condition, the interface of the cylinders discharge may excite detrimental pulsation.

3.2.1 Hexagonal pump piston kinematics and comparison with a crankshaft driven piston

The ideal discharge and suction flow rate of an individual piston in a reciprocating pump can be approximated by the volume variation of the chamber (neglecting the fluid compressibility effects). As the only moving wall in the chamber is the piston head, then the flow is completely defined by the piston movement (Fig. 3.5).

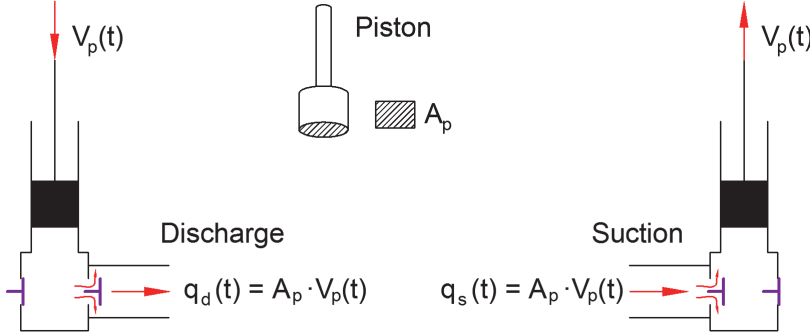


Fig. 3.5 Theoretical discharge and suction flow rate of the piston defined by the piston movement

This is a very valuable observation because, as the piston is driven by a well-defined mechanism, it is usually possible to express the piston displacement, velocity and acceleration vs power shaft rotation or vs. time. For the particular case of the Hexagonal pump the movement of the piston is determined by the patented shape Cam.

The Hexagonal pump piston displacement (x) vs shaft rotation angle (θ) curve was reconstructed by analyzing Fig. 3 of Kverneland et al. (2003). The curve was represented by piecewise functions as shown in Eq. 3.1 This function depends only on the shaft rotation angle (θ) and the piston stroke (S , Distance between lowest piston position and highest piston position).

$$x(\theta) = \left(\frac{S}{180} \right) \cdot \begin{cases} \left(\frac{1}{60} \right) \cdot \theta^2 & \text{if } 0 \leq \theta \leq 30 \\ (\theta - 15) & \text{if } 30 < \theta \leq 180 \\ \left(-\frac{\theta^2}{60} + 7 \cdot \theta - 555 \right) & \text{if } 180 < \theta \leq 210 \\ \left(-\frac{\theta^2}{40} + 10.5 \cdot \theta - 922.5 \right) & \text{if } 210 < \theta \leq 240 \\ (-1.5 \cdot \theta + 517.5) & \text{if } 240 < \theta \leq 330 \\ \left(\frac{\theta^2}{40} - 18 \cdot \theta + 3240 \right) & \text{if } 330 < \theta \leq 360 \end{cases} \quad \text{Eq. 3.1}$$

The mathematical derivative of this function with respect to time was taken to obtain the piston velocity. The procedure was repeated with the piston velocity function to obtain the piston acceleration. These piecewise functions are presented in Appendix B3. The functions depend similarly on θ , S but additionally on the shaft rotational velocity (ω).

The Hexagonal pump piston displacement, velocity and acceleration were plotted vs shaft angle in Fig. 3.6. For comparison purposes the piston displacement, velocity and acceleration of a reciprocating piston driven by a crankshaft mechanism is presented in the same figure. The plots were generated with $S=300$ mm, $\omega = 212$ rpm, and considering a connecting rod/crank length ratio of 4 for the crankshaft mechanism.

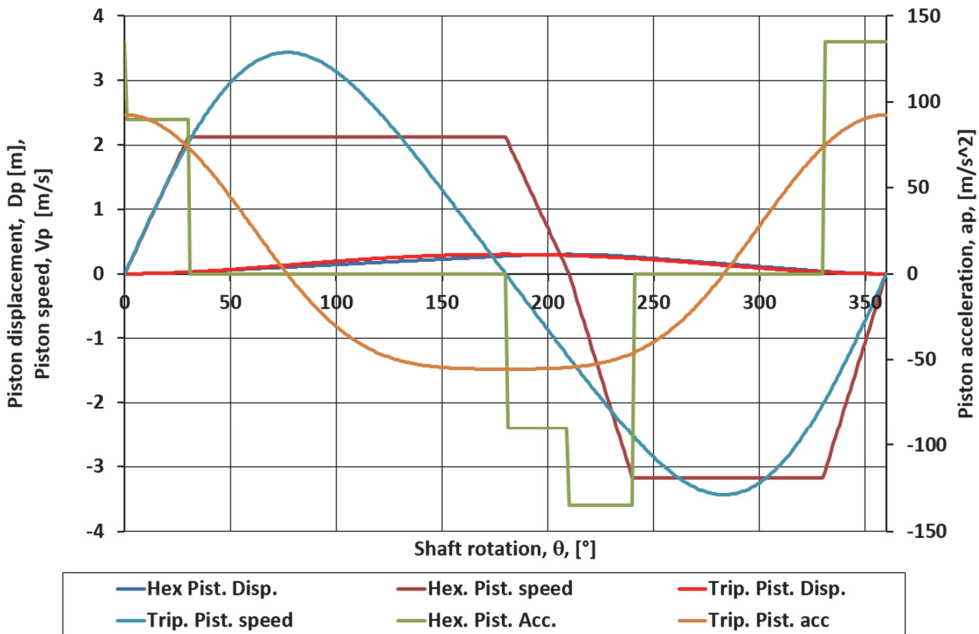


Fig. 3.6 Piston kinematics of the Hexagonal piston and crankshaft driven piston

Note that when the piston velocities are positive, it indicates that the piston is in the discharge phase. When the piston velocities are negative, it indicates that the piston is in the suction phase. The Hexagonal piston velocity curve has been designed by the pump manufacturer such as when adding the discharge of six pistons the compound rate will remain constant during a complete rotation of the power shaft. The total discharge rate is 3 times the discharge rate of an individual piston during the flat part of the curve. In the piston cycle of the Hex pump, the duration of each phase is different (in contrast with a regular Triplex pump). The duration of the discharge phase is 210° shaft rotation, and the duration of the suction phase is 150° . As the volume displaced in discharge or suction phases is the same, this indicates that the piston velocities during the suction phase (i.e. flow rates) are much higher than in the discharge phase (50 % higher for the flat part of the curve).

The maximum velocities for the crankshaft driven piston are 62% higher than for the Hexagonal pump piston in the discharge phase and 8% higher in the suction phase. However, the hexagonal piston acceleration is 64% higher at the end of the discharge phase than for the crankshaft driven piston. The Hexagonal pump piston acceleration is 145% and 47% higher at the beginning and end of the suction phase (respectively) than for the crankshaft driven piston. This represents higher dynamic forces in the piston support elements during those part of the cycle. However these are only applied for a limited part of the shaft rotation.

3.2.2 Operational valve delays in the Hexagonal pump

As it was presented in the previous section, the ideal Hexagonal pump piston flow during discharge and suction cycle is dictated by the piston speed. However, the ideal flow shape is never achieved in real operation because of valve opening and closing delays. These delays are typically expressed in terms of shaft rotation angle.

Fig. 3.7 shows a compact description of the main delays of suction and discharge valves during the piston cycle. The description of valve delays presented below are based on that figure.

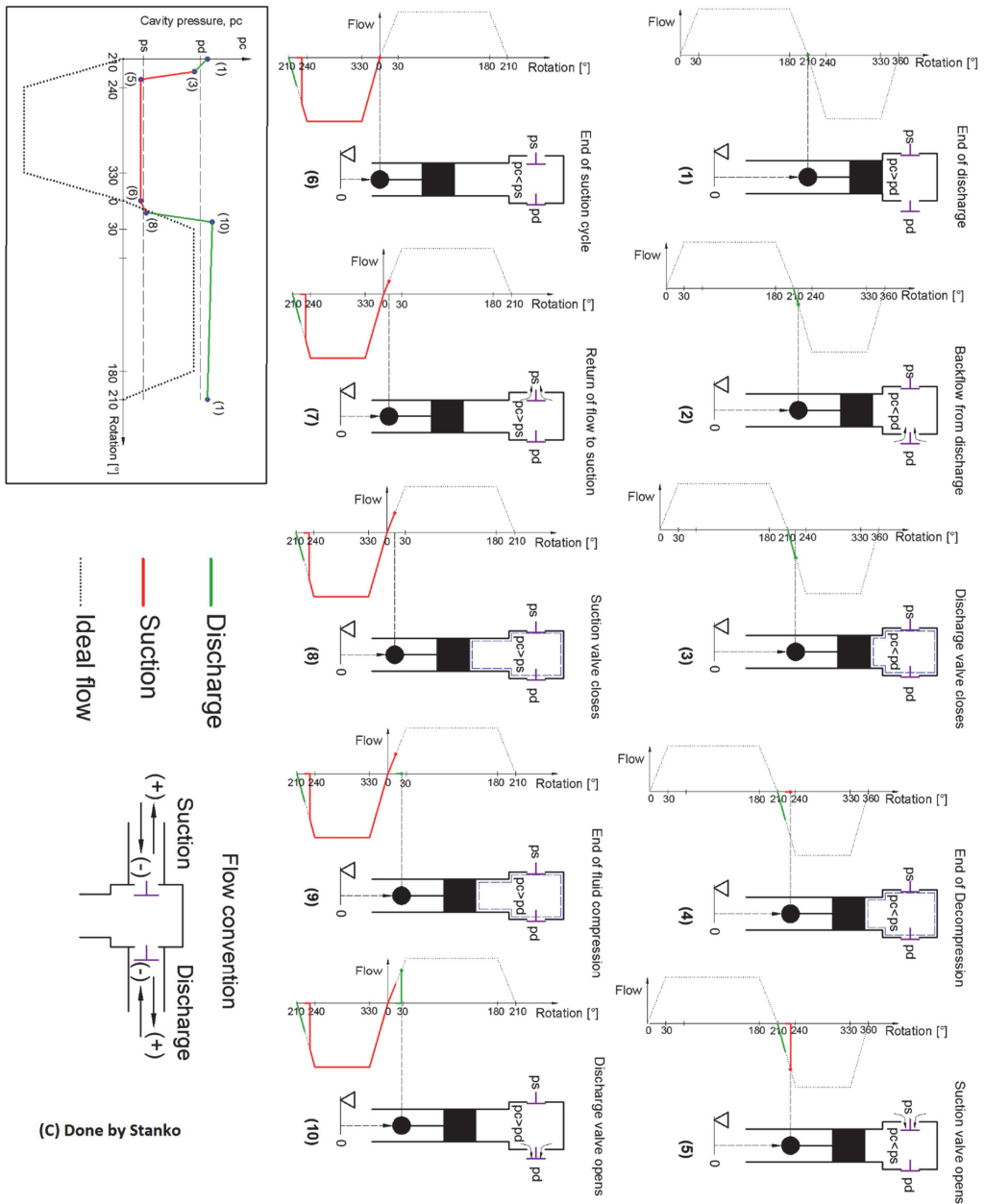


Fig. 3.7 Primary delays in the suction and discharge cycles of the Hex pump piston

1. Discharge valve closure delay (α_3)

When the piston has finished the discharge stroke (position 1) the discharge valve is open and the suction valve is closed. After it initiates the suction stroke, due to the fact that the discharge valve is still open, some of the fluid in the discharge line will flow back into the piston cavity (position 2). This backflow causes the closure of the discharge valve (Position 3).

2. Decompression delay (Suction valve opening delay) (α_4)

At this moment (Position 3) the existing fluid in the piston cavity is at a pressure similar to the pressure at the discharge. The piston continues the suction stroke until the fluid is decompressed below the pressure in the suction line (Position 4), and causes that the suction valve opens, allowing the ingress of fluid to the piston cavity (Position 5). The suction stroke then continues normally.

3. Suction valve closure delay (α_1)

After the piston has concluded the suction stroke (Position 6) the suction valve is open and the discharge valve is closed. After the discharge stroke is initiated, due to the fact that the suction valve is still open, some of the fluid in piston chamber will flow back into the suction line (Position 7). This backflow causes the closure of the suction valve (Position 8).

4. Compression delay (discharge valve opening delay) (α_2)

At this moment (Position 8) the existing fluid in the piston cavity is at a pressure similar to the pressure at the suction. The piston continues the discharge stroke until the fluid is compressed above the pressure in the discharge line (Position 9), and causes that the discharge valve opens, allowing the exit of fluid from the piston cavity (Position 10).

The actual discharge and suction flow (after all the delays are applied) are presented in Fig. 3.8.

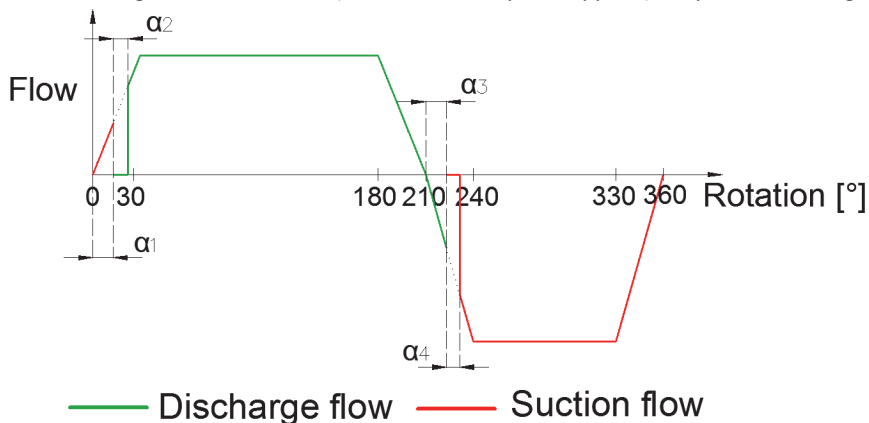


Fig. 3.8 Primary delays in the suction and discharge cycles of the Hex pump piston

It is important to note that, due to the valve delays, the discharge or suction pipeline experience a sudden flow rate step up, rather than the gradual increment of the ideal flow rate profile. Additionally the delays cause also some reverse flow to the suction and discharge piping at the end of the piston suction and discharge cycles.

The suction and discharge valve closing delays depend on the backflow to the cavity, valve lift, valve shape, the duration of the sealing sequence, shaft rotation speed, among others. As an example its estimation from a case from the literature is presented in Appendix B3.

There is an interdependence between the valve closing and valve opening (fluid compressibility) delays. This is because the fluid volume in the piston chamber to be compressed/decompressed depends very much on the starting piston position (determined by the valve closing delays).

A procedure employed to estimate these opening delays is presented In Appendix B3. Based on this procedure, Fig. 3.9 shows some discharge and valve suction opening delays versus assumed discharge/suction valve closing delays.

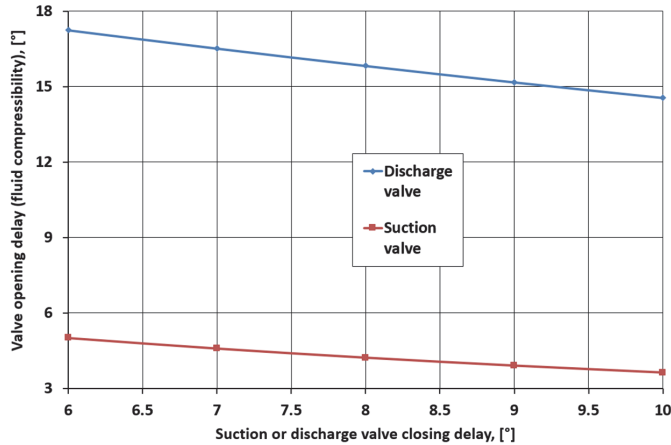


Fig. 3.9 Valve opening delay dependance with valve closing delay

It is important to note that the discharge valve opening delay is significantly higher than the suction valve opening delay. This might be due to the fact that the piston speeds in the suction phase are considerably higher (50%) than the piston speeds in the discharge phase.

3.2.3 Simulation of the hexagonal pump valve dynamics

Valves are critical components of a reciprocating pump because their opening and closing sequence defines the real discharge flow profile of the piston thus the actual flow delivery of the pump. The valves employed in the Hexagonal pump are bevel type, with two horizontal guides and a spring (Fig. 3.10). The seal has two parts: one metal to metal seal, and one metal to elastomer seal. In the figure the flow coming either from the suction piping (if it is a suction valve), or from the piston chamber (if it is a discharge valve) is depicted with $q(t)$.

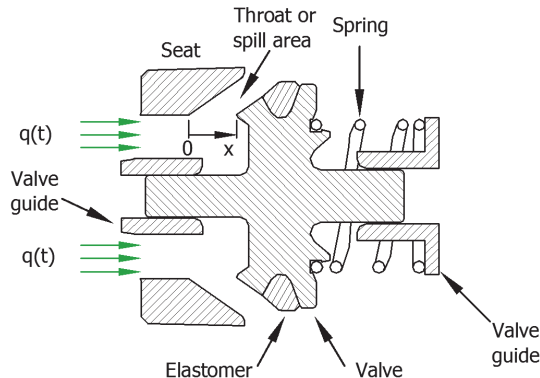
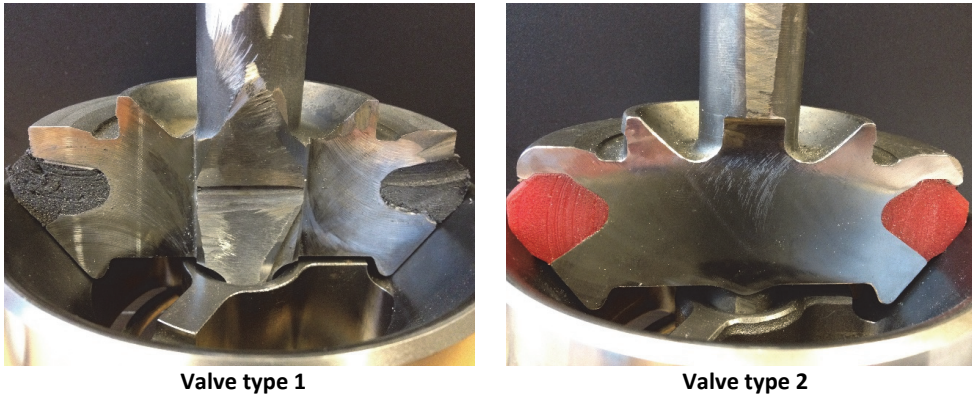


Fig. 3.10 Valve configuration in the Hexagonal pump

There are two valve models that can be used in the pump as presented in Fig. 3.11. Their geometric details are presented in Appendix C3. The main difference between the two is the size of the elastomer insert, in Valve 1 the elastomer follows the metal bevel angle while in valve 2 the elastomer protrudes out of the bevel angle. For valve type 2 the elastomer separates from the metal seat when there is a horizontal distance of 3.5 mm between the metal to metal seal.



Valve type 1
Valve type 2
Fig. 3.11 Valve types used in the Hexagonal pump

In this section the valves movement is simulated through its cycle (discharge or suction cycle) in order to detect possible operational problems.

The simulation is performed by solving the force summation equation along the valve movement axis (Eq. 3.2 where m_v is valve mass and a_v or \ddot{x}_v is valve acceleration).

$$\sum F_{VALVE} = m_v \cdot a_v = m_v \cdot \ddot{x}_v \quad \text{Eq. 3.2}$$

The different forces acting on the valve are: the force exerted by the spring (F_s), the frictional force between the valve and the guides and the fluid forces. The main challenge is to model the fluid forces as they depend on the flow rate through the valve (dictated by the piston movement) and the distance of the valve from the seat. The dependence of the forces with the valve position and velocity makes this a coupled fluid-structure problem.

In this section the valve dynamics during its cycle was modeled by using two approaches: a 1D model taken from the literature, programmed and solved using MS Excel and a 2D CFD model using a commercial simulator. Please note that these simulations have the following limitations:

- In order to simplify the simulation a starting valve position greater than zero was assumed (already separated from the seat). This assumes that when the valve opens, it opens very quickly thus the time to go from the seat to the assumed initial valve position is negligible. The velocity of this initial position is taken as zero "0".
- No experimental data was available to validate the results obtained from the simulation.

3.2.3.1 Estimating the valve closing delay from the results of the valve dynamics simulation

The valve departs at the beginning of the cycle from its seat ($x_v = 0$) and at the end of the cycle ideally should be back again in the seat. However this is not always true as it depends on the valve dynamics through the cycle. The separation between the valve and seat at the end of the cycle is what causes the closing delay discussed previously.

The valve closing delay (expressed in time units) was estimated by taking the valve position, velocity and acceleration at the end of the cycle and, assuming that the acceleration remains constant, calculating the time required for its position to be zero again. This was performed using the equation Eq. 3.3.

$$x_v = x_0 + v_{v0} \cdot t + \frac{a_{v0} \cdot t^2}{2} \quad \text{Eq. 3.3}$$

$$v_v = v_{v0} + a_{v0} \cdot t \quad \text{Eq. 3.4}$$

Where:

x_v : Valve displacement when the seating metal surfaces are in contact ($x_v = 0$)

x_0 : Valve displacement at the end of cycle (calculated from simulation)

v_v : Valve speed when the metal seating surfaces are in contact

v_{v0} : Valve speed at the end of cycle (calculated from simulation)

a_{v0} : Valve acceleration at the end of cycle (calculated from simulation)

3.2.3.2 One dimensional simulation of the valve dynamics

A transient simulation of the valve type 1 motion during the discharge and suction cycle was made using a one dimensional approximation. The procedure used was taken from the work of Henshaw (2009). The fluid force is estimated by taking into account 4 representative pressure forces acting on the valve body (p_1 , p_2 , p_3 and p_4 in Fig. 3.12). p_2 is expressed in terms of p_1 using the Bernoulli equation (p_1 equal to p_2 plus the kinematic energy) and p_3 is expressed in terms of p_4 in a similar fashion. This particular selection is made in order to make possible the simplification of terms in the force summation equation and to obtain a final equation involving only the pressure difference across the valve ($p_1 - p_4$).

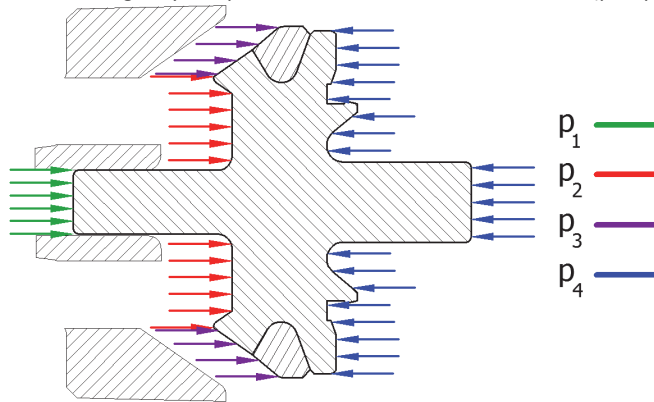


Fig. 3.12 Representative pressure forces acting on the valve body

The expression used for the pressure drop across the valve ($p_1 - p_4$) is presented in Eq. 3.5.

$$(p_1 - p_4) = \frac{\rho}{2} \cdot \left(\frac{V_3}{c} \right)^2 \quad \text{Eq. 3.5}$$

Where:

V_3 Fluid velocity in the throat area (taken at the place where the area is narrowest)

c Valve coefficient (value 1.3 estimated from a 3D CFD simulation of the valve geometry).

Some other values used as an input for the simulation are below:

- Valve dimensions as presented in the Appendix C3 corresponding to valve type 1.
- Fluid density 1350 kg/m³
- Spring data: Precompression :2.7 mm, Stiffness: 15784 N/m
- The piston flow rate curve vs time was built with the following hexagonal pump data: piston diameter 4.5 inch, speed 125 RPM, stroke 0.3 m.
- The friction force was calculated assuming a dynamic friction coefficient of: 0.16.
- Valve discharge pressure: 300 bara, valve suction pressure: 4 bara.
- Initial valve conditions: valve displacement: 1 mm, valve velocity: 0 m/s.

The resulting equation is a second order differential equation that is solved numerically in MS Excel using a 4th order Runge Kutta. The total number of time steps employed were 1000. The procedure used for the simulation was iterative and consisted on the following steps:

1. Assume a suction valve closing delay
2. Calculate the discharge valve opening delay from the fluid compressibility (using the value of the suction valve closing delay)

3. Perform the simulation of the discharge valve movement
4. Calculate the discharge valve closing delay by the procedure mentioned earlier (Eq. 3.3)
5. Calculate the suction valve opening delay from the fluid compressibility (using the value of the discharge valve closing delay)
6. Perform a simulation of the suction valve movement
7. Calculate the suction valve closing delay by the procedure mentioned earlier (Eq. 3.6)
8. Check if the calculated suction valve closing delay matches the assumed value in step 1, if not repeat the procedure.

Convergence was achieved after two iterations.

Discharge valve simulation results

In Fig. 3.13 the discharge valve displacement and piston chamber outflow are shown versus time during the discharge cycle. The valve lift (displacement) follows the same curve form of the flow, which is consistent with results existing in the literature for triplex pumps (Karassik et al 2008). At the initial part of the cycle (0.05-0.08 s) the valve oscillates. It was found that this oscillation depends on the initial valve separation from the seat employed for the simulation. However the rest of the curve was independent from the initial value of the valve separation from the seat.

Is it important to note that the valve position is constant for a part of the valve cycle (when the piston flow rate is constant). This is an equilibrium position where the fluid forces and the spring forces are equal. The valve displacement reaches a maximum value of 7.4 mm. By the end of the cycle, the valve separation from the seat is 1.3 mm. The discharge valve closure delay calculated is 6.5°. This value is similar to the value calculated from the paper of Kyllingstad & Nessjøen (2011).

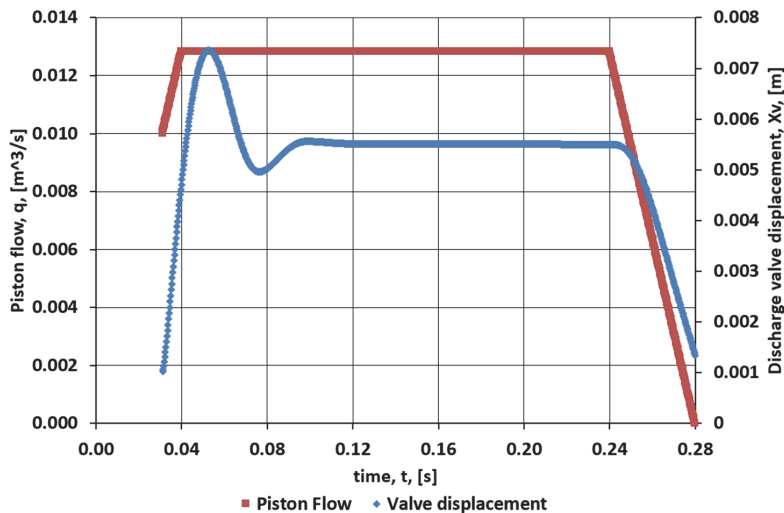


Fig. 3.13 Discharge valve displacement and flow rate from piston chamber.

In Fig. 3.14 the pressure drop across the discharge valve is shown versus time. During most part of the cycle, values are below 1 bar, meaning that the piston chamber pressure will be very close to the discharge pressure. However, at the initial part of the cycle a higher pressure drop is required for the fluid to pass through the valve.

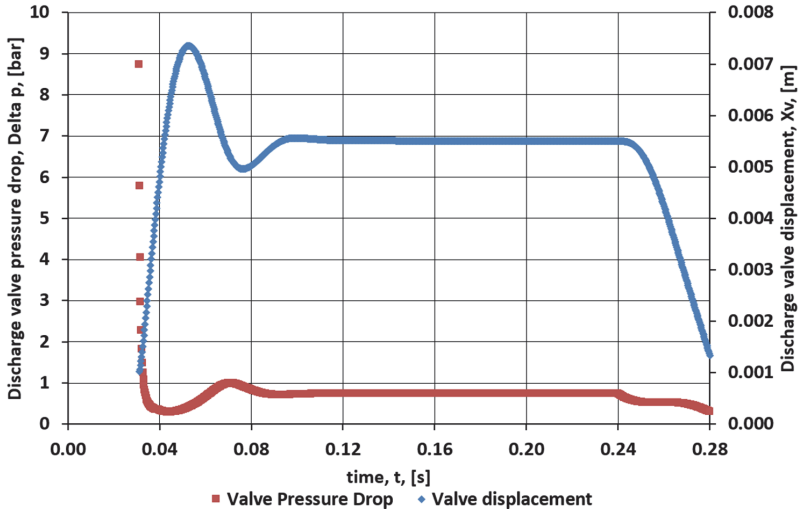


Fig. 3.14 Simulated discharge valve displacement and valve pressure drop

Suction valve simulation results

In Fig. 3.15 the suction valve displacement and suction piston inflow are shown versus time during the suction cycle. The maximum valve displacement is 7.8 mm. By the end of the cycle, valve separation from the seat is 1.7 mm which corresponds to a valve closing delay of 6.2°.

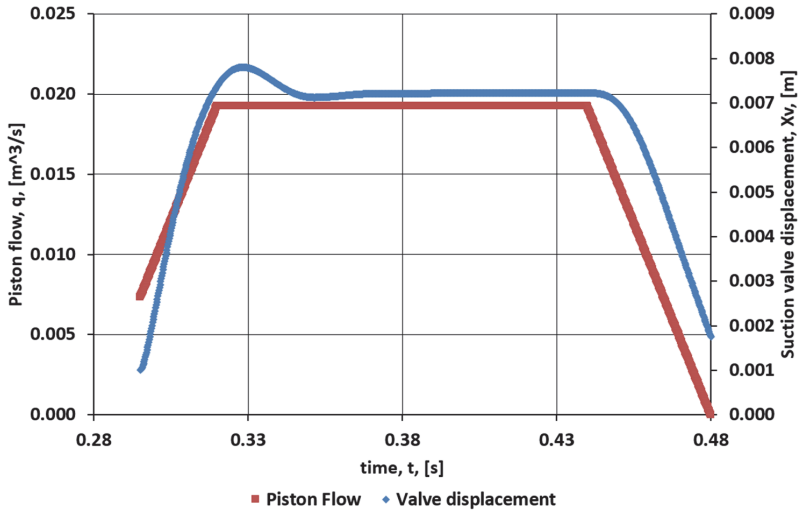


Fig. 3.15 Simulated suction valve displacement and inflow to piston chamber versus time

In Fig. 3.16 the suction valve pressure drop is shown versus time. During most part of the cycle, values are below 1 bar. However, at the initial part of the cycle a higher pressure drop is required, which is usually not available at the suction conditions (4 bara). This is a normal operating condition (Collier 1983) where the fluid separates from the piston head, it is vaporized and then turns back into liquid thus hitting the piston head (knocking).

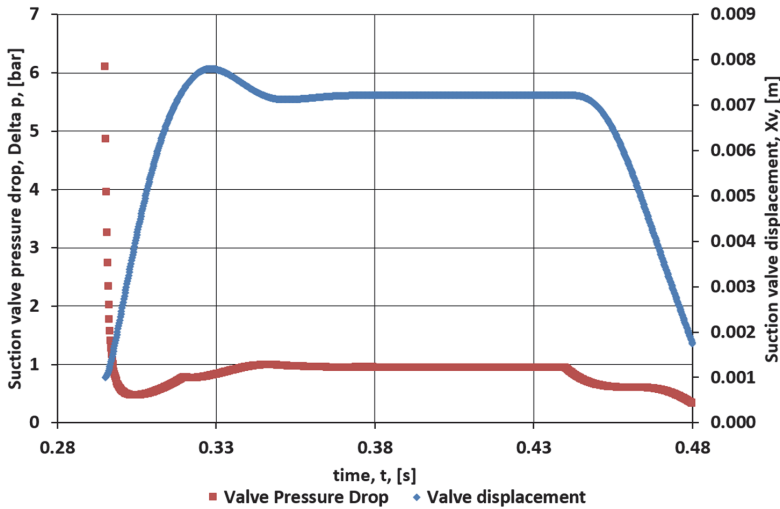


Fig. 3.16 Simulated suction valve pressure drop and displacement vs time.

Suction and Discharge valve closing delays dependence with pump shaft rotation

The 1D simulation was repeated for 3 more different pump shaft rotation speeds (95, 160 and 212). The valve closing delays were computed and the results are shown in Fig. 3.17. The valve closing delays increase as the pump shaft rotation speed increases.

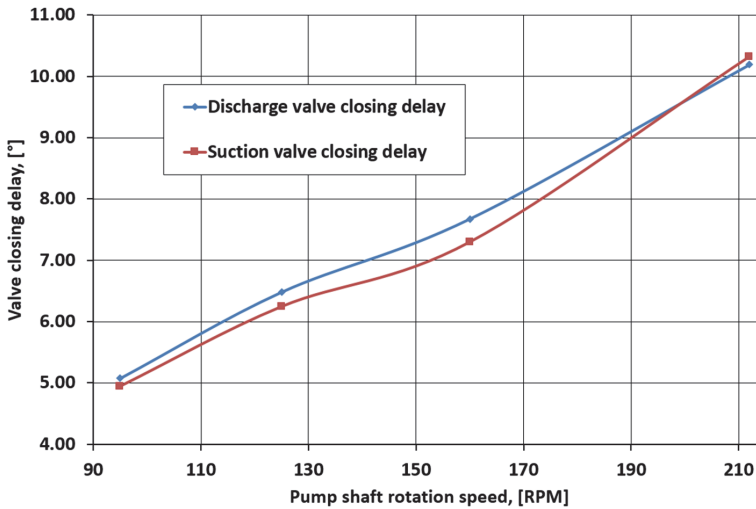


Fig. 3.17 Valve closing delay vs pump shaft rotation speed - 1D simulation results

The sum of the valve delays occurring in the discharge cycle (suction valve closing + discharge valve opening) and suction cycle (discharge valve closing + suction valve opening) are plotted vs pump shaft rotation speed in Fig. 3.18. Please note that the total delay increase with speed is not as steep as for the valve closing delays (Fig. 3.17). This is due to the fact that fluid compressibility delays diminish as the valve closing delay increases (as seen in Fig. 3.9).

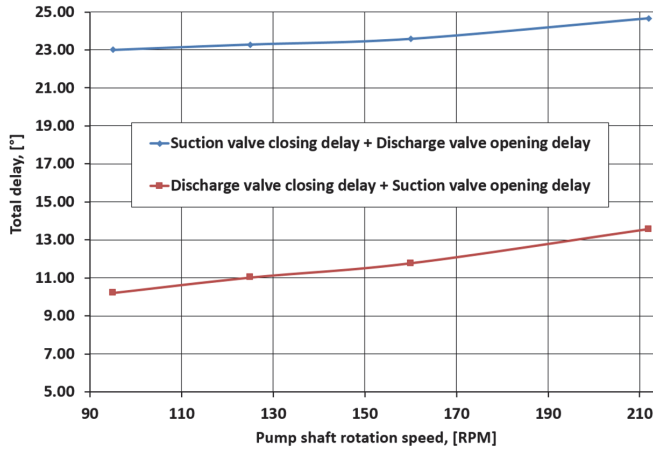


Fig. 3.18 Total discharge and suction delays vs pump shaft rotation speed

3.2.3.3 Suggestion for improvement of the 1D model

As a suggestion for improvement of the 1D modeling presented in the previous section it is proposed to use an axisymmetric 2D CFD model to estimate the axial fluid force function acting on the valve that depends on the flow rate through the valve (q) and the valve separation from the seat (x). This eliminates the assumptions taken by Henshaw (2009) about representative pressure forces acting in different valve locations thus yielding a more robust modeling.

The axial fluid force function was determined using a CFD model of the valve type 2 geometry. Eight (8) valve geometries were meshed corresponding to 8 different valve openings (4, 5, 6, 7, 9, 11, 13 and 15 mm) and for each one of these geometries 11 rates were simulated (a total of 88 CFD simulations). The fluid taken for the simulation has a density of 1350 kg/m^3 and a viscosity of $0.021 \text{ Pa} \cdot \text{s}$. Results of the simulations are shown in Fig. 3.19.

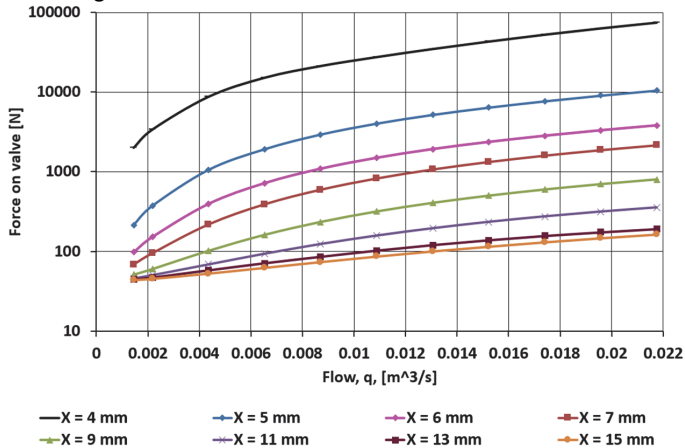


Fig. 3.19 Fluid force function vs valve flow rate for different valve openings

Borregales et al (2014) built a function (depending on q and x) to represent this set of data using a genetic algorithm. Unfortunately the 1D simulation was not performed employing this fluid force function. The simulated pressure drop across the valve is presented in Fig. 3.20. It is important to note that the shape of the pressure drop curve is very similar to the fluid force curve for small openings (4,5,6,7 mm) and high flow rates ($>0.004 \text{ m}^3/\text{s}$). However the shape of the curves is different for bigger valve openings.

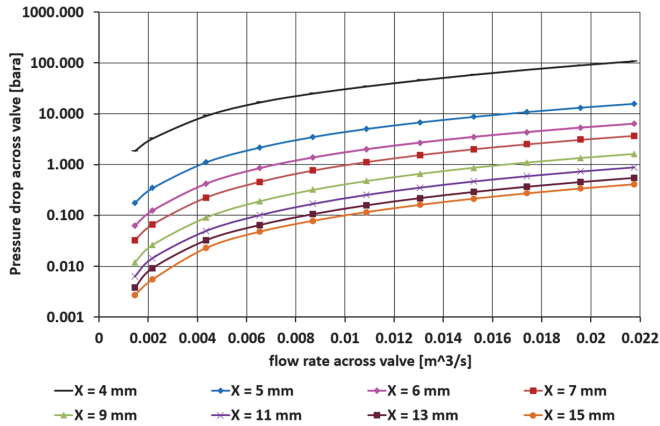


Fig. 3.20 Pressure drop across the valve vs flow rate for different valve openings

3.2.3.4 Two dimensional axisymmetric CFD model simulation of the discharge valve dynamics

A fluid-structure coupled simulation of the discharge valve type 2 was performed using a CFD model. The model was setup, solved and results were visualized in the commercial software Ansys CFX. The details of the simulation are presented in Appendix D3.

The CFD simulation employed as inlet boundary condition the flow rate coming from the piston (for a shaft rotation speed of 125 RPM) and as outlet boundary condition a constant discharge pressure of 300 bara. The mesh employed had a fixed number of elements that were deformed as the valve surface moved. The simulation was made assuming a suction valve closing delay of 5° and a discharge valve opening delay of 18°.

It is important to note that for type 2 valve when the metal to metal seal separates, there is still contact between the elastomer and the seat. The elastomer separates when there is a distance of 3.5 mm between the metal to metal seal. For that reason the starting valve metal to metal seal separation from the seat was 5 mm for the simulation. This was done in order to avoid excessive mesh deformation during the simulation.

In Fig. 3.21 the discharge valve displacement and piston chamber outflow are shown versus time during the discharge cycle. The same valve oscillation is seen than in the 1D simulation. The discharge valve separation from the seat (metal to metal seal) at the end of the cycle was 4.2 mm (0.7 mm axial distance between elastomer and metal).

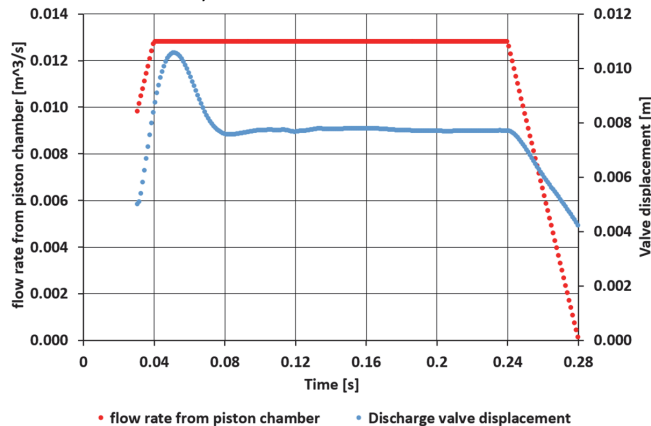


Fig. 3.21 Simulated discharge valve displacement versus time

For referential purposes the discharge valve displacement and speed results versus time of the CFD method and the 1D method are compared in Fig. 3.22. Please note that the two cases are not exactly comparable because the valve geometry is slightly different.

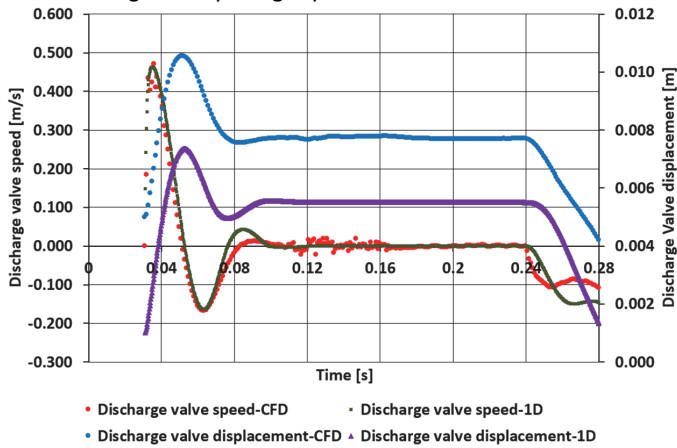


Fig. 3.22 Discharge valve simulation results between CFD model and a 1D approximation

The discharge valve displacement behavior vs time is very similar between the two simulations, however the equilibrium position (when the piston flow rate is constant) value is different between them. This might be due to two factors:

- The two valve types have slightly different geometries that give a different fluid drag force acting on the valves
- The 1D model is underpredicting the fluid forces acting on the valve.

However the computed valve speed vs time is very similar between the two cases.

3.3 Transient hydraulic 1D simulation

The objective of this section is to analyze the hydraulic performance of the discharge of the hexagonal pump using a 1D transient hydraulic simulator. This section consists of two parts:

- Simulation of the discharge characteristics of the Hex pump and comparison with the characteristics of a Triplex crankshaft driven pump and a six cylinder cam driven pump, both with linear discharge manifold. A simplified acoustic resonance analysis was made for these systems and it is presented in Appendix G3.
- Simulating the pulsation arresting effect of two pulsation reducing measures, a single orifice plat installed on one of the manifold spools and a volumetric dampener conventionally used with triplex pumps.

3.3.1 Setting up the simulation cases

The simulated system consists of a pump with a 40 m long horizontal steep pipe tied-in to the discharge side of the pump and with a constant pressure of 300 bara at the exit of the pipe. Three cases, each with different pump, are simulated (Fig. 3.23). The cases are selected as to distinguish between the effects of pump configuration, number of pistons, and the shape of the discharge manifold. In all cases, the pumping rate is 38.5 l/s (Pump shaft speed 125 RPM):

- Conventional triplex pump-with sine shape, simple harmonic piston motion (crankshaft drive)and with linear manifold
- Six piston hexagonally arranged pump with ramp type piston motion (rotating cam drive) and with linear discharge manifold
- Hexagonal pump with ramp type piston motion and with hexagonal discharge manifold

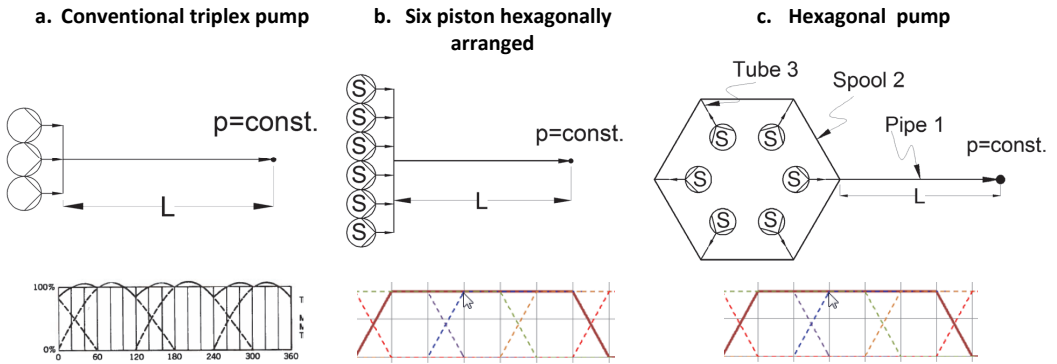


Fig. 3.23 Cases simulated using transient hydraulics

The relevant fluid and simulated pipe section properties are listed in Table 3.1 and the dimensions of the pipe section and the short spools of the hexagonal manifold are listed in Table 3.2.

Table 3.1 Fluid properties and pipe properties and characteristics

Fluid properties		Pipe properties	
Fluid density [kg/m ³]	1350	Elasticity module [MPa]	203282.4
Fluid viscosity [Pa s]	21e-3	Poisson ratio	0.3
Bulk elasticity module [bar]	20759.4	Pipe support	Anchored upstream
Constitutive fluid model	Newtonian		

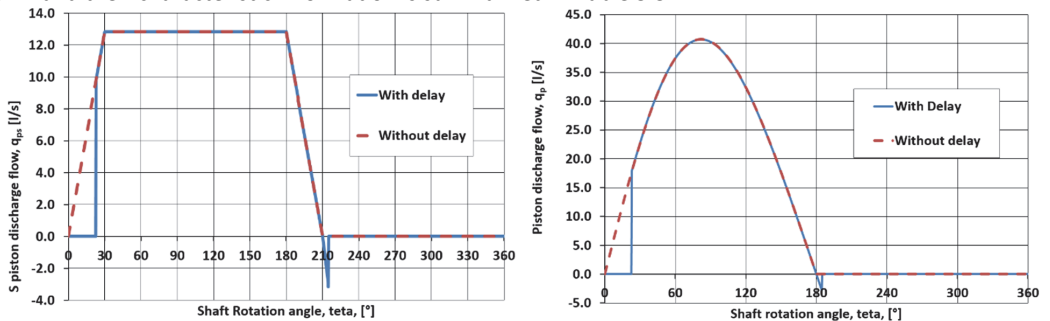
Table 3.2 Piping geometrical characteristics

	Pipe 1	Spool 2	Tube 3
Length [m]	40.0	1.2	0.3
Inner diameter [mm]	103.2	103.2	80.1
Pipe thickness [mm]	19.1	19.1	17.1

The simulations address two piston kinematics and their associated discharge characteristics

- Ramp shape- Generated by rotating disk-shaped cam
- Sinusoidal profile- generated by crankshaft power end

The real ramp and sinusoidal discharge flow profiles have a distortion or cut out from the ideal curves. These distorted profiles are input to the dynamic flow simulation. The distortions, or cut-outs, as mentioned earlier are caused by fluid compressibility and by the valve closing delay. The characteristics of the two considered discharge profiles with and without their considered delays are illustrated in Fig. 3.24 and their characteristic information is summarized in Table 3.3.



(a) Ramp shape discharge

(b) Sinusoidal shape discharge

Fig. 3.24 Ideal and real piston discharge for: (a) Ramp profile, (b) Sinusoidal profile

Table 3.3 General data for the calculation of the sinusoidal and Ramp piston discharge

Ramp discharge profile		Sinusoidal discharge profile	
Maximum flow [l/s]	12.826	Piston diameter [mm]	148.5
Pump speed [RPM]	125	Stroke length [mm]	355.6
Fluid compressibility delay [°]	18	Rod length [mm]	1244.6
Suction valve closing delay [°]	5	Pump speed [RPM]	125
Discharge valve closing delay [°]	5	Fluid compressibility delay [°]	18
		Suction valve closing delay [°]	5
		Discharge valve closing delay [°]	5

3.3.2 Setup of the simulations

3.3.2.1 The simulator

The simulations in this study were conducted by a simulator for transient flow in a pipe of a homogenous and slightly compressible fluid. It is based on solving the partial differential equations of the mass and momentum conservation taking into account the fluid and pipe elasticity. The differential equations are converted to ordinary differential equations using the method of characteristics, and these are discretized using finite differences on temporal-spatial grid, given two finite difference formulas each with a characteristic direction where the formula is valid.

The development of the characteristic formulas and the strategy for solving them with the boundary conditions are given in Appendix E3. The appendix comments also on the approach to determine a time step for the solution. Time step solution requires special considerations as the pipe and the manifold tubes and spools constitute a piping network with a wide range of pipe length elements, where all of them need to use the same time step in the solution.

The friction factors used in the finite different formulas are the conventional and widely used steady state approximation: Blasius equation for laminar flow and Colebrook correlation for turbulent flow.

All the involved pipes in the network are considered thick walled for their elastic response to inner pressure. The simulated pipe support for each pipe or spool segment is simplified by an upstream anchor (pipe end is fixed in all 3 dimensions).

3.3.2.2 The boundary conditions

The boundary conditions used in the solution of the three simulation cases are time-dependent flow at the pump discharge end of the system and a constant pressure at the exit of the 40 m pipe section. Cases a) and b) have a single point flow boundary conditions at the outlet of the linear shaped and relatively large volume discharge manifold. In case c) there are six point flow boundary conditions representing the individual pistons discharge. This includes the hexagonal discharge manifold in the model.

The input to the simulator is a two column table listing a time series with its corresponding flow for the total time duration of the simulation.

The time dependent flow at the boundary for case a) is calculated by adding three piston discharge rates with an angle shift of 120° between them. The individual discharge of a sinusoidal piston is obtained from the piston velocity expression derived from the time dependent motion of the crankshaft mechanism.

The time dependent flow at the boundary for case b) is calculated by adding six piston discharge rates with an angle shift of 60° between them. The individual piston discharge is calculated with data listed in table 3.

The time dependent flows at the boundary for case c) are calculated by phase shifting 60° the discharge of individual piston by 60°, 120°, 180°, 240° and 300°.

The constant pressure boundary at the exit from the 40 m pipe represents a hydraulic element such as a reservoir, tank or a position in the system where the pressure pulsations caused by the pump have dropped to a negligible level. The boundary conditions are summarized in Fig. 3.25.

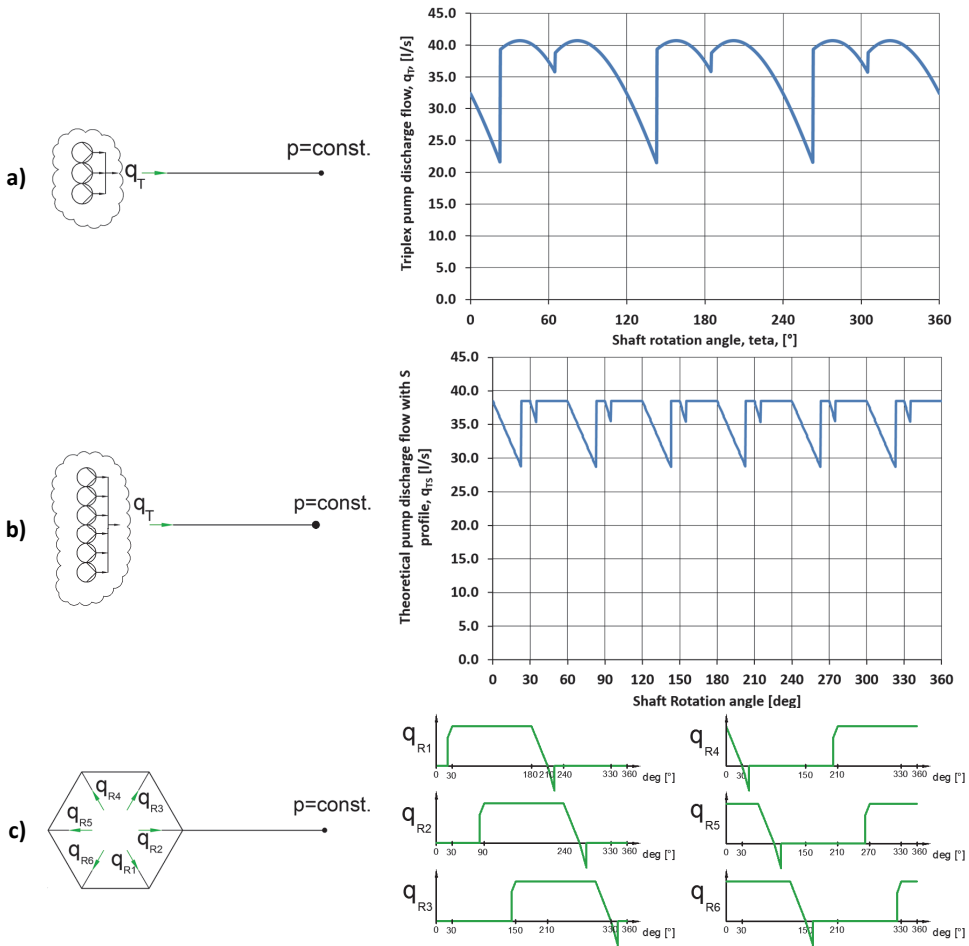


Fig. 3.25 Time dependent flow boundary conditions for cases a, b and c.

The transient simulations were carried out departing from a steady state solution. The steady state solution for each particular case was calculated by imposing the flow values corresponding to time = 0 s. The transient simulation was performed for a total time of 60 s, and with a time step of 2.49e-4 s.

3.3.3 Results

The transient results of the simulations were inspected visually to discard the stabilization period between the steady state solution and the “stable transient”. The “stable transient” is defined when there is qualitative and quantitative repetition of the variables after a time period.

The range selected for the post processing analysis was from 30 to 30.48 s (one period of the pump shaft rotation). Fig. 3.26 below shows the discharge pressure and flow for cases a, b, c and the maximum, minimum, average and peak to peak values of these two variables.

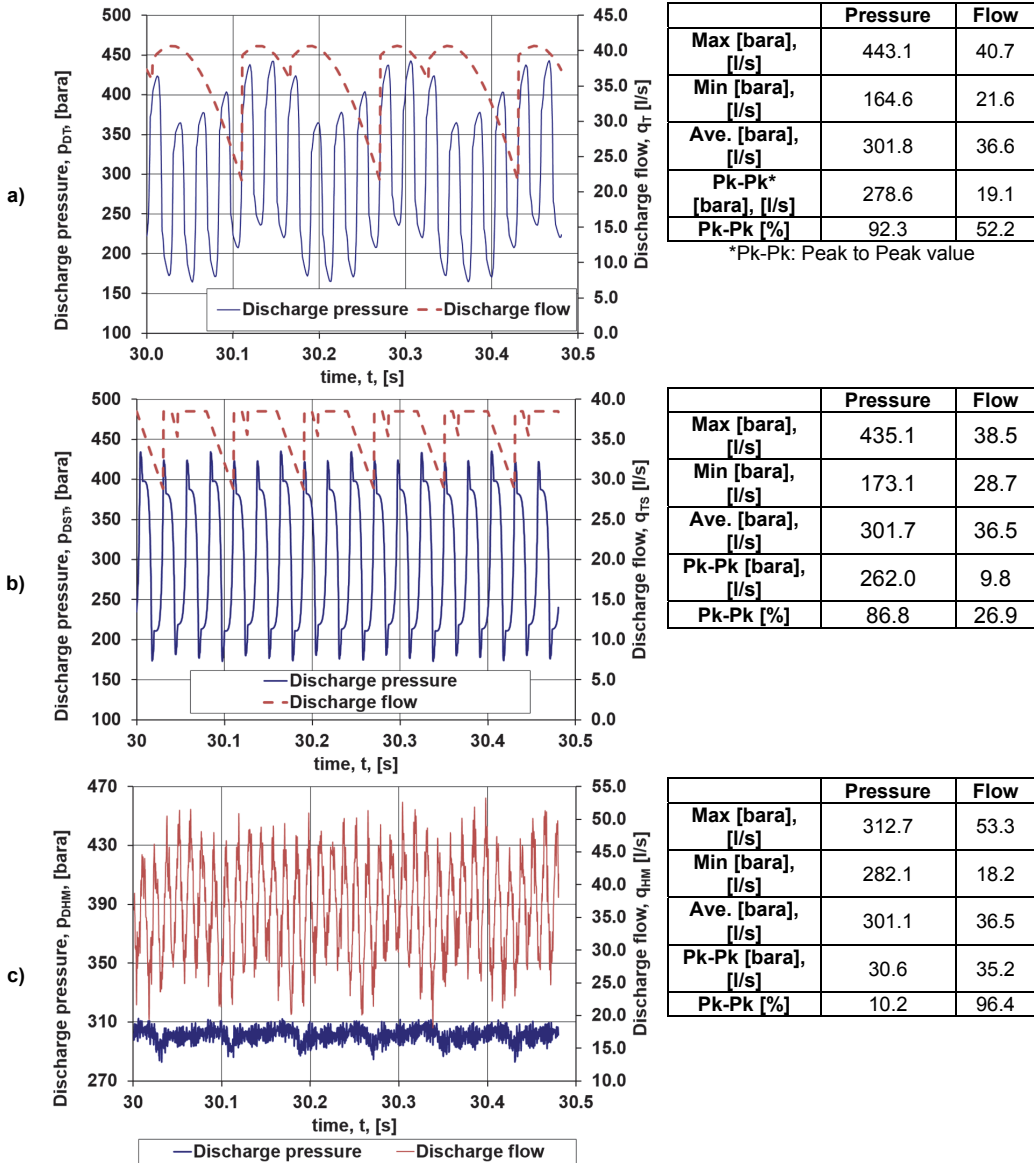


Fig. 3.26 Calculated discharge pressure and flow for one pump period ($T = 0.48$ s) for cases a, b and c.

The triplex pump (case a) exhibits the most severe discharge pressure fluctuation. The peak to peak values of pressure are 92.3% of the average discharge pressure. The maximum flow corresponds to 11% above the mean and the minimum flow corresponds to 41% below the mean.

The pressure fluctuations of case b have a similar behavior to case a, however, the discharge flow fluctuation band is significantly less than of the triplex pump (max 5% above mean and minimum 21% below mean).

When comparing the flow discharges of cases b and c it is important to note that the presence of the hexagonal manifold creates a discharge flow pattern completely different from the superposition of the individual piston flow discharges. The hexagonal manifold configuration exhibits the most severe

discharge flow fluctuation (maximum 46% above mean and minimum 50% below mean). This flow fluctuation occurs several times within a cycle, at a dominating frequency of 75 Hz, far superior than the theoretical superposition case.

In spite of the flow fluctuations, the pressure fluctuations of case c are the less severe, with a peak to peak value of 10% of the average pressure. The magnitude of the pressure fluctuations are comparable with the values reported in Fig. 2 of the paper by Kyllingstad & Nessjøen. (2011).

FFT analysis of the pressure results

The discharge pressures of the three cases were processed with Fast Fourier Transform analysis. The time period taken for the analysis was from 30-34 s of data. The calculated frequency spectra are presented in Fig. 3.27 below.

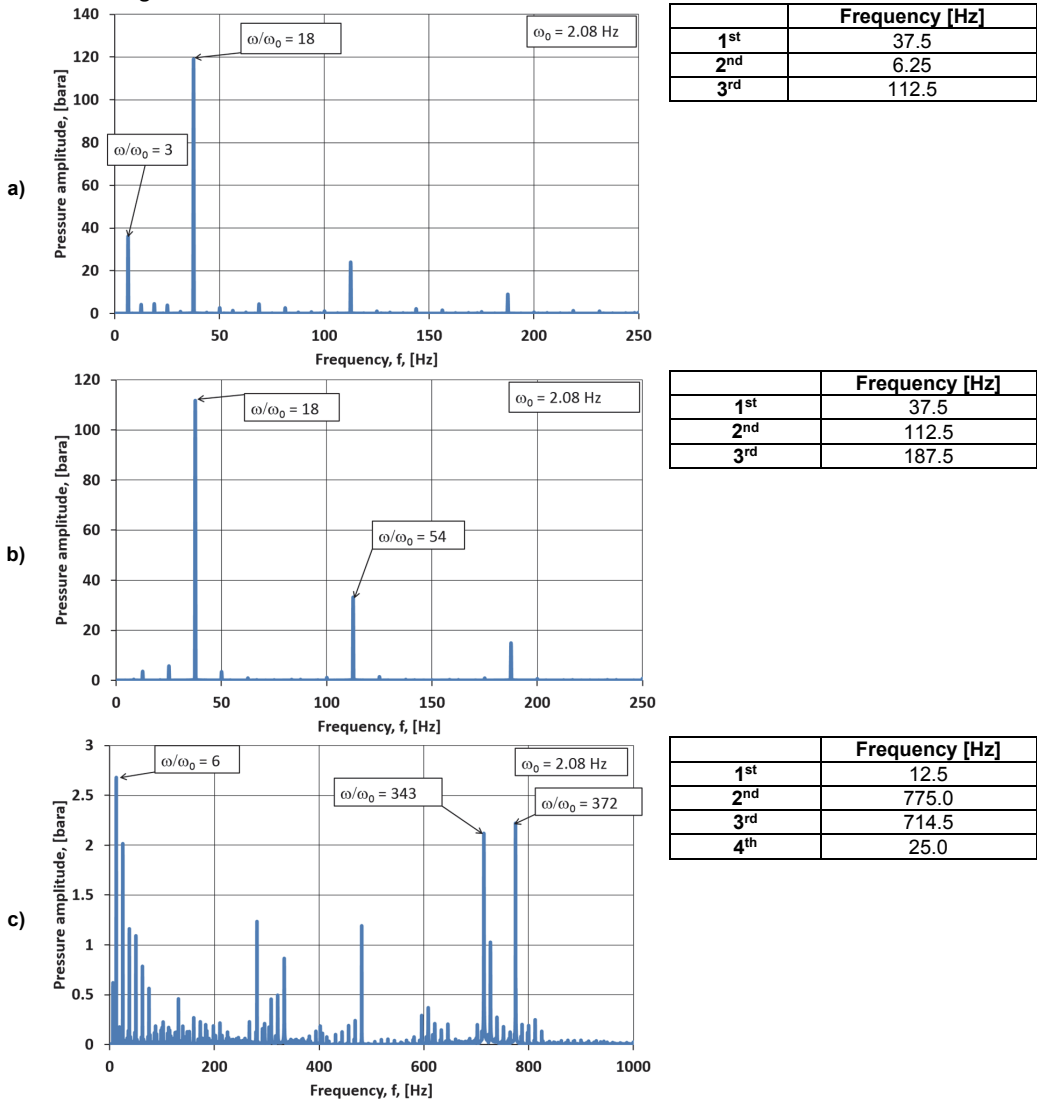


Fig. 3.27 Dominant frequencies in the discharge pressure signal for cases a, b and c.

For cases a) and b) there is one clear frequency that contributes most to the pressure fluctuation signal. The value of these frequencies is 37.5 Hz which corresponds, as shown in Appendix G3, to the 6th (case a) and 3rd (case b) harmonics of the pumps base frequencies.

The frequency spectrum of case c) show several frequencies that make an important contribution to the pressure fluctuation signal. The predominant frequency (with the biggest amplitude) corresponds to the base frequency of the pump (12.5 Hz).

The range of frequencies with relevant amplitude is broader than in cases a) and b), reaching frequencies of 775.0 Hz and 714.5 Hz. These frequencies might be a consequence of the pipe connectors between the piston discharges and the vertexes of the hexagonal manifold.

3.3.3.1 Pressure and flow inside the hexagonal manifold

The results of the simulation of case c) indicate that there is alternating flow in the hexagonal manifold sectors between the discharge points of the individual cylinders (Fig. 3.28).

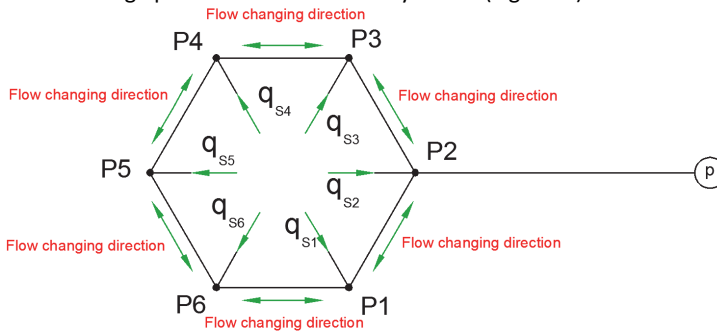


Fig. 3.28 Diagram indicating the location of alternating flow in the hexagonal manifold.

The alternating flow in the hexagonal ring is not symmetric though the cylinders discharge points are evenly distributed. This is due to the single exit point from the manifold ring that makes the entire flow asymmetric and the sectors flow alternating. As shown in Fig. 3.29, the most severe changes (alternating intensity) in the flow direction occurs in P5 of the Hex ring, located opposite to the manifold discharge point. Severity of flow direction changes diminish when approaching the hexagonal manifold discharge point.

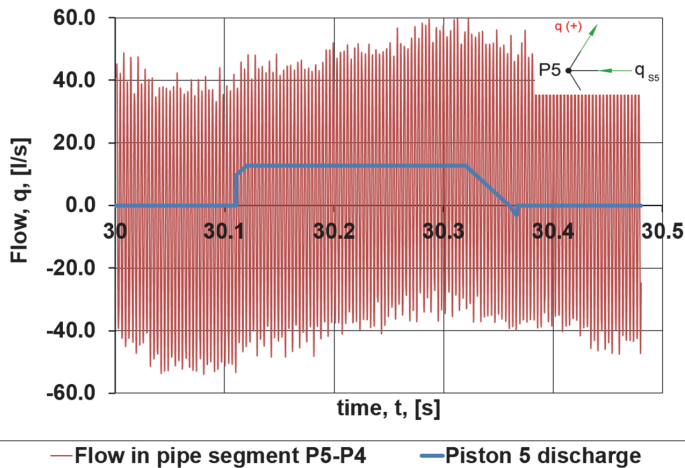


Fig. 3.29 Reciprocating flow in section P5-P4 of the hexagonal manifold.

The maximum and minimum pressures recorded during the entire simulation time, along the hex ring path P5-P4-P3-P2 are shown in Fig. 3.30. The other branch of the Hexagonal ring (P5-P6-P1-P2) showed a similar behavior. The points of the hexagonal ring with the biggest pressure fluctuation (approx. 200 bar) are located close to P4, P3 and their analogous P6 and P1. The biggest flow fluctuations are the points where the pressure fluctuation is minimum, i.e. P5, between P4 and P3, between P6 and P1 and at the discharge.

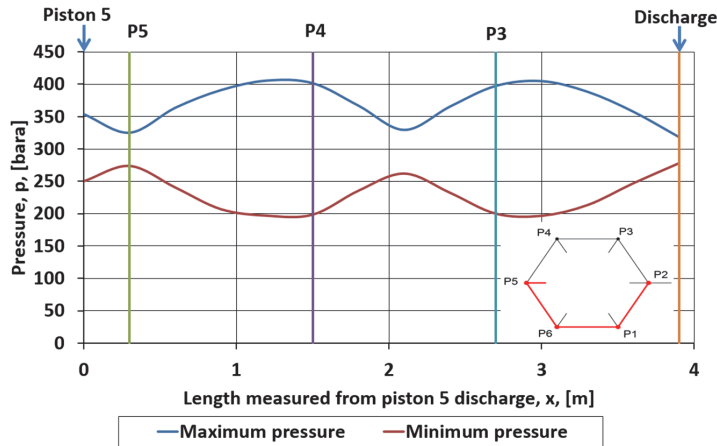


Fig. 3.30 Maximum and minimum pressure values recorded during the simulation along a branch of the hexagonal discharge manifold.

The maximum and minimum pressure recorded during the entire simulation time, along the discharge piping is shown in Fig. 3.31. The biggest pressure fluctuation does not occur in the pump discharge but at approximately at 4 m, 12 m, 20 m, 28 m and 36 m from the discharge. The graph resembles the fifth mode resonance mode of an open-open end pipe (74.84 Hz) (as per Appendix F3).

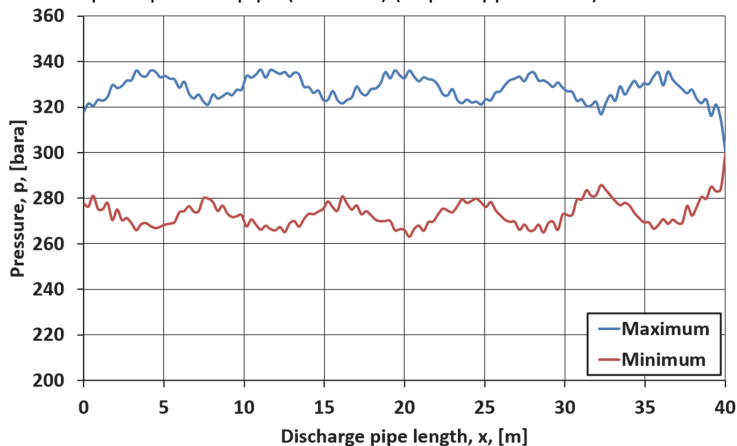


Fig. 3.31 Maximum and minimum pressure values recorded during the simulation along the discharge piping.

The simulated pressures of the hexagonal manifold points (P1, P3, P4, P5, P6) were processed using FFT analysis for the time range between 30-34 s. Points P1, P3, P4 and P6 showed an identical behavior as the one shown in Fig. 3.32. The spectra of the pressure signal of point P5 was similar to the one calculated for the pump discharge.

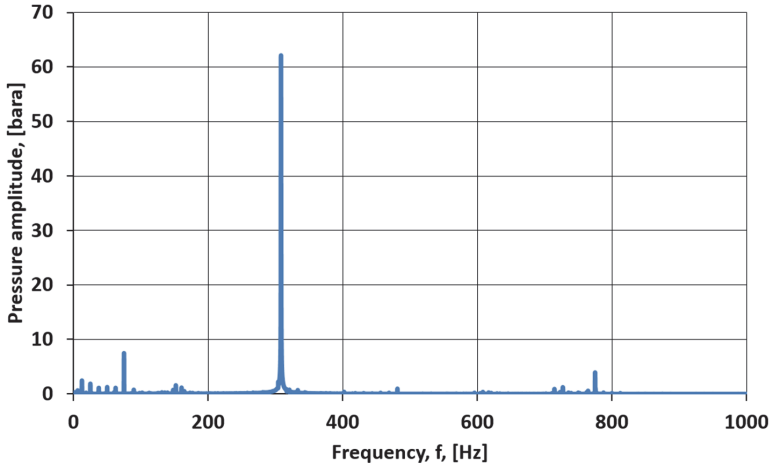


Fig. 3.32 Dominant frequencies in the pressure signal of the hexagonal manifold point P6.

The existence of a common strong frequency in the pressure signals of points inside the hexagonal manifold could indicate the presence of a high frequency pressure wave that propagates through the hexagonal manifold. This phenomenon could be caused by the circular continuous fluid structure of the hexagonal manifold with low frictional energy dissipation.

3.3.4 Pulsation remediation measures

Two measures against pressure pulsation were employed and evaluated for the hexagonal pump: orifice plate and a gas accumulator. The cases simulated were: 1. hexagonal pump with orifice plate and 2. Hexagonal pump with orifice plate and gas accumulator

3.3.4.1 Case 1: Hexagonal pump with orifice plate

The orifice plate was placed at 15 cm from P5, on the pipe section that joins P5 and P4 (Fig. 3.33). This location was chosen because it exhibits maximum flow fluctuation, thus maximizing the dissipative effect of the orifice. The orifice was modeled with a loss coefficient with a value of 577 (approx. 20 bar pressure loss for a flow of 20 l/s through the orifice).

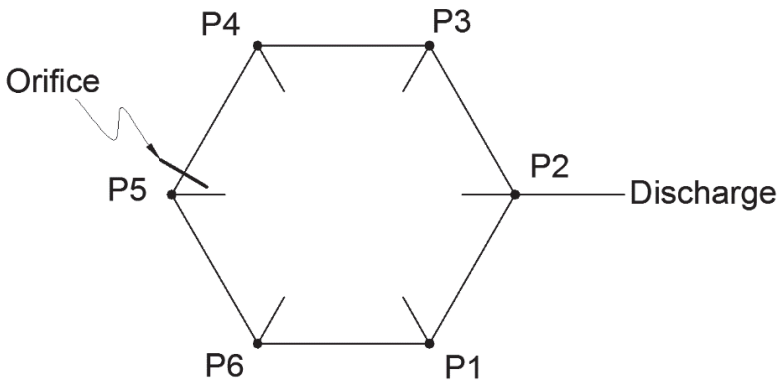


Fig. 3.33 Hexagonal pump configuration with orifice plate.

The computed discharge pressure and flow are presented in Fig. 3.34 below. The magnitude of the peak to peak flow and pressure fluctuations are the similar to those calculated for the original Hexagonal pump. However, the spectra and dominating frequencies of the two signals are different.

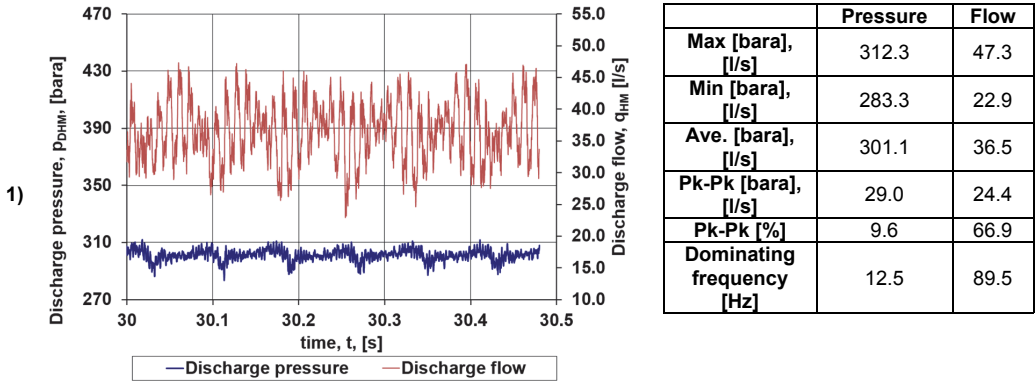


Fig. 3.34 Discharge pressure and flow for the hexagonal pump with orifice.

The main differences between the hexagonal pump with and without orifice are in the hexagonal manifold. The orifice reduces considerably the peak to peak value of pressure pulsation in the manifold from 200 bar to 30 bar (Fig. 3.35).

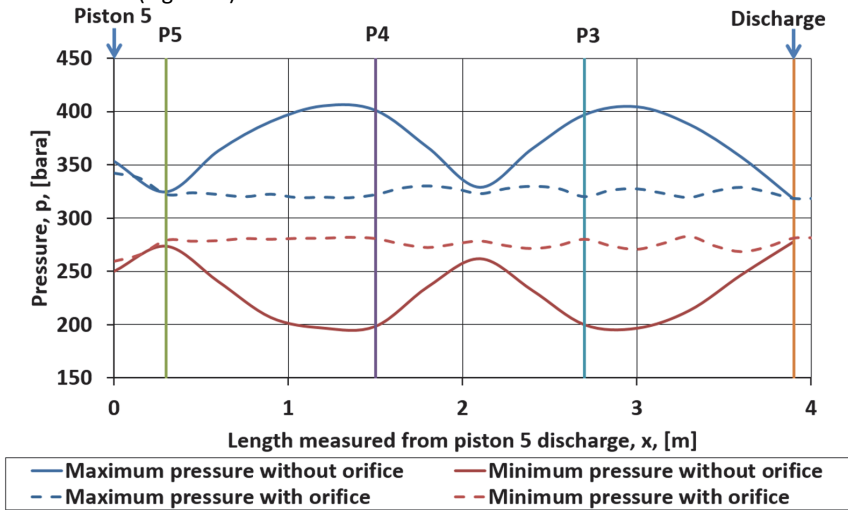


Fig. 3.35 Maximum and minimum pressure values recorded during the simulation along a branch of the hexagonal discharge manifold with and without orifice.

The orifice plate has an isolating effect between the two hexagonal manifold branches P5-P4-P3-P2 and P5-P6-P1-P2. This is observable in Fig. 3.36 where the flow in pipe section P5-P4, just after the orifice plate, is graphed for a piston cycle and compared with the discharge of piston 5.

As shown in Fig. 3.36, the alternating intensity in the flow direction in P5 of the Hex ring has diminished considerably in comparison to the original configuration (Fig. 3.29). The peak values have a maximum magnitude of 10 l/s while for the original geometry had a value of 60 l/s. The behavior of this flow is dictated roughly the discharge of piston 5, with a positive flow value (from P5-P4) when the piston is discharging and a negative flow value when the piston 5 is in the suction phase.

The orifice diminishes the severity of flow direction changes in the rest of pipe section in the hexagonal manifold, forcing the flow to move towards the discharge.

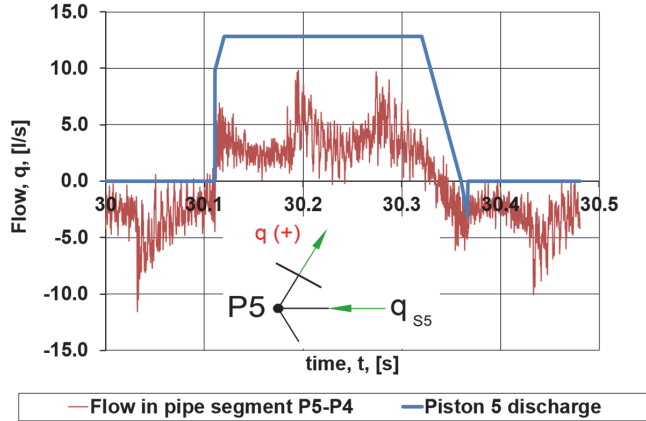


Fig. 3.36 Reciprocating flow in section P5-P4 of the hexagonal manifold with orifice plate installed.

3.3.4.2 Case 2. Hexagonal pump with orifice plate and gas accumulator.

A gas accumulator was placed at the discharge piping of the pump (1 m after the point P2) as presented in Fig. 3.37. The accumulator chosen was a 20 gallons pneumatic dampener with nitrogen charge (polytropic coefficient $n=1.2$). The precharge pressure was set to 242.3 bara. The details about the sizing of the accumulator are presented in Appendix F3. The accumulator is assumed to be connected directly to the pipe with no hydraulic loss.

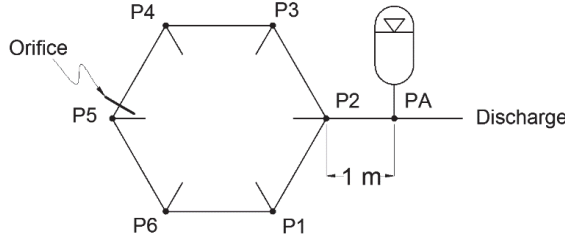


Fig. 3.37 Hexagonal pump configuration with orifice plate and gas accumulator.

The computed discharge pressure and flow are presented in Fig. 3.38. The magnitudes of the peak to peak flow and pressure fluctuations have decreased dramatically with the employment of the gas accumulator.

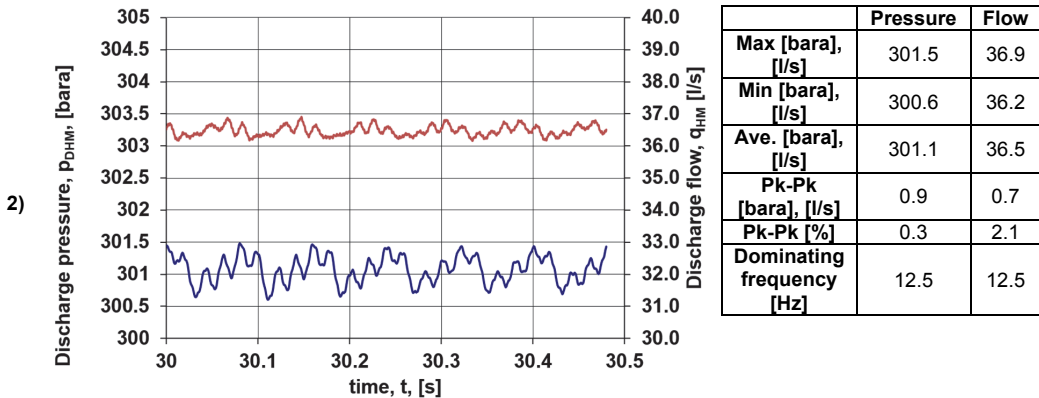


Fig. 3.38 Discharge pressure and flow for the hexagonal pump with orifice and gas accumulator.

Conclusions and Recommendations

As part of future work, it is highly recommended to perform other complementary numerical and experimental studies to confirm and support the given observations.

- The hexagonal pump piston driven by the special shaped cam has significantly better kinematics characteristics than those of a piston driven with a crankshaft mechanism. This characteristics are: uniform speed for larger time periods and zero acceleration during a big part of the piston cycle.
- A methodology for estimating the valve opening delays of the hexagonal pump was presented and demonstrated. The values obtained are similar to those values in the literature for traditional crankshaft reciprocating pump.
- The valve movement of the hexagonal pump was successfully modeled using a 1D model programmed in MS Excel and a 2D model built in a commercial CFD software. According to the results the valve movement follows a curve similar to the discharge flow profile of the piston.
- The CFD simulation of the valve movement yielded slightly different results from those of the simplified 1-D model. A suggestion is provided for improving the 1D model.
- The hexagonal manifold discharge configuration impedes the superposition of the individual piston flow discharges. The main reason for this is that it causes a complex interaction between the piston's discharge and the flow in the pipe sections.
- The hexagonal manifold generates the appearance of multiple dominant frequencies in the discharge pressure signal. Some of these pressure fluctuations occur at much higher frequencies than typical multiplex pumps. Usually the amplitudes of such frequencies must be limited to avoid the excitation of structural and piping supports.
- The delays in the piston cycle (i.e. the volumetric efficiency) are important parameters that have to be accounted for in the modeling of reciprocating pumps.
- The pressure pulsation generated by a hexagonal pump configuration is significantly less than the one produced by a linear superposition of the pistons discharges. This indicates that the hexagonal manifold provides certain level of dampening against pressure pulsations.
- Due to the high levels of pressure pulsation detected in all the analyzed systems, the need of installation of a pulsation dampening device is mandatory.
- The orifice plate improves significantly the pressure and flow fluctuation in the hexagonal manifold. However it doesn't improve the pressure pulsation levels downstream the pump.
- The installation of a 20 gal gas pulsation dampener in addition to the orifice plate reduced dramatically the pressure pulsation levels in the system. The resulting configuration however has a bigger footprint than the original Hexagonal pump.

References

- Borregales, M.; Cappelletto, J., Stanko, M. Shmueli, A. Asuaje, M. (2014). Model Building Using Genetic Algorithm for Data Fitting. *Proceedings of XII International congress of Numerical Methods in Engineering and Applied Science. CIMENICS. 24-26 march 2014. Isla de Margarita. Venezuela.*
- Collier, S.L. 1983, *Mud pump Handbook*. Houston Texas. Gulf Publishing Company.
- Fine, R. & Millero, F. J. (1973). Compressibility of water as a function of temperature and pressure. *Journal of Chemical Physics* 59 (10): 5529–5536.
- Henshaw, Terry, (2009) Power Pump Valve Dynamics. A Study of the Velocity and Pressure Distribution in Outward-Flow Bevel-Face and Flat-Face Power Pump Valves. *Proceedings of 25th International Pump Users Symposium, Houston, Texas, 2009.*
- HYDAC International. *Accumulator Technology. Product Catalogue (n.d.)*. Retrieved from www.hydac.ro/resurse/Acumulatori.pdf.
- Karassik, Igor J.; Messina, Joseph P.; Cooper, Paul; Heald, Charles C. (2008). *Pump Handbook*. 4th Edition. McGraw-Hill.
- Kverneland, H., Kyllingstad, Å., Moe, M., (2003). Development and Performance Testing of the Hex Mud Pump. *Proceedings of SPE/IADC Drilling Conference, Amsterdam, Netherlands. SPE/IADC 79831*
- Kverneland, H., Kyllingstad, Å., Moe, M., (2005). Operational experience with use of a Hex pump on a land ring. *Proceedings of SPE/IADC Drilling Conference, Amsterdam. SPE/IADC 92507.*
- Kyllingstad, Å., Nessjøen P. (2011). Condition based maintenance: A new early leak Detection system for mud pumps. *Proceedings of SPE/IADC Drilling Conference, Amsterdam, Netherlands. SPE/IADC 139888.*
- Moe, M., Kyllingstad, Å. (2006) U.S. Patent No. 7,004,121. Washington DC: US patent and Trademark office.
- Wylie, E.B., Streeter, V.L., Lisheng Suo. (1993) *Fluid Transients in Systems*. 8th edition, Prentice Hall.
- Økland, J. (2013, December). *Bygger om Songa Trym*. Retrieved from http://www.offshore.no/sak/60380_bygger_om_songa_trym (last accessed 13 march, 2014).

Appendix A3

Public drilling records of a platform with the Hexagonal pump installed

Public records of OSEE drilling campaigns

Oseberg East Development Wells							
	Wellbore name	Entry date	Completion date	Purpose	Status	Content	Elapsed days
1	30/6-E-2	13/01/1999	26/04/1999	PRODUCTION	PRODUCING	OIL	103
2	30/6-E-9	02/05/1999	07/06/1999	INJECTION	PLUGGED	GAS	36
3	30/6-E-4	01/07/1999	30/07/1999	PRODUCTION	PLUGGED	OIL	29
4	30/6-E-4 A	30/07/1999	11/09/1999	PRODUCTION	PLUGGED	OIL	43
5	30/6-E-13	25/09/1999	04/10/1999	PRODUCTION	PRODUCING	WATER	9
6	30/6-E-6	06/10/1999	19/01/2000	INJECTION	PLUGGED	NOT AVAILABLE	105
7	30/6-E-14	21/01/2000	13/03/2000	INJECTION	INJECTING	WATER	52
8	30/6-E-1	02/04/2000	13/05/2000	PRODUCTION	PLUGGED	OIL	41
9	30/6-E-1 A	13/05/2000	02/06/2000	PRODUCTION	PRODUCING	OIL	20
10	30/6-E-8	05/06/2000	04/08/2000	PRODUCTION	PRODUCING	OIL	60
11	30/6-E-10	04/08/2000	18/08/2000	PRODUCTION	PRODUCING	WATER	14
12	30/6-E-12	27/08/2000	30/09/2000	INJECTION	INJECTING	WATER	34
13	30/6-E-9 A	23/09/2000	12/11/2000	INJECTION	INJECTING	WATER	50
14	30/6-E-5	13/11/2000	25/11/2000	PRODUCTION	PLUGGED	OIL	12
15	30/6-E-5 A	25/11/2000	07/12/2000	PRODUCTION	PRODUCING	OIL	12
16	30/6-E-7	02/01/2001	26/01/2001	OBSERVATION	PLUGGED	NOT APPLICABLE	24
17	30/6-E-7 A	27/01/2001	20/02/2001	PRODUCTION	PLUGGED	OIL	24
18	30/6-E-11	21/02/2001	12/03/2001	OBSERVATION	PLUGGED	NOT APPLICABLE	19
19	30/6-E-11 A	12/03/2001	22/04/2001	PRODUCTION	PLUGGED	NOT AVAILABLE	41
20	30/6-E-15	24/04/2001	15/06/2001	PRODUCTION	PLUGGED	OIL	52
21	30/6-E-15 A	27/06/2001	05/10/2001	PRODUCTION	PRODUCING	OIL	100
22	30/6-E-6 A	23/10/2001	15/11/2001	OBSERVATION	PLUGGED	NOT APPLICABLE	23
23	30/6-E-6 B	15/11/2001	20/12/2001	INJECTION	INJECTING	WATER/GAS	35
24	30/6-E-3	26/02/2002	12/04/2002	PRODUCTION	PLUGGED	OIL	45
25	30/6-E-3 A	13/04/2002	06/06/2002	PRODUCTION	CLOSED	OIL	54
26	30/6-E-11 B	16/06/2002	02/07/2002	OBSERVATION	PLUGGED	NOT APPLICABLE	16
27	30/6-E-11 C	03/07/2002	03/08/2002	INJECTION	INJECTING	GAS	31
28	30/6-E-4 B	26/05/2008	22/12/2011	PRODUCTION	SUSP.AT TD		1305

Well NO 30/6 E-4 B drilling							
	Wellbore name	Entry date	Completion date	Purpose	Status	Content	Elapsed days
28-a	30/6-E-4 B top section	26/05/2008	28/06/2008	Section 1/12x20	17-suspended		33
28-b	30/6-E-4 B	15/03/2011	22/12/2011	PRODUCTION	completed	244 drilling days	282

Appendix B3

Hexagonal pump piston kinematics and valve delays

Hexagonal piston velocity function vs. shaft rotation angle:

$$V(\theta) = \omega \cdot \left(\frac{S}{180} \right) \cdot \left\{ \begin{array}{ll} \left(\frac{1}{30} \right) \cdot \theta & \text{if } 0 \leq \theta \leq 30 \\ 1 & \text{if } 30 < \theta \leq 180 \\ \left(-\frac{\theta}{30} + 7 \right) & \text{if } 180 < \theta \leq 210 \\ \left(-\frac{\theta}{20} + 10.5 \right) & \text{if } 210 < \theta \leq 240 \\ -1.5 & \text{if } 240 < \theta \leq 330 \\ \left(\frac{\theta}{20} - 18 \right) & \text{if } 330 < \theta \leq 360 \end{array} \right\} \quad \text{Eq. B3.1}$$

Hexagonal piston acceleration function vs. shaft rotation angle:

$$a(\theta) = \omega^2 \cdot \left(\frac{S}{180} \right) \cdot \left\{ \begin{array}{ll} \left(\frac{1}{30} \right) & \text{if } 0 \leq \theta \leq 30 \\ 0 & \text{if } 30 < \theta \leq 180 \\ \left(-\frac{1}{30} \right) & \text{if } 180 < \theta \leq 210 \\ \left(-\frac{1}{20} \right) & \text{if } 210 < \theta \leq 240 \\ 0 & \text{if } 240 < \theta \leq 330 \\ \left(\frac{1}{20} \right) & \text{if } 330 < \theta \leq 360 \end{array} \right\} \quad \text{Eq. B3.2}$$

Where:

θ Hex pump shaft rotation angle, [deg]

S Stroke length, [m]

ω Hex pump rotational speed [deg/s]

Estimation of valves opening and closing delays

1. Estimation of discharge valve closing delay (α_3) and suction valve closing delay (α_1)

In fig. 1 in the paper by Kyllingstad & Nessjøen (2011), vibrations were measured in a location close to a pumping chamber of the Hexagonal pump (Fig. B3.1). The spikes in the curve represent the closing (hitting against the seat) of suction and discharge valves. The graph is adjusted when piston starts the discharge cycle. With the speed of the pump (95 SPM) valve delays were calculated from the graph time values (B3.1).

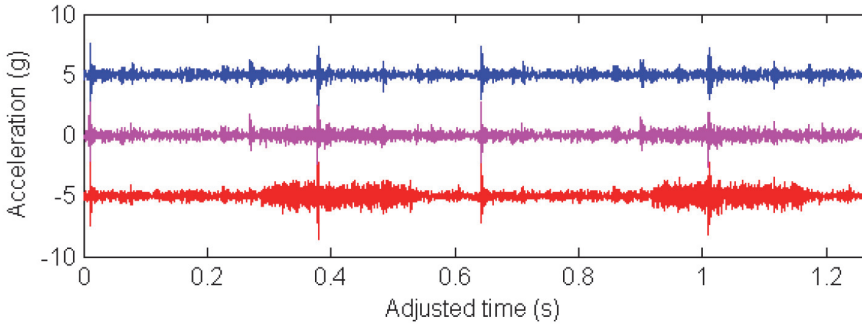


Fig. B3.1 Pump vibrations during a developing leak, taken from Kyllingstad and Nessjøen (2011)

Table B3.1 Measured valve closure delays

suction valve closure delay ($\alpha 1$) [°]	5
discharge valve close delay ($\alpha 3$) [°]	5

2. Procedure for estimation of discharge valve opening delay (fluid compression) ($\alpha 2$):

The discharge valve opening delay was calculated with the volume variation from condition 1 (DV+PV1) to condition 2 (DV+PV2) (shown in Fig. B3.2). In this figure the piston head is compressing the fluid from below, DV means dead volume, and PV is piston volume. In state 1 suction valve is closed, after some back flow has been sent to the suction line. The pressure in the cavity (p_c) is slightly above the pressure in the suction line (p_s). In state 2, the piston has continued its discharge stroke, and pressure has risen to a value slightly above the pressure in the discharge line (p_d).

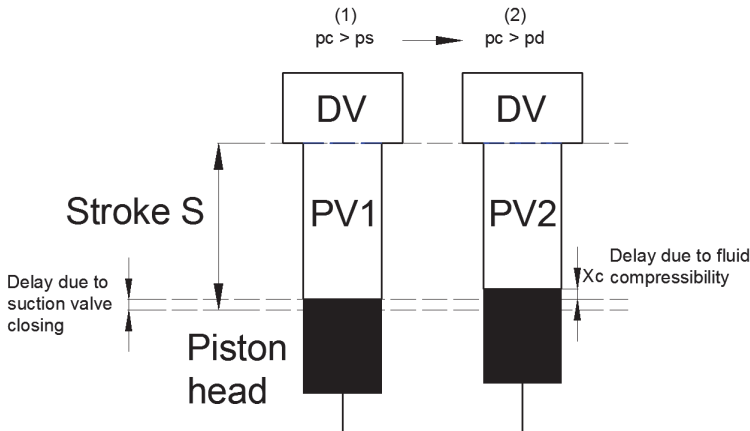


Fig. B3.2 Schematic representation to calculate compression valve delay

- Initial piston volume (PV1) was calculated using $\alpha 1$ as an input a suction valve closure delay ($\alpha 1$)
- The volume variation (PV1-PV2) during the compression process was calculated using the correlation by Fine & Millero(1973) for salt water.
- Calculated piston displacement (X_c) is converted to shaft rotation
- General data used in the calculations is presented in Table B3.2.

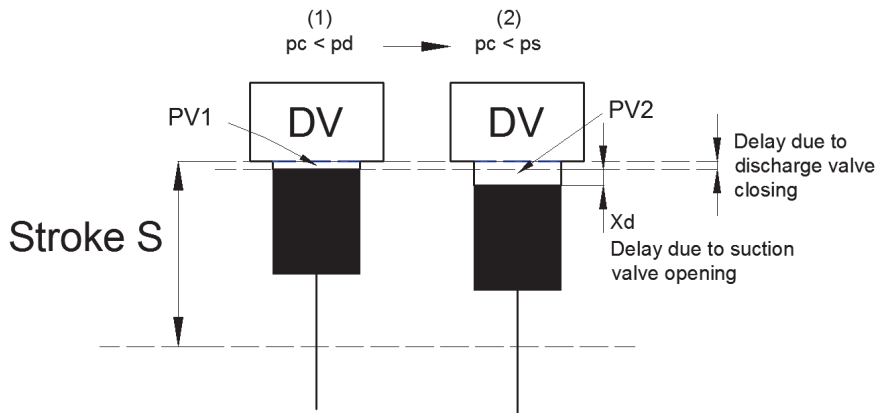
Table B3.2 Values used in compression valve delay calculation

Dead volume (DV) [m³]	0.002770
Initial cavity pressure (pc1) [bara]	4
Final cavity pressure* (pc2) [bara]	597

*value calculated by assuming average discharge pressure of 300 bara and using the valve dimensions specified in Appendix C3.

3. Procedure for estimation of suction valve opening delay (fluid decompression) ($\alpha 4$):

The decompression valve delay was calculated with the volume variation from condition 1 (DV+PV1) to condition 2 (DV+PV2) (shown in Fig B3.3). In state 1 discharge valve is closed, after some back flow has entered the piston cavity. The pressure in the cavity (pc) is slightly below the pressure in the discharge line (pd). In state 2, the piston has continued its suction stroke, and pressure has decreased to a value slightly below the pressure in the suction line (ps).

**Fig B3.3 Schematic representation to calculate decompression valve delay**

- Initial piston volume (PV1) is calculated using as an input the discharge valve closure delay ($\alpha 3$)
- The volume variation (PV1-PV2) during the compression process was calculated using the correlation by Fine & Millero (1973).
- Calculated piston displacement (Xd) is converted to shaft rotation
- General data used for the calculations is presented in Table B3.3.

Table B3.3 Values used in calculation of decompression valve delay

Dead volume (DV) [m³]	0.002770
Initial cavity pressure (pc1) [bara]	300
Final cavity pressure * (pc2) [bara]	2

*value calculated by assuming average suction pressure of 4 bara and using the valve dimensions specified in Appendix C3.

Appendix C3

Hexagonal pump check valves dimensions

The dimensions presented in this appendix were measured by the author

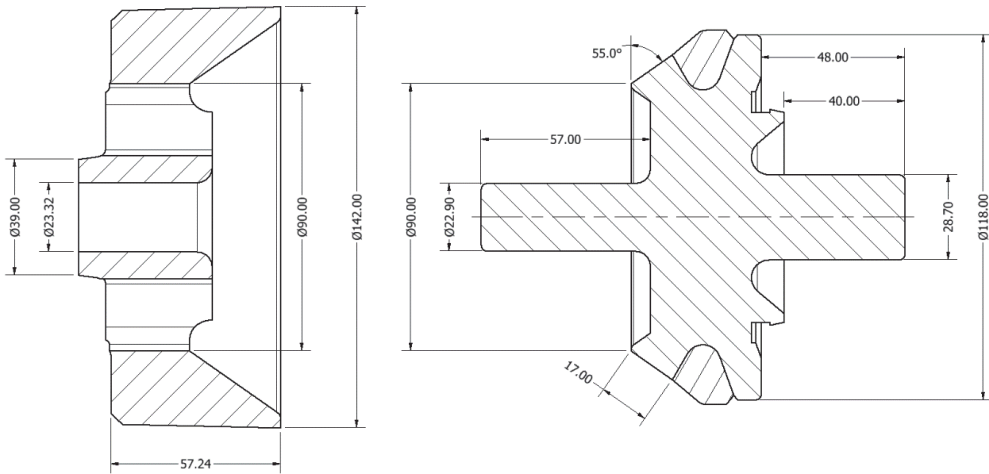


Fig. C3.1 Approximated measured dimensions of valve type 1

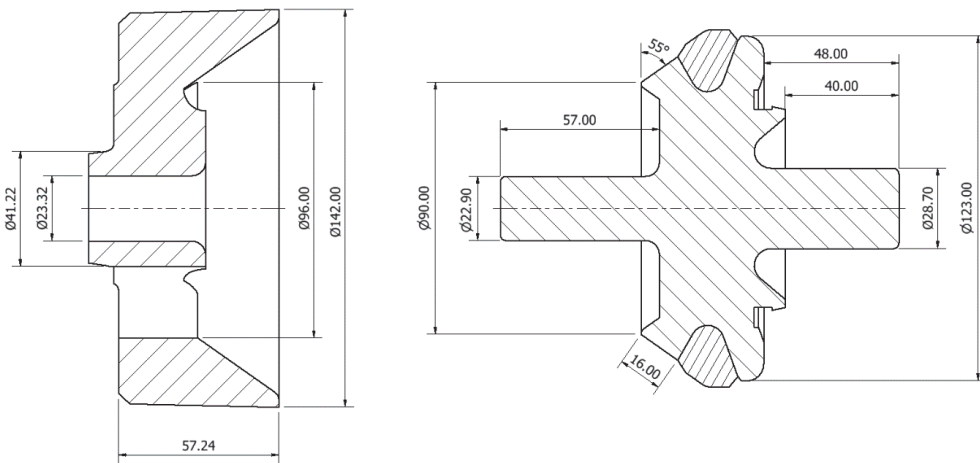


Fig C3.2 Approximated measured dimensions valve type 2

Table C3.1 Valve components measured data

Valve type 1 weight [Kg]	3.132
Valve type 2 weight [Kg]	3.092
Spring stiffness [N/m]	15784

Appendix D3

Axisymmetric 2D CFD fluid structure numerical simulation of the discharge valve dynamics

The CFD model was setup using the software Ansys CFX v13.0. The fluid structure interaction modeling approach used is called Rigid body solver with mesh deformation. It consists on the following:

- The valve surfaces (boundaries) in the mesh are allowed to move and are linked to a rigid body type motion.
- The rigid body motion is calculated with the equation of motion (sum of forces equals to mass times acceleration). The forces considered are spring forces and fluid forces acting on the rigid body boundaries. The rigid body movement has been confined to the horizontal direction.
- The coupling between the fluid dynamics solution and the rigid body movement is implicit in time.

One angular section (2°) of the valve fluid domain was modeled taking advantage of the symmetry (as shown in Fig. D3.1). The boundary conditions are highlighted in colors in the figure and are presented in more detail in Fig. D3.2. The turbulence model employed was the K-epsilon model.

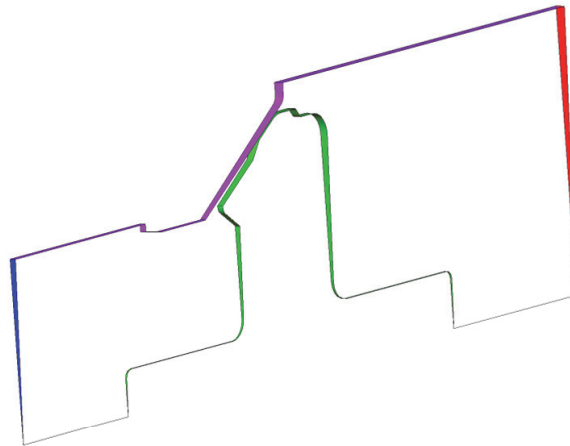


Fig. D3.1 Fluid domain included in the CFD model

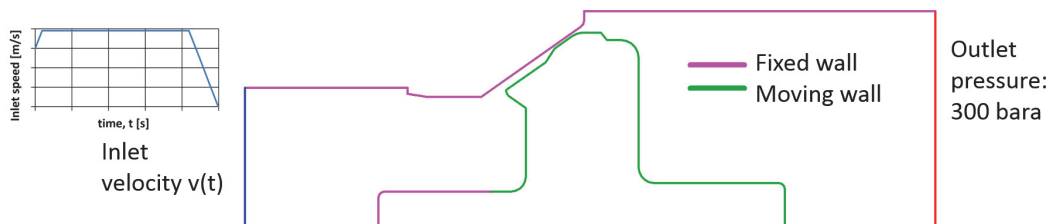


Fig. D3.2 Boundary conditions used for the CFD model

The inlet velocity boundary condition was calculated by taking the discharge flow rate from the piston chamber and dividing it by the total inlet area to the domain.

It is important to note that the valve stem located close to the inlet was not included as a moving surface therefore the forces acting on it are not included in the rigid body motion. This was done in order to minimize mesh deformations as much as possible. The resulting mesh after the mesh independence study has 22614 elements. Some snapshots of the mesh in the initial position and maximum valve opening position are presented in Fig. D3.3, Fig. D3.4 and Fig. D3.5.

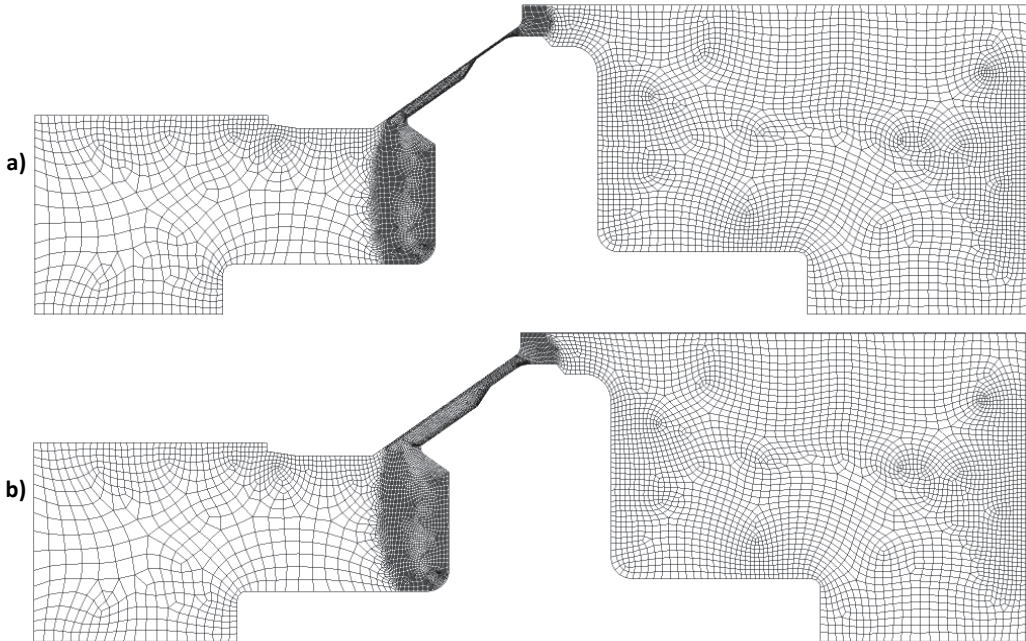


Fig. D3.3. Mesh view in the initial position (a) and in the maximum valve opening position (b)

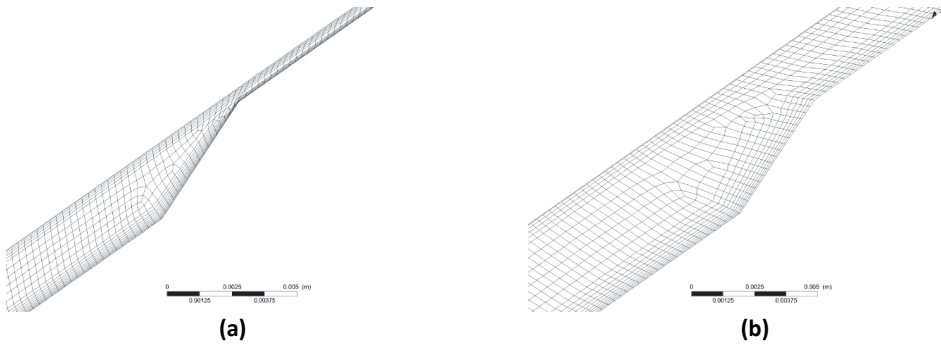


Fig. D3.4. Mesh details in the valve throat at the valve initial position and in the maximum valve opening position

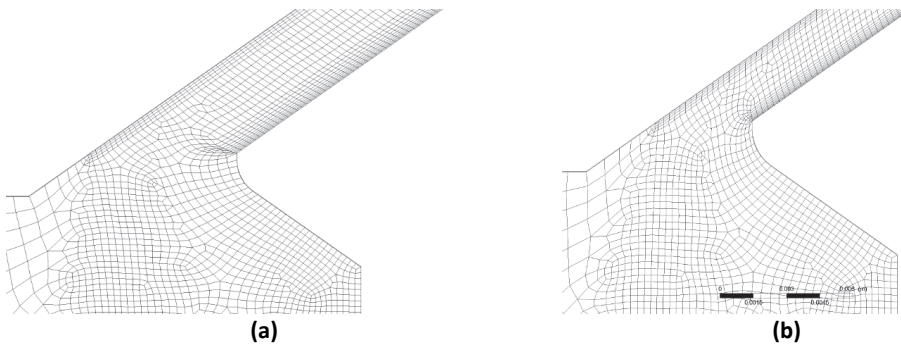


Fig. D3.5. Mesh details in the initial position and in the maximum valve opening position

Appendix E3

Transient Fluid Dynamics Numerical Simulator

The theory presented in this Appendix is based on the book by Wylie et al (1993) The numerical tool employed in the present study is a simulator for the analysis of unsteady flow of liquids in piping networks. It is based in the transient conservation equations of mass (Eq. E3.1) and momentum (Eq. E3.2), taking into account the fluid and pipe elasticity.

$$a^2 \cdot \frac{\partial V}{\partial x} + \frac{1}{\rho} \cdot \frac{\partial p}{\partial t} = 0 \quad \text{Eq. E3.1}$$

$$\frac{\partial p}{\partial x} + \rho \cdot \frac{\partial V}{\partial t} + \rho \cdot g \cdot \sin(\alpha) + \frac{\rho \cdot f \cdot V \cdot |V|}{2 \cdot D} = 0 \quad \text{Eq. E3.2}$$

Where:

a ...fluid wavespeed

ρ ...Fluid density

p ...Pressure

V ...Fluid velocity

g ...Gravitational acceleration

t ...time

f ...Friction factor

α ...Pipe inclination angle

D ...Pipe inner diameter

The partial differential equations (Eq. E3.1) and (Eq. E3.2) are converted to 2 ordinary differential equations (Eq. E3.3 and Eq. E3.5) using the method of the characteristics. Each equation however is valid only for the positions and times that comply with conditions (Eq. E3.4) and (Eq. E3.6) respectively.

$$+\frac{1}{\rho \cdot a} \frac{dp}{dt} + \frac{dV}{dt} + g \cdot \sin(\alpha) + \frac{f \cdot V \cdot |V|}{2 \cdot D} = 0 \quad \text{Eq. E3.3}$$

$$\frac{dx}{dt} = a \quad \text{Eq. E3.4}$$

$$-\frac{1}{\rho \cdot a} \frac{dp}{dt} + \frac{dV}{dt} + g \cdot \sin(\alpha) + \frac{f \cdot V \cdot |V|}{2 \cdot D} = 0 \quad \text{Eq. E3.5}$$

$$\frac{dx}{dt} = -a \quad \text{Eq. E3.6}$$

Equations Eq. E3.3, Eq. E3.4, Eq. E3.5 and Eq. E3.6 were discretized using finite differences on the temporal-spatial grid shown in Fig. E3.1 below. The resulting equations are presented below: Eq. E3.7, Eq. E3.8, Eq. E3.9, Eq. E3.10.

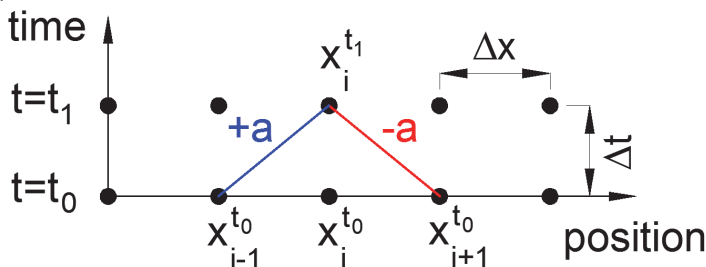


Fig. E3.1 Temporal and spatial discretization used in the characteristics method

$$p_i^{t_1} - p_{i-1}^{t_0} + \rho \cdot a \cdot (V_i^{t_1} - V_{i-1}^{t_0}) + \rho \cdot g \cdot \sin(\alpha) \cdot \Delta x + \frac{\rho \cdot f \cdot V_i^{t_1} \cdot |V_{i-1}^{t_0}| \cdot \Delta x}{2 \cdot D} = 0 \quad \text{Eq. E3.7}$$

$$\frac{\Delta x}{\Delta t} = +a \quad \text{Eq. E3.8}$$

$$+ p_{i+1}^{t_0} - p_i^{t_1} + \rho \cdot a \cdot (V_i^{t_1} - V_{i+1}^{t_0}) + \rho \cdot g \cdot \sin(\alpha) \cdot \Delta x + \frac{\rho \cdot f \cdot V_i^{t_1} \cdot |V_{i+1}^{t_0}| \cdot \Delta x}{2 \cdot D} = 0 \quad \text{Eq. E3.9}$$

$$\frac{\Delta x}{\Delta t} = -a \quad \text{Eq. E3.10}$$

For the inner points of the pipe eq. Eq. E3.7 and Eq. E3.9 can be combined to obtain the solution for time t_1 . For the boundary nodes upstream of the pipe, Eq. E3.9 has to be used in combination with the boundary condition. For boundary nodes downstream of the pipe eq. Eq. E3.7 has to be used in combination with the boundary condition.

The friction factor was calculated by using the steady state approximation (Blasius for laminar flow and Colebrook correlation for turbulent flow).

All the existing pipes were considered supported as anchored upstream and thick-walled.

In pipe network systems the time step Δt has to be the same for each pipe section "j". The time step is calculated for each pipe section "j" according to equation (Eq. E3.11) below. Due to the fact that the wavespeed a_j and length L_j are *a priori* different for each section, it is very unlikely that an adequate integer number of subdivisions N_j will be found to achieve a unique Δt . In order to achieve a common Δt the wavespeed in each section was modified slightly ($\pm 2\%$).

$$\Delta t = \frac{L_j}{N_j \cdot a_j} \quad \text{Eq. E3.11}$$

Appendix F3

Gas Pulsation Accumulator

A simplified drawing of a pulsation accumulator is shown in Fig. F3.1. It is usually installed close to the discharge of the pump. The operating pressure of the accumulator will be close to the pressure existing in the line to which the accumulator is connected (p_d).

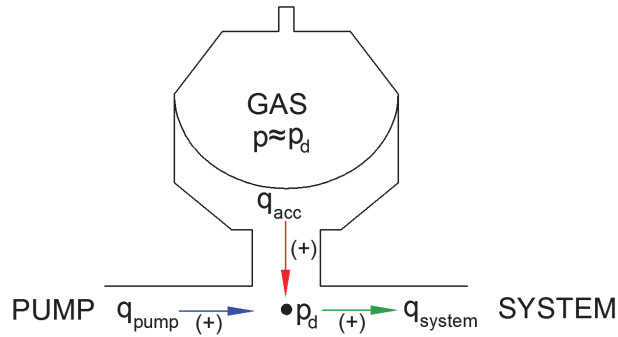


Fig. F3.1 Gas Accumulator installed at the pump exit

The ideal flow behavior of the system with the accumulator installed is shown in Fig. F3.2. When the pump is delivering flow exceeding the required flow by the system, the accumulator receives the compensating inflow (periods denoted by “-” in the figure). When the pump is delivering less flow than the required by the system, the accumulator provides the compensating outflow (periods denoted by “+” in the figure). Flow delivery or gather by the pulsation accumulator is dictated by pressure p_d . For a smooth operation, variation in p_d should be kept minimal (i.e. $\pm 1\%$) thus providing sufficient compensating flow.

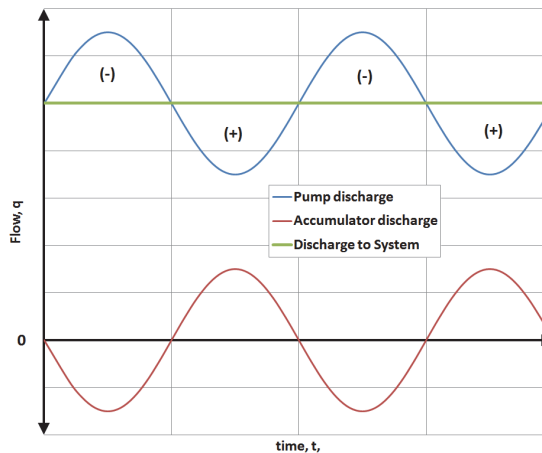


Fig. F3.2 Ideal Flow compensation from a gas accumulator

The pressure (p) and volume of the gas (V_g) in the accumulator will typically follow a thermodynamic polytropic process expressed by Eq. F3.1, where “ c ” is a constant. The constant c is computed with the precharge conditions ($p = p_{pc}$ and $V_g = V_{acc}$).

$$p \cdot (V_g)^n = c \quad \text{with} \quad p_{pc} \cdot (V_{acc})^n = c$$

Eq. F3.1

Simplified gas pulsation accumulator sizing equation

The sizing procedure shown in this section is based in a simplification of the gas accumulator sizing method of the company HYDAC (see references). It was assumed a precharge pressure/operating pressure ratio of 0.8, polytropic coefficient of 1.2 and an allowance of ± 1 % variation in the discharge pressure. Eq. F3.2 provides an estimation of the accumulator volume (V_{acc}) calculated from the volume to compensate ($\Delta V_{compensate}$).

$$V_{acc} = \frac{\Delta V_{compensate}}{0.0138} \tag{Eq. F3.2}$$

The volume to compensate is calculated by means of Eq. F3.3

$$\Delta V_{compensate} = \frac{\pi \cdot d_p^2 \cdot S \cdot \delta}{4} \tag{Eq. F3.3}$$

Where:

d_p Piston diameter

S Stroke length

δ coefficient of cyclic variation of the pump

For the present case, coefficient δ will be estimated by performing an average between the maximum flow fluctuation above average flow (Δq_{am}) and the maximum flow fluctuation below average flow (Δq_{bm}) in Fig F3.3.

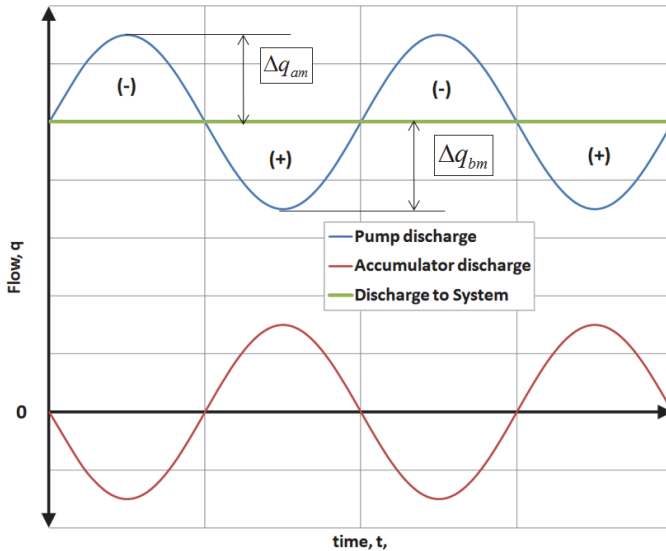


Fig. F3.3 Maximum flow fluctuation above average and below average

Sizing of gas accumulator for hydraulic simulation of Hexagonal pump discharge

A gas accumulator was sized based on the results of the numerical model of the Hex pump discharge presented in section 3.3.3. Relevant information for calculation is presented in. Table F3.1.

Table F3.1 Parameters used in Gas accumulator sizing

Maximum discharge flow during pump cycle [m³/s]	0.0414
Average discharge flow during pump cycle [m³/s]	0.0365
Minimum discharge flow during pump cycle [m³/s]	0.0255
Maximum flow fluctuation above average flow [%]	13.6
Maximum flow fluctuation above average flow [%]	30.1
Coefficient of cyclic variation of pump [%]	21.8
Cylinder volume [m³]	3.078E-3
$\Delta V_{compensate}$ [m³]	6.723E-4
V_{acc} [gal.]	12.87

A commercial accumulator of 20 gal capacity is selected, and pre-charged with gas at 242.3 [bara], based on the results for the particular case.

Appendix G3 Simplified resonance assessment of the discharge hydraulic system

The pressure pulsation generator element in the system is the volumetric pump. It excites the discharge pipe by introducing mass periodically which in turns causes a fluid compression or decompression in the boundary. The way the hydraulic system responds to this excitation is computed by solving the discretized momentum and mass fluid conservation equations.

The solution of these set of equations shows that pressure perturbations propagate in the hydraulic system with a wave type motion at a characteristic speed “ a ”. The wave speed “ a ” depends on the fluid and pipe characteristics. This justifies the employment of analogies from general acoustic theory which are useful to understand the interaction between the wave and the system. The pressure pulsations travel from the pump end to the constant pressure boundary. There are also phenomena such as constructive or destructive superposition and reflection when the pressure waves interact with each other and with the system elements and boundaries. The result is a series of pressure waves travelling in the system with their own distinctive amplitude, frequency and angle shift.

The superposition of all the pressure waves in the system yields a standing wave (or non-moving wave) where the pressure on each point in the system oscillates with a characteristic frequency and amplitude. For very simple acoustic systems it is possible to determine the wave frequency that yields maximum constructive superposition and thus maximum amplitude. This is called the natural frequency of the system. Any multiple of this frequency (called harmonics) yields also the maximum constructive superposition. If an acoustic system is excited with its fundamental frequency or any of its harmonics it is said that the system is in acoustic resonance.

The 40 m long pipe analyzed in the present study has two boundaries: pump and constant pressure. The pressure at the pump end has to change according to the amount of fluid that is being introduced to the system. This corresponds acoustically to a “closed end”. The pressure wave is reflected on a closed end like a mirror image: with the same amplitude and frequency.

The constant pressure boundary condition maintains the same pressure without being influenced by the rest of the system. This corresponds acoustically to an “open end”. The pressure wave is reflected on an open-end with the same amplitude and frequency but shifted 180°.

This hydraulic system was analyzed acoustically as a closed-end and open-end system. This is perfectly valid for cases (a) and (b) but for case c might be inadequate. The hexagonal manifold is a complex system of interconnected pipes that the current analysis is overlooking.

The fundamental frequency is calculated with Eq. G3.1:

$$f = \frac{a}{4 \cdot L} \quad \text{Eq. G3.1}$$

The expected maximum and minimum pressure values for each point of the system for different harmonics is shown in Fig G3.1. The pressure at each point pulsates with the corresponding harmonic frequency.

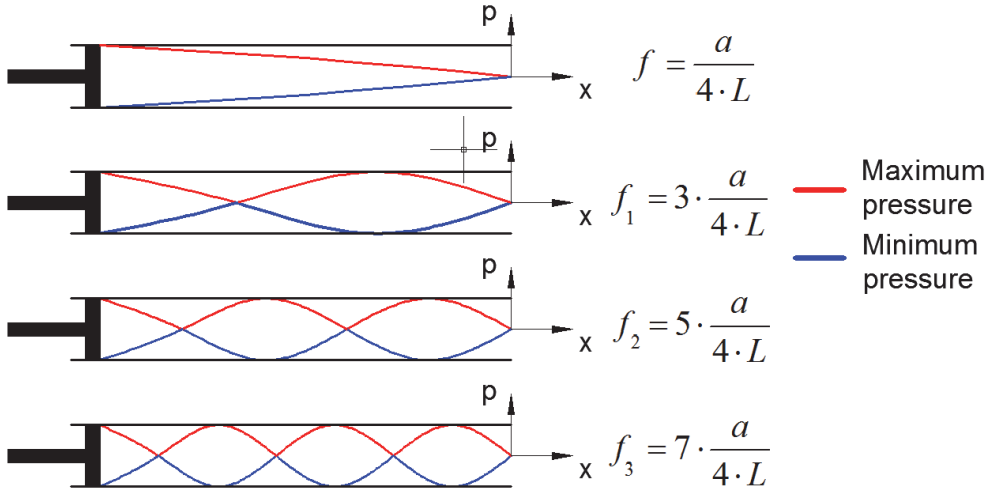


Fig. G3.1 Resonant mode shapes for an open-closed end pipe.

Eq. G3.1 is calculated for cases a, b and c in Table G3.1. The harmonics of these fundamental frequencies are also computed up to number 3. These values constitute the excitation frequencies where resonance is expected.

Table G3.1 Fundamental frequency and harmonics of the discharge pipe

Case	a/b	c
Wavespeed [m/s]	1200.91	1197.86
Fundamental frequency [Hz]	7.51	7.49
1st harmonic	22.52	22.46
2nd harmonic	37.53	37.43
3rd harmonic	52.54	52.41

The pressure waves/perturbations generated by the volumetric pump are not purely sinusoidal perfect waves. However there is typically a dominant frequency that contains most of the wave energy. This is usually taken as the representative frequency to make the acoustic-like analysis of the system. This frequency is usually dictated by the movement of the shaft.

In the case of a triplex pump there is an excitation 3 times within a shaft revolution and in the case of the hexagonal pump there is an excitation 6 times within a shaft revolution.

The excitation frequencies of the pumps for case a, b and c were computed and are shown in Table G3.2.

Table G3.2 Excitation frequencies for cases a,b,c

Case	a	b/c
Shaft speed [RPM]	125	125
Shaft speed [Hz]	2.08	2.08
Base frequency [Hz]	6.25	12.50
2nd harmonic [Hz]	12.50	25.00
3rd harmonic [Hz]	18.75	37.50
4th harmonic [Hz]	25.00	50.00
5th harmonic [Hz]	31.25	62.50
6th harmonic [Hz]	37.50	75.00

In case a) the pipe is hydraulically excited in its 2nd harmonic, by the 6th pump harmonic. In cases b) and c) the 2nd harmonic of the pipe is hydraulically excited by the 3rd pump harmonic.

Appendix A Details about the numerical models and computational tools employed in the thesis

The numerical models employed in this thesis can be classified into two main categories:

1. Numerical models built in specialized software. The model building process consists in preparing the input data (fluid properties, boundary conditions, etc.) and adapting them to the format and units required by the specialized software. Usually the software interface is employed (through fields or dialog boxes) to introduce the data, to select the appropriate modeling options, specify the output frequency, to run the simulations, check the convergence, and to read, visualize, analyze and export the results.

2. Numerical models programmed in specialized software. The model building process consists in creating computational routines or functions based on the physical equations that represent the phenomena and the algorithm to solve them. The input data connectivity, data processing and output data connectivity has to be defined in detail through programming logic.

Table A.1 presents an overview of the relevant numerical models and computational tools employed in the thesis. The models that belong to category “2” have been tagged with the word “**Programmed**” at the beginning of the model description. All the other models without this distinction belong to category “1”.

Table A.1. Main numerical models and computational tools employed in the thesis

CHAPTER 1			
TOPIC: Pressure reduction estimation with the deployment of the inline separator			
Section in thesis	Description	Author	Software
1.2.1	Pipesim models representing main production riser and separated stream riser for Cases 1,2,3,4. General settings: -Black oil treatment of the fluids thermodynamics -Steady state -Multiphase pressure drop calculation using the bja model. No slip assumption -Heat transfer calculations included (Insulated pipes). -Hydraulic network solver tolerance: 0.01 %. -Method to determine the viscosity of the oil water mixture: Water cut off (streams with watercut more than 60% are considered water continuous and less than 60% are considered oil continuous). -Viscosity dependence with temperature	Stanko	Pipesim V2011.1.2
TOPIC: Evaluating the capability of a CFD model to represent the segregation and separation phenomena in oil in water dispersion			
Section in thesis	Description	Author	Software
1.5	CFD models of a single pipe geometry for cases 1,2,3,4,5 General settings: -Structured mesh formed by hexahedrons (created in Ansys Icem) -Euler-Euler multiphase flow formulation -Particle model for the oil: Single diameter or multiple diameters or population balance using the homogeneous MUSIG model (Prince and Blanch for droplet coalescence and Luo and Svendsen for droplet breakage)	Stanko	Ansys CFX V13.0, V14.0

	<ul style="list-style-type: none"> -Interfacial forces considered: drag (Ishii Zuber), lift (Tomiyama), buoyancy, turbulent dispersion (Favre), lubrication (Frank) -Turbulence model: homogeneous k epsilon model -Constant fluid properties, no heat transfer considered -Newtonian fluid -Steady state -Wall treatment: smooth -Turbulence option at the inlet: Medium -Outlet pressure option: Pressure average over whole outlet -Discretization of the advection terms of the conservation equations: High resolution (blending of first and second order) -Timescale used for the solving process: Automatic or 0.02 s -Typical number of iterations: 600-2000. Typical running time: 8-24 hrs. Serial or parallel runs (2 partitions) 		
TOPIC:	CFD simulations to evaluate the inline separator performance		
Section in thesis	Description	Author	Software
1.6	<p>CFD models of a separator prototype geometry for two sets of inlet oil and water flow rates</p> <p>General settings:</p> <ul style="list-style-type: none"> -Structured mesh formed by hexahedrons (created in Ansys Icem) -Euler-Euler multiphase flow formulation -Particle model for the oil: Single diameter -Interfacial forces considered: drag (Ishii Zuber), lift (Tomiyama), buoyancy, turbulent dispersion (Favre), lubrication (Frank) -Turbulence model: homogeneous k epsilon model. -Constant fluid properties, no heat transfer considered -Newtonian fluid -Steady state -Wall treatment: smooth -Turbulence option at the inlet: Medium -Outlet pressure option: Pressure average over whole outlet -Discretization of the advection terms of the conservation equations: High resolution (blending of first and second order) -Timescale used for the solving process: Automatic or 0.02 s -Typical number of iterations: 600-2000. Typical running time: 8-24 hrs. Serial or parallel run (2 partitions) 	Stanko	Ansys CFX V13.0, V14.0

TOPIC:	Droplet size distribution prediction of an oil in water dispersion		
Section in thesis	Description	Author	Software
Appendix C1	<p>(Programmed) Excel spreadsheet to predict the droplet size distribution of an oil in water dispersion based in a Upper-Limit Log-Normal distribution</p> <p>General Settings:</p> <ul style="list-style-type: none"> -The equations and procedure presented in Appendix C1 were programmed by employing user defined functions and computed in spreadsheet cells -The excel standard solver (GRG method) was employed (using the interface) for tuning the model to measured droplet size distribution and observed maximum droplet diameter 	Stanko	Excel V2007
CHAPTER 2			
TOPIC:	Model based constrained optimization for production networks with ESP-produced, high water cut wells		
Section in thesis	Description	Author	Software
2.4, 2.5, 2.6	<p>(Partly Programmed) Pipe-It project to perform oil production maximization by changing well ESP speed of a Pipesim model</p> <p>General settings:</p> <ul style="list-style-type: none"> -VBS (Visual Basic script) and Excel VBA (Visual Basic for Applications) routines were programmed to communicate with the Pipesim models by using the Open Link functionality. These routines transfer data from text files to the Pipesim model and vice versa. -The main running sequence was set up using the Pipe-It graphical elements: write ESP frequencies in the Pipesim file, run the network solver, read the results, compute the values of the constrained variables. All the graphical elements were associated with the routines and files mentioned in the previous point. -The variables of interest (e.g. well ESP frequencies, oil production, suction pressure, etc) were spotted in the text files using the Linkz functionality of Pipe-It. This allowed to import them as variables in Pipe-It, to use them in further calculations and to pull them as variables for the optimizer. -Optimizer solvers employed: IPOPT, NOMAD and Reflection. NOMAD and Reflection use the default settings. The settings for the IPOT solver are: Perturbation size: 0.1, Tolerance: 1e-5, Constraint violation tolerance: 1e-5, Acceptable Tolerance: 1e-5, Acceptable constraint violation tolerance: 1e-5. 	Solrud, Røyset, Stanko	Pipe-It V 1.3
2.4, 2.5	Pipesim models representing a simplified oil production system for cases 1 (2 wells) and 2 (six wells, 2 clusters)	Stanko	Pipesim 2011.1.2

	<p>General settings</p> <ul style="list-style-type: none"> -Black oil treatment of the fluids thermodynamics -Steady state -Multiphase pressure drop calculation using bja model. No slip assumption. -Heat transfer calculations included but the system surroundings have the same temperature as the fluid -No dependence of the fluid viscosity with temperature -Hydraulic network solver tolerance: 0.01 % -Method to determine the viscosity of the oil water mixture: Water cut off (streams with watercut more than 49% are considered water continuous and less than 49% are considered oil continuous). The viscosity of the mixture is taken as the viscosity of the continuous fluid -Viscosity Correction for the ESP pump not activated. 		
2.5	<p>(Programmed) Excel model of the production system of case 2 (six wells, 2 clusters) with user defined functions representing pressure drop in pipe segments.</p> <p>General settings:</p> <ul style="list-style-type: none"> -An incompressible single phase pressure drop equation using water oil mixture properties was programmed by using user defined functions -The pump equation (pressure difference vs flowrate) was programmed by using user defined functions -The pressure of each important point in the production system (e.g. wellhead pressure, ESP suction pressure) was computed in a spreadsheet cell using the user defined functions and relevant input -The oil water mixture is always in the water continuous regime. The viscosity of the mixture is the viscosity of the water -No correction on ESP pump performance was done for Viscosity -No heat transfer or temperature effects were considered -The hydraulic network solving process (explained in detail in Appendix B2) was set up using arithmetic operations with the spreadsheet cells. The condition for network convergence (expressed as a sum of residuals) was reduced to one spreadsheet cell -The network solving convergence process and the optimization were then performed simultaneously by employing the excel solver (GRG method). The network solving condition was introduced as a constraint in the optimization settings (forcing the cell to be less than certain tolerance) 	Stanko	Pipesim 2011.1.2
2.6	<p>Pipesim model representing a real oil production surface network</p> <p>General settings:</p> <p>Undisclosed</p>	Oil company X	Pipesim 2011.1.2

CHAPTER 3			
TOPIC:	Hexagonal pump characteristics		
Section in thesis	Description	Author	Software version
3.2	<p>(Programmed) Excel file with the hex pump piston curves, compounded together for discharge and suction</p> <p>General settings:</p> <ul style="list-style-type: none"> -The Hexagonal pump piston displacement, velocity and acceleration equations versus time were programmed using user defined functions in VBA. -The Hexagonal pump piston discharge and suction flow rate profiles assuming perfect superposition were programmed using user defined functions in VBA. 	Stanko	Excel 2007
3.2.2	<p>(Programmed) Excel file with to calculate hex pump fluid compressibility delays</p> <p>General settings:</p> <ul style="list-style-type: none"> -The relevant equations required to perform the calculations were programmed using user defined functions. -The method described in Appendix B3 for estimating the valve delays due to fluid compressibility was programmed. The calculations were made in spreadsheet cells -The excel solver (GRG method) was employed in a routine to compute the fluid compressibility delay (expressed in rotation angle of the pump shaft) 	Stanko	Excel 2007
TOPIC:	Simulation of the hexagonal pump valve dynamics		
Section in thesis	Description	Author	Software version
3.2.3.2	<p>(Programmed) Excel file to perform a one dimensional simulation of discharge and suction valve dynamics</p> <p>General Settings:</p> <ul style="list-style-type: none"> -Incompressible fluid with constant properties -The terms of the second order differential equation (valve movement equation) were programmed using user defined functions -Input and output data were read from and written to spreadsheet cells -The 4th order Runge-Kutta to solve the differential equation was programmed in a VBA routine using the user defined functions mentioned earlier. Results were written to the cells in the spreadsheet 	Stanko	Excel 2007
3.2.3.4	<p>CFD model for simulation of discharge valve movement using a CFD 2D model</p> <p>General Settings:</p> <ul style="list-style-type: none"> -Incompressible fluid with constant properties -No temperature calculations performed -Transient simulation (timestep 0.001 s). Total time: 0.26 s but simulation stopped at 0.253 s because of excessive mesh deformation 	Stanko	Ansys CFX V14.0, Ansys Workbench

	<ul style="list-style-type: none"> -Fixed number of mesh elements but deformable mesh option (change position of nodes according to the displacement of the boundaries). Mesh motion model: Displacement Diffusion, with mesh stiffness 1.0 -Turbulence level at the inlet: Medium -Discretization of the advection terms of the conservation equations: High resolution (blend of first and second order) -Outlet boundary condition: Opening (Allows fluid recirculation) option: Entrainment -Transient scheme: second order backward Euler -Turbulence numeric: first order -Maximum solver iterations for each time step: 10 -Initialization values for each time step: automatic (blend between the values of the previous time step and an extrapolation) 		
TOPIC:	Transient hydraulic 1D simulation of the system downstream the hex pump		
Section in thesis	Description	Author	Software version
3.3	<p>Models for the simulations of Cases 1 (Hexagonal manifold),2(linear manifold with Hex piston discharge),3 (triplex pump)</p> <p>General settings:</p> <ul style="list-style-type: none"> -Constant fluid properties, Newtonian, isothermal fluid, fixed viscosity -Transient simulation with automatic calculation of initial conditions -Loss model for the junctions: No loss -Pipe support type: Thick pipe anchored upstream -Transient control: Use variable pipe resistance (update the friction factor in every time step) 	Stanko	AFT Impulse V4.0
3.3.4	<p>Models for simulations of the hexagonal pump with 2 pulsation arresting measures: orifice plate and pulsation dampener.</p> <p>General settings:</p> <ul style="list-style-type: none"> -Constant fluid properties, Newtonian, isothermal fluid, fixed viscosity, -Transient simulation with automatic calculation of initial conditions -Loss model for the junctions: No loss -Loss model for the orifice plate: constant K factor -Loss model for the accumulator exit: No loss -Pipe support type: Thick pipe anchored upstream -Transient control: Use variable pipe resistance(update the friction factor in every time step) 	Stanko	AFT Impulse V4.0

Appendix B Brief description of some of the computational tools employed in the thesis

• Pipesim

Pipesim is a one dimensional, steady state multiphase flow simulator originally developed by the company Baker Jardine that was acquired by Schlumberger in 2001. Pipesim allows to simulate hydrocarbon production systems from the well until the processing facilities including elements such as reservoir inflow, well tubing, ESPs, separators, pipes, pumps, compressors, heat exchangers, among many others. Each element has usually a variety of preprogrammed equations and options available for the modeling.

The program has a graphical interface (as shown in Fig. A.1) where the elements can be dragged to the canvas with the mouse pointer for model building. The settings of the individual components are inputted by double clicking the elements and filling the dialog screen. The common and general settings are inputted by using the menu (an example is shown in Fig. A.2.).

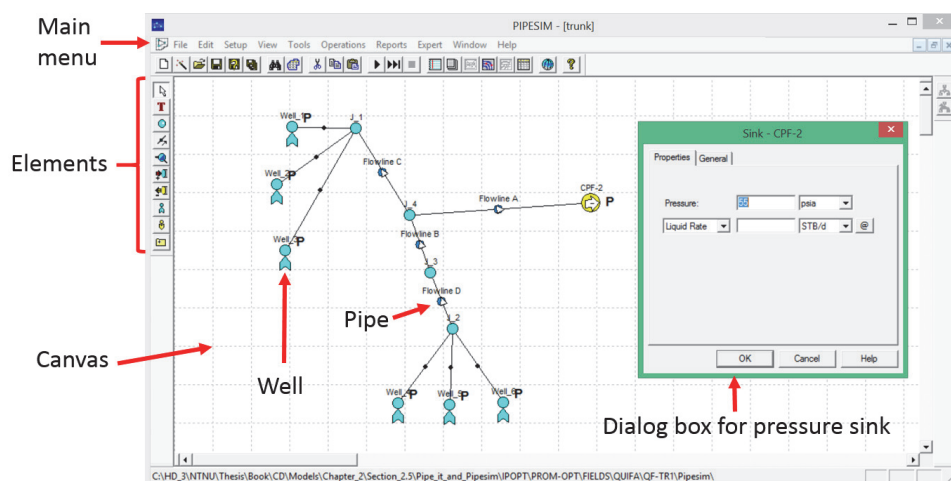


Fig A.1. Pipesim typical interface

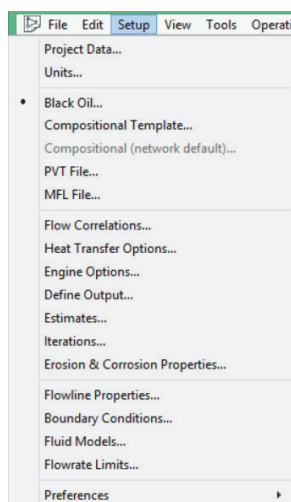


Fig. A.2. Details of the general Setup menu of Pipesim

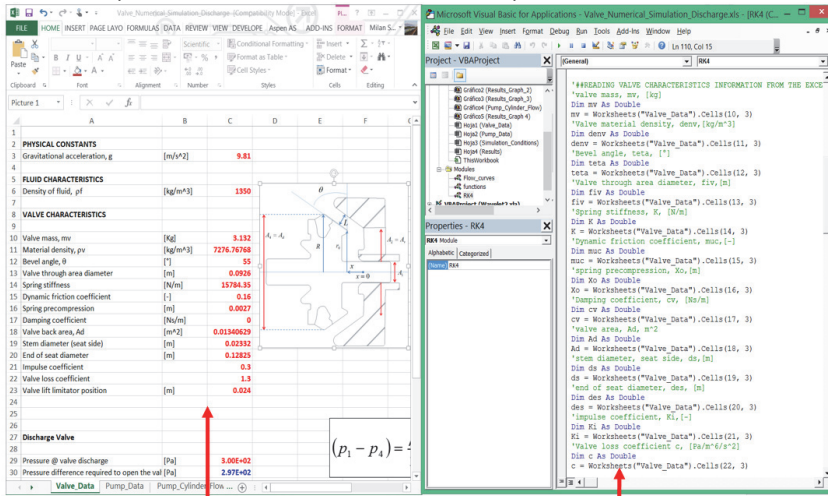
The same interface is used for running the simulations and reviewing the results.

The program also allows to set up optimization cases by defining objective variables (e.g. oil flow rate), controllable or adjustable variables (valve openings) and constrained variables (e.g. maximum water production) and to perform optimization by employing numerical techniques.

• Excel

Excel is a well-known spreadsheet application by Microsoft. Excel has an extensive list of powerful features that allow the user to perform many operations. Some of the features used in this thesis are:

-Macro programming: Excel supports programming through VBA (visual basic for applications). This functionality allows to create programmable routines, functions (also called user defined functions), dialog boxes, buttons etc. It allows also to open files and access other programs. All the programming is done in a separate module (Called Visual Basic Editor, as shown in Fig. A.3.). Functions and routines usually read data from the spreadsheet cells and write data to the spreadsheet cells.



Input data in excel sheet

Routine to read information from excel sheet and perform calculations in Excel's Visual Basic Editor

Fig. A.3. Excel spreadsheet and VBE interface

-Standard solver: the excel solver is an add-in that allows to perform numerical optimization on the cells in the spreadsheet. The excel solver add-in is provided by a third party company called Frontline Solvers. An example of the standard solver interface is shown in Fig. A.4.

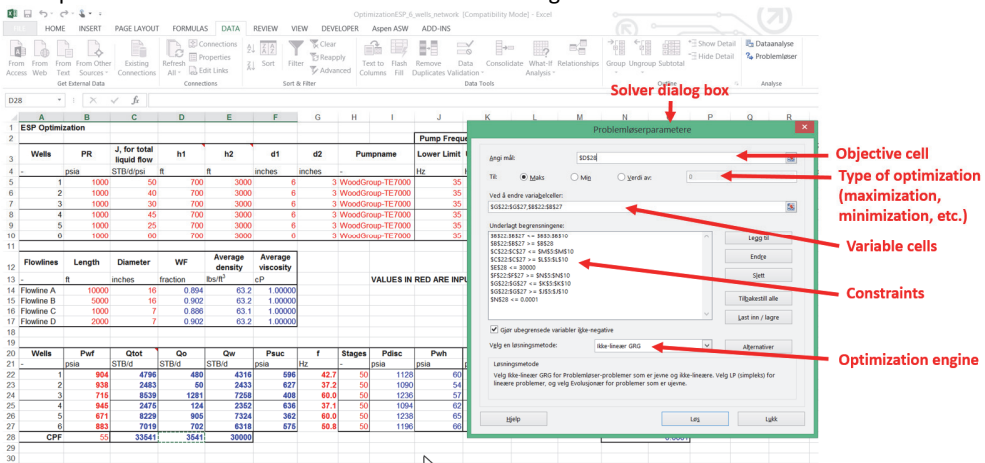


Fig. A.4. Excel standard solver interface

• Pipe-It

Pipe-It is a computational tool to integrate and optimize software. It is developed and marketed by the company Petrostreamz. It is mainly oriented to software related with the petroleum industry but it is flexible enough to integrate a large variety of programs existing in the market.

Pipe-It allows to connect input and output of different software and build a logical sequence. The basic model building philosophy is to use graphical elements that represent resources, processes and connectors (as seen in Fig. A.5). These elements are then associated to input files, software execution commands, computational routines, etc.

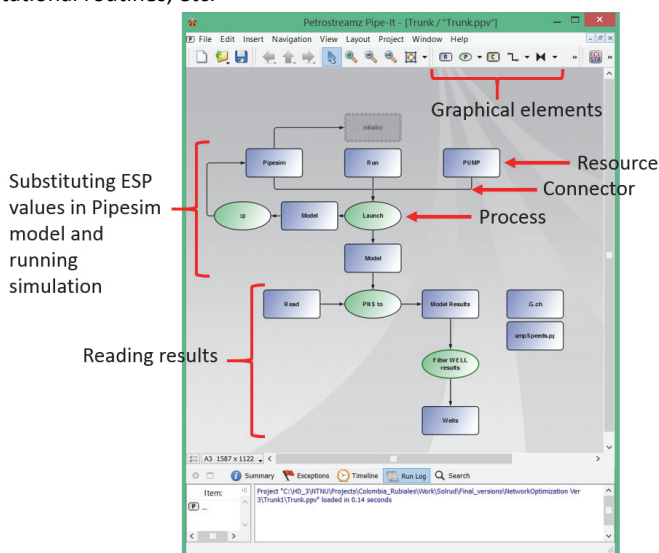


Fig. A.5. Pipe-It's interface

Pipe-It also has a propriety file format (streamz) suited specially for storing characteristics of a fluid stream (e.g pressure). It also has a lot of built-in additional tools available such as the optimizer, Linkz (to spot important variables in text files), translators to the streamz format for common input and output files used by commercial simulators. A snapshot of the optimizer's interface is presented in Fig. A.6.

Name	Role	Cc	Type	Lower	Value	Upper	Equation	RW	Link	Location
1 Sink_Press	CON		real		55			R	Sink...	Trunk.str
2 Sink_Temp	CON		real		51.76			R	Sink...	Trunk.str
3 Sink_GLR	CON		real		0			R	Sink...	Trunk.str
4 Sink_WC	CON		real		89.44			R	Sink...	Trunk.str
5 Sink_Mass...	CON		real		134.5			R	Sink...	Trunk.str
6 Sink_LiqRate	CON		real		3.352e+04			R	Sink...	Trunk.str
7 Sink_GasR...	CON		real		0			R	Sink...	Trunk.str
8 Sink_OilRate	OBJ		real	--	3540	--	((100-SL...			
9 Sink_Water...	CON		real	0	2.999e+04	3e+04	((Sink...			
10 Profit	CON		real		2.448e+05			R	Econ...	Econom...
11 TotalPump	CON		real		538.9			R	Total...	PL1.Tota...
12 Well_1_Pu...	VAR	real	30	45.83	60			W	Pump...	[1] @ InIPum...
13 Well_2_Pu...	VAR	real	30	36.7	60			W	Pump...	[2] @ InIPum...
14 Well_3_Pu...	VAR	real	30	59.75	60			W	Pump...	[3] @ InIPum...
15 Well_4_Pu...	VAR	real	30	36.49	60			W	Pump...	[4] @ InIPum...
16 Well_5_Pu...	VAR	real	30	58.66	60			W	Pump...	[5] @ InIPum...
17 Well_6_Pu...	VAR	real	30	46.02	60			W	Pump...	[6] @ InIPum...
18 Well_1_On...	VAR	int	0	0	1			W	OnOff...	[1] @ InIPum...
19 Well_2_On...	VAR	int	0	0	1			W	OnOff...	[2] @ InIPum...
20 Well_3_On...	VAR	int	0	0	1			W	OnOff...	[3] @ InIPum...
21 Well_4_On...	VAR	int	0	0	1			W	OnOff...	[4] @ InIPum...
22 Well_5_On...	VAR	int	0	0	1			W	OnOff...	[5] @ InIPum...

Fig. A.6. Pipe-It's optimizer interface

• Ansys Icem

Ansys ICEM is a specialized meshing software from the company Ansys. The term “meshing” refers in this context to the action of subdividing a geometry in smaller elements that keep some degree of connectivity between them (share common vertexes, edges and faces). The resulting mesh usually represents accurately the original geometry volumes and surfaces. The main functionality of the software is listed next:

- It allows to import a large variety of geometry file formats (generated either by other Ansys programs or other commercial drawing applications)
- It provides a set of tools to build a mesh. These tools allow to produce different mesh types (types of elements, arrangements of the elements, etc.) and usually cover the cases ranging from semi-manual work to semi-automatic work.
- It also contains a set of tools to verify and check the quality of the mesh.
- It allows to name and tag surfaces and parts of the mesh.
- Additionally it allows to export the mesh in a variety of file formats employed by other Ansys programs or other commercial software.

A snapshot of the graphical interface is shown in Fig. A.7.

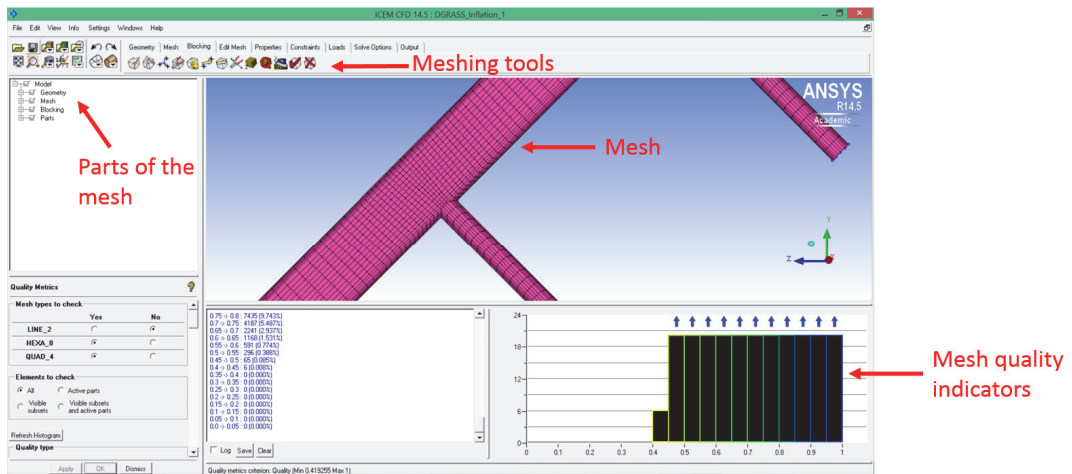


Fig. A.7. Ansys ICEM interface

• Ansys CFX

Ansys CFX is a general purpose fluid dynamics program with an extensive choice of physical models to represent different fluid phenomena. The solver of the software employs the finite volume method.

The program is split into three independent modules:

-CFX Pre: In this module the mesh is imported, the governing physical models are selected and their details are specified, the boundaries are specified and the boundary conditions details are inputted. It is important to note that all the mesh surfaces that are somehow relevant for the modeling have to be tagged in the mesh a priori (by the meshing application). This is because a name will be required when assigning the boundary conditions.

The solver settings, convergence tolerances, number of iterations, output frequency (in case of a transient simulation), variables of interest to monitor and similar are also specified in the CFX Pre.

A snapshot of the graphical interface is shown in Fig. A.8. On the left side of the windows there is a tree view with all the elements of the CFX model. The details of each element can be accessed by double clicking on it with the mouse pointer. New boundary conditions, fluid regions of interest, connectivity regions between two meshes, etc. can be added using the item menu at the top.

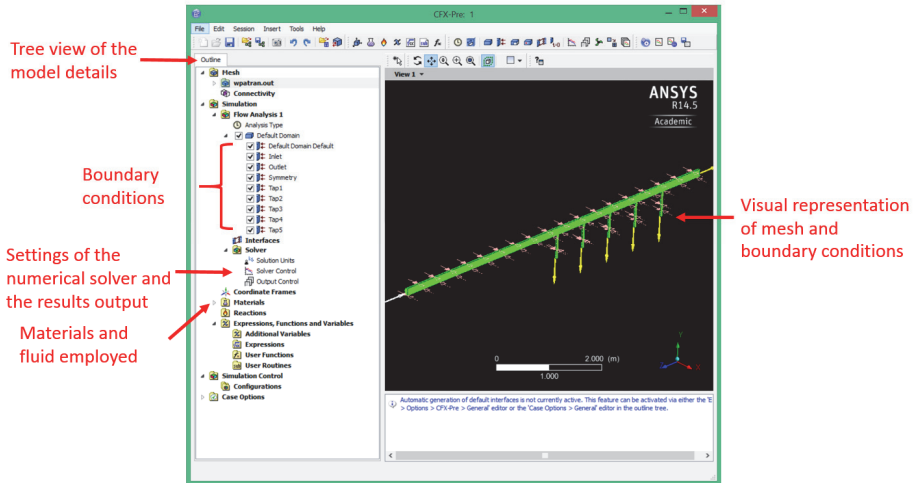


Fig. A.8. Ansys CFX pre interface

-CFX solver manager: In this module some other solver settings are specified regarding parallelization of the computations (if any) and initial conditions. During the solving process there is a residual monitor plot vs the number of iterations and a progress window showing detailed messages from the solver (as shown in Fig. A.9).

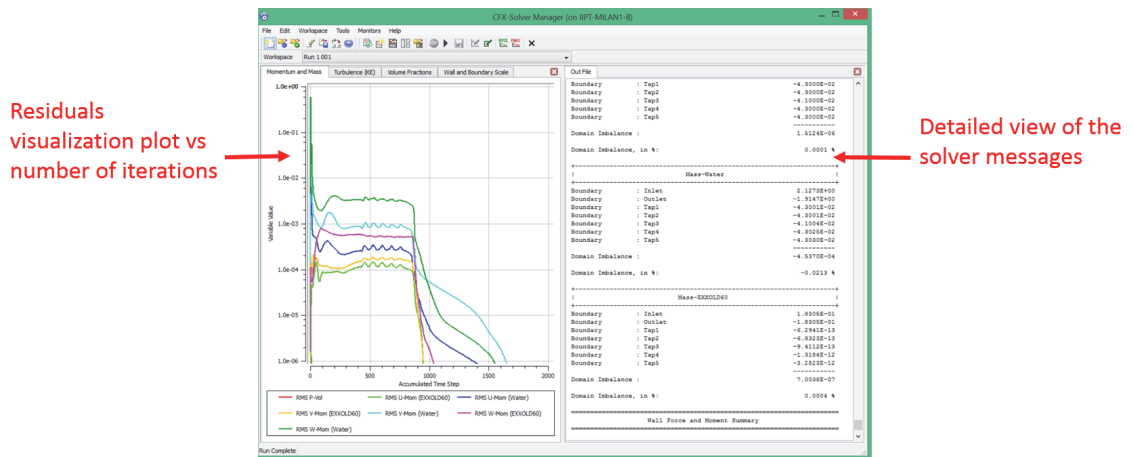


Fig. A.9. Ansys CFX solver manager interface

-CFX Post: This module is meant for the visualization, inspection, analysis and export of the simulation results. A snapshot of the interface is shown in Fig. A.10. The CFX-post allows to display the values of pre-specified variables on mesh surfaces and boundaries using color scales. It allows also to create user defined lines, points, planes, surfaces, streamlines and color them in a similar fashion. The numerical values of the variables on these elements (average, maximum, minimum, evenly distributed, etc.) can also be computed and exported.

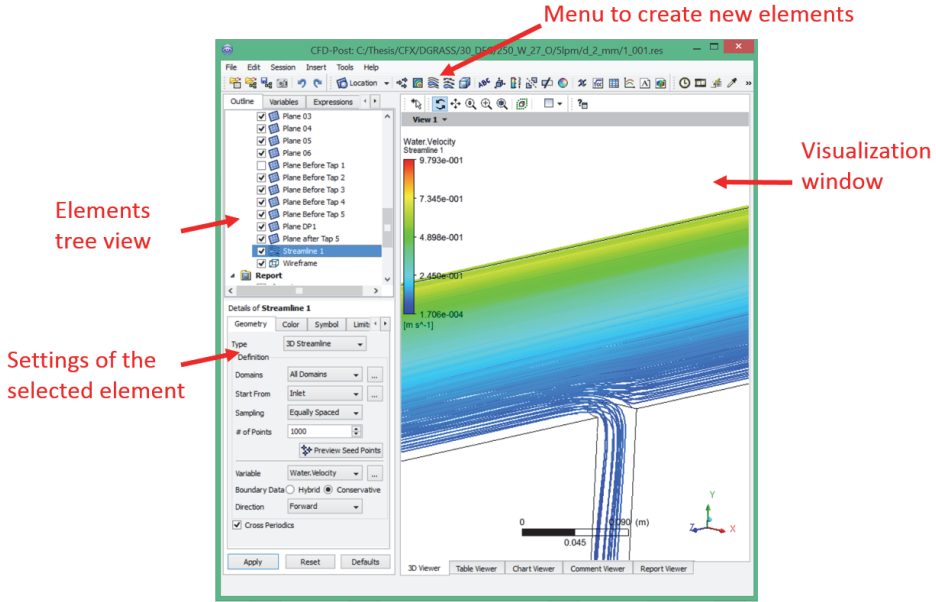


Fig. A.10. Ansys CFX post interface

• **Ansys Workbench**

Ansys Workbench is a computational environment that allows to create simulation projects using the software tools from Ansys. It is possible to trigger all the Ansys applications from the workbench, create the models and store them in the workbench project. It also allows to transfer automatically information from one application to another.

Ansys Workbench also includes some tools (only accessible through the Ansys Workbench interface) for geometry generation and meshing (called CFX meshing). An example of the Ansys Workbench interface for a CFX simulation project is presented in Fig. A.11.

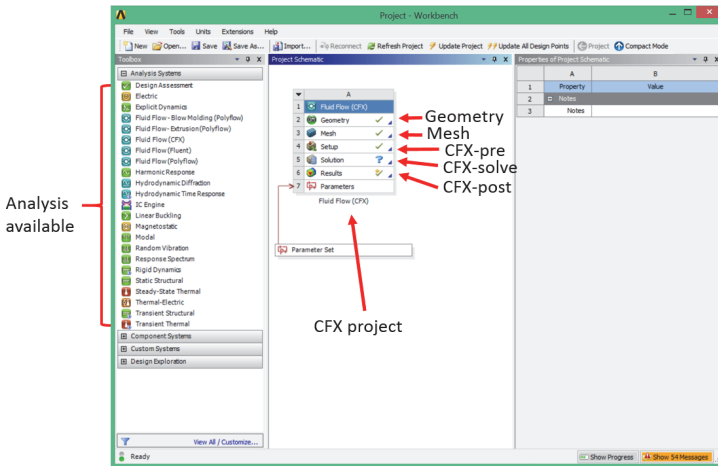


Fig. A.11. Ansys Workbench interface

The CFX meshing interface opened through Ansys Workbench is shown in Fig. A.12.

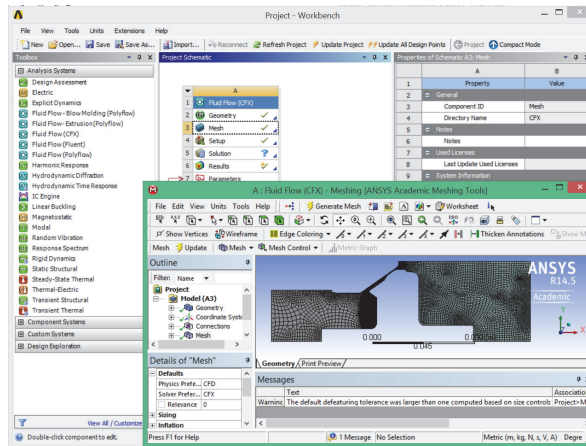


Fig. A.12. Ansys CFX meshing module open from the Workbench interface

• AFT Impulse

AFT Impulse is a software from the company Applied Flow Technology (AFT). This program allows to calculate one dimensional transient hydraulic behavior in piping systems taking into account the changes in fluid density and pipe deformation (due to pressure variations). AFT Impulse has many piping components and pulsation arresting elements available. The program has two solvers: a transient solver based on the Method of Characteristics and a steady state solver to calculate the initial conditions for the transient simulation.

The program has a graphical interface (as shown in Fig. A.13) where the elements can be dragged to the canvas with the mouse pointer for model building. The settings of the individual components are inputted by double clicking the elements and filling the dialog screen. The common and general settings are inputted by using the menu shown in Fig. A.13.

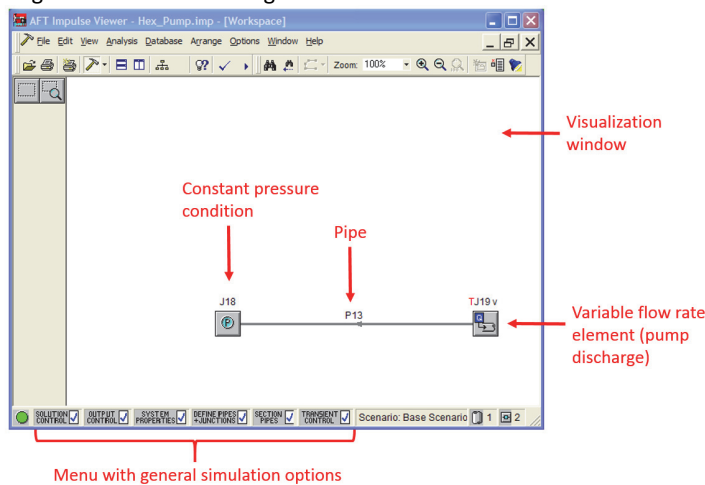


Fig. A.13. AFT Impulse interface